Self-healing $M_{n+1}AX_n$-phase ceramics

Farle, Ann-Sophie

DOI
10.4233/uuid:ef2e1c2c-f88b-4cca-b52d-b06e06822a22

Publication date
2017

Document Version
Final published version

Citation (APA)
Farle, A.-S. (2017). *Self-healing $M_{n+1}AX_n$-phase ceramics*. [Dissertation (TU Delft), Delft University of Technology]. https://doi.org/10.4233/uuid:ef2e1c2c-f88b-4cca-b52d-b06e06822a22

SELF-HEALING $M_{n+1}AX_n$-PHASE CERAMICS

SELF-HEALING $M_{n+1}AX_n$-PHASE CERAMICS

Proefschrift

ter verkrijging van de graad van doctor
aan de Technische Universiteit Delft,
op gezag van de Rector Magnificus prof. ir. K.C.A.M. Luyben,
voorzitter van het College voor Promoties,
in het openbaar te verdedigen op donderdag 11 mei 2017 om 12:30 uur

door

Ann-Sophie Magdalena FARLE

Master of Engineering,
University of Queensland, Brisbane, Australia,
geboren te Berlijn, Duitsland.

Dit proefschrift is goedgekeurd door de

promotor: prof. dr. S. van der Zwaag
copromotor: dr. W.G. Sloof

Samenstelling promotiecommissie:

Rector Magnificus,	voorzitter
Prof. dr. ir. S. van der Zwaag	Technische Universiteit Delft
Dr. ir. W.G. Sloof,	Technische Universiteit Delft
Onafhankelijke leden:	
Prof. dr. P. Greil	Friedich-Alexander Universität Erlangen-Nürnberg
Prof. dr. A.J.A. Winnubst	University of Science and Technology of China & University of Twente
Prof. dr. ir. K. van Breugel	Technische Universiteit Delft
Prof. dr. E.H. Brück	Technische Universiteit Delft
Prof. dr. I. Richardson	Technische Universiteit Delft


Keywords: Self-healing ceramics, MAX-phase ceramics, Oxidation, SPS, FEM

Printed by: Ipskamp Printing, Enschede

Front & Back: SEM micrograph of Ti_2AlC

ISBN 978-94-028-0626-7

An electronic version of this dissertation is available at
`http://repository.tudelft.nl/`.

You'll miss the best things if you keep your eyes shut.
Sometimes the questions are complicated and the answers are simple.

Dr Seuss

Contents

Summary

Damage management and the development of new materials come together in self-healing $M_{n+1}AX_n$ phase ceramics. These ternary layered carbides and nitrides exhibit a multitude of properties, such as high temperature strength, fracture toughness, thermal and electrical conductivity and machinability, which have been discovered over the past 20 years. In addition, intrinsic crack-gap filling and strength recovery by high temperature oxidation have been demonstrated for Ti_2AlC, Cr_2AlC and Ti_3AlC_2. The selective oxidation of the A-element, Aluminium in all known cases, leads to almost full crack gap closure by Al_2O_3 filling. The dense, strong and well adhering oxide is formed at temperatures above 1000 °C in atmospheric air and can restore the integrity of a sample even for multiple successive crack-healing cycles.

The potential applications for such functional materials are vast, but currently restricted to high temperature fields. In general, use of ceramics has been limited due to their brittle nature and limited toughness. Furthermore, the viability of the new high temperature self-healing mechanisms in application relevant conditions, i.e. combustion engines, is unknown. By predicting, analysing and applying self-healing MAX phases an important gap to industrial use can be bridged and development accelerated.

Of the more than 75 known MAX phase compounds, more than just Ti_2AlC, Ti_3AlC_2 and Cr_2AlC could exhibit self-healing abilities. New healing products and varying initial matrix properties could expand the range of possible applications for self-healing metallo-ceramics. Further self-healing MAX-phases are identified by postulating design criteria to predict compounds with optimal healing properties: i.e. the formation of a stable oxide upon selective oxidation, mobility of reactive constituents, oxide adhesion, and sufficient volume expansion to fill crack gaps. Also the healing agent is scrutinized concerning its match of Young's Modulus and coefficient of thermal expansion (CTE) to the virgin matrix material. The application of these design criteria to the known MAX-phases is presented in Chapter 2. Known compounds, Ti_2AlC, Ti_3AlC_2 and Cr_2AlC, conform with the postulated demands, as well as Ti_3SiC_2 and Ta_2AlC, for which self-healing behaviour is yet to be demonstrated.

To investigate self-healing in ceramic composites, traditional bending tests with a high material consumption and little crack-path control have been replaced by a newly designed test method to induce controlled cracks and determine material properties. By wedge loading a new chevron notched specimen geometry, with side grooves and a rounded bottom, a crack is propagated through the material. The controlled manner of creating cracks, i.e. without fully fracturing the specimen, is beneficial for healing treatments and self-healing characterization. Furthermore, the recorded load-displacement data and final crack length can be processed by means of finite element analysis based on cohesive zone modelling to determine the fracture energy and fracture strength of the material, see Chapter 3.

Comparison of healed and virgin properties in a single specimen has not been possible using conventional methods. However, samples with cracks created by loading of the new chevron notched, wedge loaded specimen (WLS) can be thermally treated ex-situ before re-cracking under identical conditions. The properties of the healed sample are thus directly comparable to those of the virgin sample. Ti_2AlC, a known self-healing MAX-phase, showed a crack gap filling by oxidation, carried out at 1200 °C for 2 h. Fracture strength recovery could be quantified by applying and further developing the procedure described in Chapter 3. Chapter 4 shows the details of the Al_2O_3 crack gap filling and analysis of the load-displacement data by a simulation-based approach using finite element analysis based on cohesive zone modelling. The analysis showed that in the detailed case considered 70% of the fracture strength was recovered. Furthermore, the fracture energy of the healed zone was 60% of that of the virgin Ti_2AlC.

Ta_2AlC and Ti_3SiC_2, predicted to be self-healing on basis of the prior determined design criteria (cf. Chapter 2), were synthesised, analysed regarding their oxidation behaviour and tested using the previously described new method. Samples of up to 50 mm diameter were synthesised by spark plasma sintering at 1400 and 1500 °C of Ti, Ta, Al and graphite or TiC powder mixtures. High purity, homogeneous and dense samples were produced in a single sintering process within up to three hours. By investigating the oxide formation at selected temperatures via thermogravimetric and differential thermal analysis (TGA/DTA), as well as preliminary crack-healing tests (e.g. thermal shock) crap-gap filling conditions, i.e. temperature and time, were determined.

Ta_2AlC and Ti_3SiC_2, just like the known Ti_2AlC, Cr_2AlC and Ti_3AlC_2, were expected to show preferential A-element oxidation, resulting in Al_2O_3 or SiO_2 formation. However, both Ti_3SiC_2 and Ta_2AlC formed M- and A-element oxides as the self-healing agents. Ti_3SiC_2 filled cracks with a mixture of Si and Ti oxides and exhibited strength recovery even when only partial crack gap filling was achieved, as shown in Chapter 5. Cracks of up 10 µm in Ti_3SiC_2 were filled by TiO_2, sandwiched between amorphous SiO_2 layers. Healing for 1 h at 1200 °C was insufficient to achieve full crack gap filling.

The predicted crack gap filling and strength recovery of Ta_2AlC could not be achieved because of the formation of porous Ta-based oxides, instead of the anticipated A-element oxide Al_2O_3. The similarities between Ta_2AlC and Ta_2C oxidation, from activation energy to oxide morphology show that limited A-element mobility strongly influences the healing behaviour. Chapter 6 discusses the healing performance and oxidation of the Ta_2AlC. It is concluded that predictive tools using only thermodynamic data are insufficient for determining MAX-phase oxidation processes. Kinetic factors are of major influence and must be taken into account, such as the oxygen diffusivity through both M- and A-oxides.

Finally, in Chapter 7, to demonstrate the potential of functional self-healing materials in realistic settings, three known systems, two MAX phases (Ti_2AlC and Cr_2AlC) and a ceramic composite (Al_2O_3/TiC) were tested in a combustion chamber. The exposure of pre-cracked samples to low oxygen partial pressures and temperatures up to 1100 °C in the exhaust of a combustion setup shows that all tested self-healing ceramics can fill micro-cracks under turbulent realistic conditions. The healing behaviour observed under combustion conditions did not differ from that recorded using a static lab furnace filled with synthetic air.

Samenvatting

De ontwikkeling van nieuwe materialen en schademanagement komen samen in zelfherstellende MAX-fasen. Deze ternaire carbides en nitrides met een gelaagde structuur, ontdekt in de afgelopen 20 jaar, bezitten bijzondere eigenschappen, zoals: een goede sterkte bij hoge temperaturen, een behoorlijke breuktaaiheid, zowel elektrische als thermische geleidbaarheid en zijn gemakkelijk te bewerken. Recent is voor drie bekende MAX-fasen, namelijk Cr_2AlC, Ti_2AlC en Ti_3AlC_2, aangetoond dat microscheuren als gevolg van oxidatie bij hoge temperatuur als vanzelf dichttrekken en de mechanische sterkte hersteld wordt. De selectieve oxidatie van het A-element, in dit geval aluminium, resulteert in een bijna volledige vulling van de scheuren met Al_2O_3. Dit dichte, sterke en goed hechtende oxide wordt gevormd bij temperaturen boven 1000 °C in lucht en kan de integriteit van een preparaat herstellen, zelfs na meerdere achtereenvolgende scheur- en herstel-cycli.

Er zijn velerlei toepassingen voor dergelijke functionele materialen, maar deze zijn echter (nog) beperkt tot het domein van hoge-temperatuur toepassingen. Door de brosheid van keramische materialen is het gebruik ervan gering. Bovendien is het momenteel niet bekend of het nieuwe zelf-herstellend hoge-temperatuur mechanisme in toepassingen, zoals bijvoorbeeld verbrandingsmotoren, werkt. De kloof naar industriële toepassing kan echter worden overbrugd en de ontwikkeling van deze materialen kan worden versneld door het gedrag van zelfherstellende MAX-fasen te voorspellen, te analyseren en toe te passen.

Naast de eerder genoemde Ti_2AlC, Ti_3AlC_2 en Cr_2AlC kunnen ook andere varianten van de meer dan 75 bekende MAX-fasen zelfherstellende eigenschappen hebben. Andere herstellende producten en andere initiële matrix-eigenschappen kunnen de mogelijke toepassingen van zelfherstellende MAX-fasen uitbreiden. Andere zelfherstellende MAX-fasen kunnen worden geïdentificeerd door het postuleren van criteria die aangeven of deze ternaire carbiden en nitriden mogelijk zelf-herstellend gedrag gaan vertonen: de vorming van stabiele oxides tijdens oxidatie bij hoge temperaturen, de mobiliteit van de reactieve componenten, de hechting van oxide en voldoende volume expansie om scheuren te vullen. Bovendien is gekeken of de elasticiteitsmodulus en de thermische uitzettingscoefficiënt van het gevormde oxide en de oorspronkelijke matrix voldoende overeenkomen. De toepassing van deze criteria is opgenomen in hoofdstuk 2. De bekende verbindingen, Ti_2AlC, Ti_3AlC_2 en Cr_2AlC voldoen aan de gestelde eisen maar dat doen ook Ti_3SiC_2 en Ta_2AlC waarvan het zelfherstellende gedrag nog moet worden aangetoond.

Om het zelf-herstellen van keramische materialen te onderzoeken, zijn traditionele buigtesten met een groot materiaalverbruik en beperkte controle over scheurvorming vervangen door een nieuw ontwikkelde methode waarmee op gecontroleerde wijze een scheur geïnitieerd kan worden en de eigenschappen van het materiaal kunnen worden bepaald. Een scheur wordt gecreëerd door een wig te drijven in een preparaat van het

materiaal met een nieuwe geometrie met chevron inkeping, zijgroeven en een ronde bodem. De gecontroleerde wijze waarop een scheur wordt gemaakt zonder het preparaat te breken, is aantrekkelijk voor het bestuderen van het zelfherstellende vermogen. Bovendien kunnen breukenergie en sterkte van het materiaal worden bepaald uit de opgenomen kracht versus verplaatsingscurve en de scheurlengte door middel van een eindige elementenanalyse op basis van 'cohesive-zone' modeleren. Deze nieuwe methode van gecontroleerde scheur initiatie is beschreven in hoofdstuk 3.

Tot nu toe was het niet mogelijk om de eigenschappen van het materiaal voor en na zelfherstel in één en hetzelfde preparaat te bepalen en met elkaar te vergelijken. Echter met de nieuwe preparaatgeometrie met chevron inkeping en wig belasting (hierna WLS genoemd) kan het gescheurde preparaat ex-situ behandeld worden voordat er een nieuwe scheur gevormd wordt onder identieke omstandigheden. Aldus is een directe vergelijking mogelijk tussen de eigenschappen van het maagdelijk materiaal en de eigenschappen van het materiaal na het repareren van een scheur. Ti_2AlC, een bekend zelfherstellende MAX-fase, laat scheurvulling zien door oxidatie bij 1200 °C gedurende 2 uur. De breuksterkte na het herstellen van de scheur kan worden gekwantificeerd door verdere ontwikkeling van de procedure beschreven in hoofdstuk 3. Details van het vullen van de scheur met Al_2O_3 en het analyseren van de kracht versus verplaatsingscurve met behulp van eindige elementenanalyse op basis van 'cohesive-zone' modeleren, zijn beschreven in hoofdstuk 4.

Ti_3SiC_2 en Ta_2AlC, waarvan op basis van de ontwerp criteria voorspeld is dat deze MAX fasen zelf-herstellend zijn (zie hoofdstuk 2), zijn bereid en vervolgens geanalyseerd op hun oxidatie gedrag en onderzocht met de hiervoor genoemde nieuwe beproevingsmethode. Preparaten met diameter tot 50 mm zijn met spark plasma sinteren vervaardigd bij 1400 en 1500 °C met Ti, Ta, Al, en grafiet of TiC poedermengsels. Materialen met een hoge relatieve dichtheid, een homogene samenstelling en een hoge zuiverheid konden in een enkelvoudig proces binnen drie uur vervaardigd worden. De condities voor het herstellen van scheuren, d.w.z. temperatuur en tijd, zijn onderzocht door het oxidatie-gedrag te bestuderen met thermogravimetrische en calorimetrische technieken alsmede door inleidend testen waarbij scheuren, die via thermische schok zijn geïnitieerd, worden gerepareerd.

Net als bij Ti_2AlC, Cr_2AlC en Ti_3AlC_2, werd preferentiële oxidatie van het A-element verwacht bij Ta_2AlC en Ti_3SiC_2 zodat respectievelijk Al_2O_3 of SiO_2 gevormd wordt. Echter zowel Ta_2AlC als Ti_3SiC_2 vormden oxiden van zowel het M- als het A element. Scheuren in Ti_3SiC_2 worden gevuld met een mengsel van TiO_2 en SiO_2 waardoor de sterkte zich herstelt ondanks dat de scheuren gedeeltelijk waren gevuld; zie hoofdstuk 5. Scheuren tot 10 µm breed in Ti_3SiC_2 waren gevuld met TiO_2 omgeven door amorfe SiO_2. Oxidatie bij 1200 °C gedurende 1 uur bleek echter onvoldoende voor het volledig vullen van de scheuren.

De verwachte vulling van scheuren in Ta_2AlC en herstel van sterkte is niet opgetreden, omdat er poreuze tantaaloxiden werden gevormd in plaats van Al_2O_3. De beperkte mobiliteit van het A-element heeft grote invloed op het zelf-herstellend gedrag blijkt uit overeenkomsten tussen het oxidatie gedrag van Ta_2AlC en Ta_2C in termen van de activeringsenergie en van de morfologie van de gevormde oxide. In hoofdstuk 6, worden het herstellend vermogen en de oxidatie van Ta_2AlC besproken. Geconcludeerd wordt

dat criteria uitsluitend gebaseerd op thermodynamische data (zie hoofdstuk 2) onvoldoende zijn voor het voorspellen van de oxidatie processen in MAX-fasen. Kinetische factoren, zoals de diffusie van zuurstof door M- en A-oxiden, hebben een grote invloed en moeten ook in beschouwing worden genomen.

Ten slotte wordt in hoofdstuk 7 het potentieel van functionele zelfherstellende materialen onder realistische omstandigheden aangetoond door twee bekende MAX-fasen (Ti_2AlC en Cr_2AlC) en een keramische composiet (Al_2O_3 / TiC) in een simulator voor de verbrandingskamer van een turbine motor te testen. In al deze materialen kunnen microscheuren onder turbulente en realistische omstandigheden gevuld worden bij 1000 °C en een lage partiële zuurstofdruk. Er is geen verschil waargenomen in het zelf-herstellend gedrag onder condities in een verbrandingskamer van een turbinemotor en die in een stationaire laboratoriumoven gevuld met synthetische lucht.

Zusammenfassung

Die Entwicklung neuer Materialien und das Prinzip Schadensmanagement kommen in selbst-heilenden MAX-phasen zusammen. Diese ternären, atomar geschichteten Carbide und Nitride besitzen außerordentliche Eigenschaften, etwa gute mechanische Festigkeit bei hohen Temperaturen, Bruchzähigkeit, gute elektrische- und thermische Transporteigenschaften, sowie gute maschinelle Bearbeitungsmöglichkeiten. Außerdem wurde kürzlich die Fähigkeit zur Selbstheilung von mechanischen Rissen durch intrinsische Rissfüllung und Festigkeits-Regeneration durch Hochtemperatur-Oxidation für drei der bekannten MAX-phasen Zusammensetzungen, nämlich Cr_2AlC, Ti_2AlC und Ti_3AlC_2, demonstriert. Die selektive Oxidation des A-Elements, Aluminium, führt zu fast vollständiger Rissfüllung durch Al_2O_3. Das dichte, stabile und gut haftende Oxid wird bei Temperaturen über 1000 °C in atmosphärischer Luft geformt und kann die Integrität einer Probe über mehrere Bruch-Heilungs-Zyklen hinweg wiederherstellen.

Es gibt weitreichende potenzielle Einsatzgebiete für derart funktionale Materialien, die jedoch (noch) auf Hochtemperatur Anwendungen begrenzt sind. Aufgrund der Brüchigkeit und geringen Zähigkeit ist der Einsatz von Keramiken beschränkt. Zudem ist die Funktionsfähigkeit der neuen selbst-heilenden Hochtemperatur-Mechanismen im Anwendungsbetrieb, z.B. in Verbrennungsmotoren, derzeit unbekannt. Durch Vorhersage, Analyse und Anwendung von selbst-heilenden MAX-phasen können wichtige Schritte zum industriellen Einsatz gemacht und die Entwicklung beschleunigt werden.

Von den über 75 bekannten MAX-phasen könnten mehr als nur die bereits genannten Ti_2AlC, Ti_3AlC_2 und Cr_2AlC selbst-heilende Eigenschaften besitzen. Andere Produkte des oxidativen Heilungsprozesses und unterschiedliche Matrix-Eigenschaften könnten die Bandbreite an möglichen Anwendungsgebieten für selbst-heilende Metall-Keramiken vergrößern. Durch die Definition von Kriterien werden weitere MAX-phasen mit optimalen selbst-heilenden Eigenschaften identifiziert, etwa die Bildung stabiler Oxide während einer Oxidation bei hohen Temperaturen, die Mobilität der reaktiven Bestandteile, die Oxidhaftung und eine hinreichende Ausdehnung, um Risse zu füllen. Des Weiteren ist die Kompatibilität der Elastizitätsmodule und der Wärmeausdehnungskoeffizienten im Vergleich zur ursprünglichen Matrix zu prüfen. Die Anwendung dieser Kriterien wird nach einer allgemeinen Einführung (Kapitel 1) in Kapitel 2 präsentiert. Es zeigt sich, dass die bekannten Verbindungen, Ti_2AlC, Ti_3AlC_2 und Cr_2AlC, genauso wie die bisher nicht-untersuchten Ti_3SiC_2 und Ta_2AlC die gestellten Anforderungen erfüllen.

Des Weiteren werden traditionelle Biegeversuche mit hohem Materialverbrauch und geringer Risspfadkontrolle durch eine neue Methode der kontrollierten Risseinleitung ersetzt, um die Selbstheilung in keramischen Verbundwerkstoffen zu prüfen. Durch Keilladung einer neuen Probengeometrie mit Chevron Einkerbung, Seitenrillen und einer gerundeten Unterkante wird ein Riss durch das Material propagiert. Diese kontrollierte Art Risse zu induzieren, d.h. ohne vollständigen Probenbruch, ist vorteilhaft für eine nachfolgende Heilbehandlung und Riss-Charakterisierung. Außerdem können die auf-

gezeichneten Daten der Belastungskurve und Risslänge via Finite-Elemente-Analyse auf Basis des Kohäsions-Bereich-Models entsprechend analysiert werden, um Bruchenergie und Bruchfestigkeit des Materials festzustellen. Diese neue Methode der kontrollierten Risseinleitung ist Inhalt von Kapitel 3 der vorliegenden Arbeit.

Bisher war es nicht möglich, die ursprünglichen und geheilten Eigenschaften in derselben Probe zu erfassen und zu vergleichen. Die neue Probengeometrie mit Chevron Einkerbung und Keilladung (im Folgenden bezeichnet als WLS) erlaubt eine ex-situ Wärmebehandlung vor einer erneuten Risseinleitung unter identischen Bedingungen. Damit ist der direkte Vergleich der Eigenschaften der geheilten WLS-Probe mit der WLS-Originalprobe möglich. Ti_2AlC, eine bekannte selbst-heilende MAX-phase, zeigte eine Rissfüllung nach Oxidation bei 1200 °C für 2 Stunden. Die erlangte Wiederherstellung der Bruchfestigkeit kann mittels Weiterentwicklung der Methode aus Kapitel 3 quantifiziert werden. Im anschließenden Kapitel 4 werden die Details der Al_2O_3 Rissfüllung und der Analyse der Belastungskurve mittels Finite-Elemente-Analyse auf Basis des Kohäsions-Bereich-Models thematisiert.

Aufgrund der Vorhersagen aus Kapitel 2 werden Ti_3SiC_2 und Ta2AlC hergestellt, bezüglich ihres Oxidationsverhaltens analysiert und mittels der bereits beschriebenen neuen Methodik aus Kapitel 3 untersucht. Proben von bis zu 50 mm Durchmesser werden durch Spark Plasma Sintern bei 1400 und 1500 °C aus Ti, Ta, Al und Graphit oder TiC Pulvermischungen synthetisiert. Binnen 3 Stunden können dichte, homogene und reine Proben hergestellt werden. Oxidationsstudien mittels thermogravimetrischer- und Differentialthermoanalyse, sowie vorläufige Heilungsversuche (z.B. Thermoshock) führen zur Bestimmung der Rissfüllungsbedingungen, Zeit und Temperatur.

Wie bei ihren Vorgängern, Ti_2AlC, Cr_2AlC und Ti_3AlC_2, wird auch bei Ta_2AlC und Ti_3SiC_2 eine Präferenz der Oxidation der A-elemente erwartet. Jedoch formen beide MAX-phasen M- und A-Element Oxide zur Rissfüllung. Eine partielle Wiederherstellung der Eigenschaften von Ti_3SiC_2 wird trotz einer nur teilweise erfolgten Rissfüllung erreicht, siehe Kapitel 5. Risse von bis zu 5 µm in Ti_3SiC_2 werden durch TiO_2, umgeben von amorphem SiO_2 Schichten, gefüllt. Die Oxidation bei 1200 °C für 1 Stunde ist unzureichend für eine vollständige Rissfüllung.

Die antizipierte Rissheilung und Eigenschaftswiederherstellung von Ta_2AlC durch selektive oxidation von Al wird nicht erreicht, stattdessen ist poröse Ta-Oxid Bildung dominierend. Die Parallelen zur Ta_2C Oxidation, von der Aktivierungsenergie hinzu der Oxidmorphologie zeigen, dass die beschränkte Mobilität des A-Elements großen Einfluss auf das Heilvermögen der MAX-phasen hat. In Kapitel 6 werden Oxidation und Heilungsvermögen von Ta_2AlC besprochen. Es wird geschlussfolgert, dass die Prognosekriterien aus Kapitel 2, basierend ausschließlich auf thermodynamischen Daten, nicht hinreichend zur Vorhersage von Oxidationsprozessen in MAX-phasen sind. Kinetische Faktoren, wie das Diffusionsvermögen von Sauerstoff durch M- und A-Oxide, haben großen Einfluss und müssen in Zukunft berücksichtigt werden.

Abschließend wird in Kapitel 7 das Potential funktionaler selbst-heilender Materialien unter realistischen Bedingungen an zwei bekannten MAX-phasen (Ti_2AlC und Cr_2AlC) und einem keramischen Verbundwerkstoff (Al_2O_3/TiC) demonstriert. Alle untersuchten Proben konnten unter turbulenten realistischen Bedingungen, im Auslass eines Verbrennungsmotorenaufbaus bei bis zu 1000 °C und geringem Sauerstoffpartialdruck Micro-

Risse füllen. Es konnte keine Abweichung vom Heilverhalten unter Anwendungsbedingungen im Verbrennungsmotor und vom bekannten Verhalten unter Laborbedingungen festgestellt werden.

1

Introduction

If you aren't in over your head, how do you know how tall you are?

T.S. Eliot

1

1.1. Introduction

Material development drives innovation. Better materials mean more data storage, faster engines, stronger structures. Development of composite materials, for example has redefined aircraft design to larger and lighter carriers [1]. Structures can be built taller, with longer life time thanks to better structural materials [2]. A steady development of new materials and the improvement of existing ones is a driving force of modern civilization.

Crack formation is a common issue in all structural materials, which can lead to failure of whole components. In the worst case, replacement, in others, time-consuming maintenance is required to prevent failure of structural components. Formation of damage can never be prevented and this notion has led to the development of stronger and tougher materials under the paradigm of 'damage prevention' [3]. By changing the materials design approach from 'damage prevention' to 'damage management' a new class of materials is being developed to control and reverse crack damage and thus prevent component failure. The leading principle is, that formation of damage is not problematic as long as an autonomous counteraction can minimize or remove said damage [3]. The field of self-healing materials is the application of the 'damage management' concept. Materials are equipped with mechanisms to 'heal' damage. Introduced in Scott White et al.'s work [4] in an epoxy used for aerospace applications, the field of self-healing now encompasses all material classes, from composite materials to brittle ceramics.

To realize self-healing in existing materials 'local temporary mobility' needs to be introduced into existing conventional non-self healing materials. This means that transport of material or reactants to the damage site must be possible. Movement should be restricted after the material has been restored, i.e. the damage repaired. Furthermore, the activation of said movement should occur autonomously or by minor human stimulation. To achieve this 'local temporary mobility' in existing materials, new material design concepts are required [5, 6].

Two rather different healing concepts are used in self-healing materials: extrinsic and intrinsic healing. The former is based on the incorporation of sacrificial particles in the matrix that release a healing agent to fill cracks, as demonstrated by White et al. [4]. In these cases, filled capsules or particles are added to the original material matrix to act as healing agents upon damage. Rupture of the capsules or exposure to the environment due to crack formation releases the healing agent. The actual release can take rather different forms, like bacteria in concrete [7] or oxidizing particles in ceramics [8], see Figure 1.1. A drawback of this method is that by addition of particles to a matrix the properties of the initial material e.g. the fracture toughness or conductivity [3] in general will be reduced. Furthermore, once hit by a crack foreign healing agents can only heal single damage events. If cracks occur in a previously healed zone, most healing agents will have utilized their capacity and are no longer available for renewed crack repair.

If no foreign healing agent needs to be incorporated into the virginal material to make it capable of healing crack damage, we speak of intrinsic healing. Intrinsic self-healing is not feasible for all materials as it is an inherent property, relying for example on reversible bonding reactions, formation of new polymeric chain entanglements or formation of secondary chemical bonds [6]. Most of these events are triggered by external incentives, such as heat or mechanical stimulation [6]. Examples of intrinsic self-

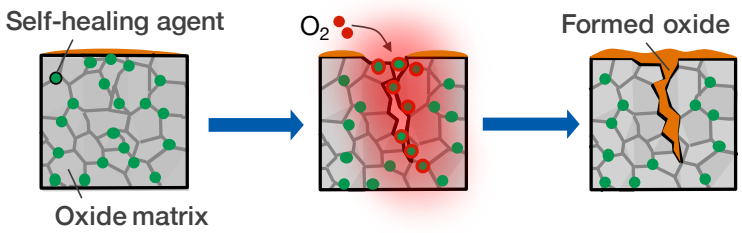

Figure 1.1: Schematic of the self-healing in the ceramics containing self-healing agent at high temperature in the presence of air [8].

healing are the replacement of aromatic diamine by branched aliphatic dimer diamine in polyetherimides [9] or thermally controlled hydrogen bond cross-linking in Nucrel [10].

In ceramics 'local temporary mobility' is limited due to the strong ionic bonding and high activation energies required for solid state diffusion. Treatments above application temperature (>1000°C) can repair surface cracks of less than 5 µm width [11]. By incorporating sacrificial healing particles which oxidize at high temperatures (>1000 °C), such as SiC, crack gap filling has been achieved in an Al_2O_3 matrix [12]. Hereby the effect of particle size on the sintering process as well as the temperature area is of importance. Beyond extrinsic healing classic oxide ceramics have no ability to autonomously repair damage, aside from minor surface crack closure observed in ZnO or Mullite at temperatures close to their respective melting temperatures [11, 13]. $M_{n+1}AX_n$ (MAX-) phase metallo-ceramics have shown the ability to autonomously, intrinsically self-heal crack damage by oxidation at high temperatures [14]. Three MAX-phases, Ti_2AlC, Ti_3AlC_2 and Cr_2AlC can heal crack gaps by forming reaction products upon oxidation at elevated temperatures [15–17].

1.2. MAX-Phase Ceramics

In 1963 Jeitschko et al. [18] discovered a new phase with a composition of M (transition metal) – Me (meta metal) – X (Carbon), naming them H-Phase. This was the beginning of what we today call the MAX-Phases. Over the next 10 years, Jeitschko, Nowotny and Benesovsky published a number of papers discussing the new discoveries and expanding the class of precursors to include Nitride [19, 20]. Barsoum & El-Raghy [21] achieved the first documented synthesis of bulk Ti_3SiC_2 in 1996, over 30 years after the first report by Jeitschko about the H-Phase materials.

The $M_{n+1}AX_n$ phase ceramics are grouped into categories based on their stoichiometry, such as the 211, 312 and 413 Phases, see Figure 1.2. These share a hexagonal structure with M6X octahedral separating A-layers. These octahedral are the same as found in binary carbides and nitrides and share an edge. In the 211 phase, two MX-layers lie between A-element layers, while for the 312 and 413 phases, the number of layers increases to three and four, respectively (Figure 1.2).

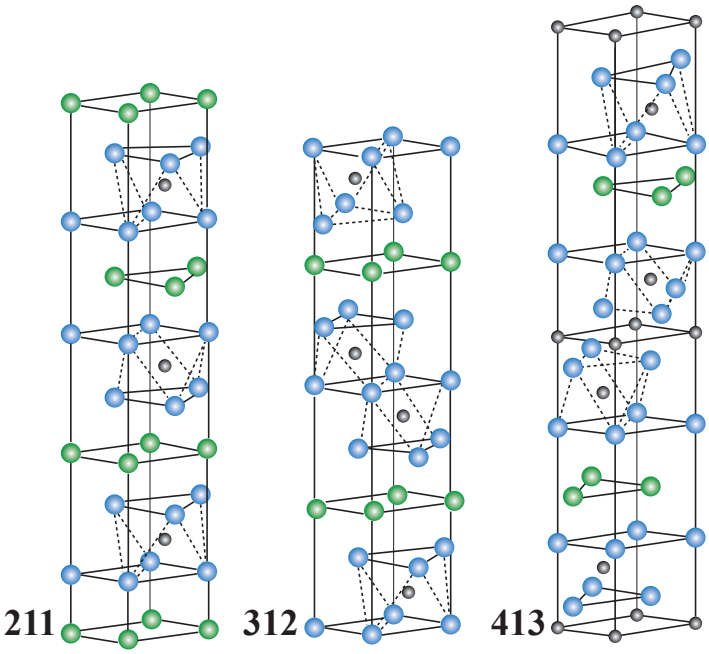

Figure 1.2: Crystal Structure of 211, 312 and 413 MAX Phases; adapted from [20].

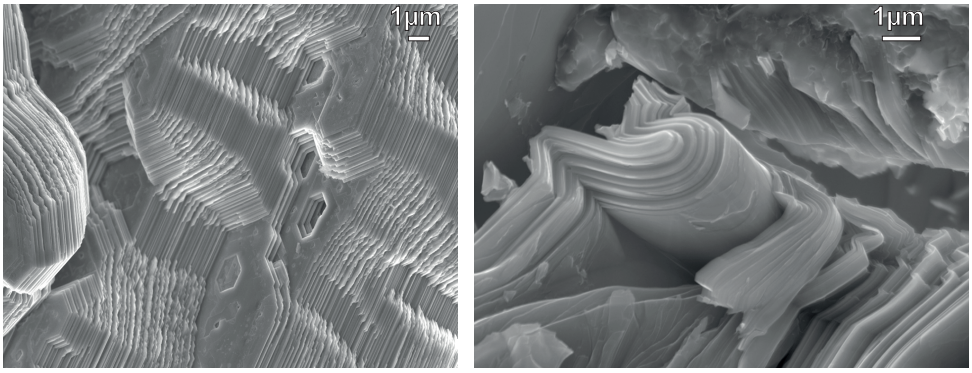

Figure 1.3: SEM images of laminar structure and kinking.

The atomistic arrangement within the MAX phase compounds leads to a laminar micro-structure (see Figure 1.3) and is responsible for multiple properties not commonly associated with ceramics, such as high damage tolerance including thermal shock, excellent machinability and electrical and thermal conductivity.

With the development of methods to synthesise MAX phases in bulk and the investigation into their oxidation behavior, autonomous crack-healing was added to the list of properties exhibited by some MAX-phase compounds. For example, cracks of 7 mm in length and a width of 5 µm in Ti_3AlC_2 were fully filled by Al_2O_3 and TiO_2 by oxidation at 1100 °C in air for 2 h [16]. Beyond filling the crack gap the healing products displayed similar hardness , toughness and CTE values as the original matrix [16].

1.3. Scientific Challenges

The great potential of MAX phase materials lies in their unique mix of properties. The ability of self-healing could set them even further apart from competing high temperature materials. Many steps remain until full industrial exploitation is reached. A systematic approach to identifying, investigating and analyzing self-healing materials is required to advance the field and progress the development of self-healing materials, not only MAX phases. An initial theoretical step is necessary to motivate and reduce the experimental efforts. Can simple rules of selection for self-healing materials be postulated to predict the self-healing ability of a material?

Synthesis of high purity dense bulk MAX phase ceramics can be achieved by multiple methods with varying success. High sensitivity to starting powder ratios, temperature profiles and applied pressure require precise recipes for every attempted compound. Carbide and intermetallic impurities can be observed by XRD and SEM to ensure they are at their lowest level possible.

The variety and versatility of self-healing materials seemingly causes a lack of consensus on quantification methods for healing efficiency. Visual observation, for example in the scanning electron microscope (SEM) is commonly the first step to assess the filling of micro-cracks. To further analyse the regain of certain properties different tests can be carried out, such as Fourier Transform Infrared Spectroscopy (FTIR), acoustic emission [22] or scratch or bending tests [23]. Bending tests used for brittle materials are, however, high in material consumption and do not actually measure the properties of the crack-healing material [23, 24].

To assess the self-healing properties of sintered materials, and to evaluate fracture toughness and strength of each sample a new test method is required. Controlled cracking, e.g. location and size, and minimized material consumption should be an upfront premise. Use of ceramic components in combustion environments is commonly stated as a justification for the high temperatures necessary to activate healing [11, 25]. Healing of high temperature ceramics has never been demonstrated under application conditions. The crack gap filling and strength recovery have thus far only been documented under ideal laboratory conditions. The effect of temperature or oxygen partial pressure fluctuation is yet to be demonstrated. Oxygen levels in such settings will be well below those of ambient air.

Goal of this work is to systematically investigate the self-healing potential of MAX-phases, from their theoretical potential (Chapter 2) to an actual application environment

(Chapter 7). To facilitate this, criteria for predicting self-healing potential are postulated, a new method to test self-healing in brittle ceramics is developed and two selected MAX phases are synthesized and tested for their self healing ability.

1.4. Thesis Outline

Chapter 2 addresses a new theoretical investigation into the concept of self-healing in MAX phase ceramics, as a result of their oxidation behavior. A simple and widely applicable approach of evaluating known material properties, such as Gibbs Free Energy (G) and diffusion coefficients, is used to predict and select potentially self-healing MAX-phase compounds from known data on 211 and 312 phases.

In chapter 3 and 4, the measurement of fracture properties of a healed sample and experimental challenges to quantify self-healing are discussed. Controlled crack formation in Ti_2AlC and Ti_3SiC_2 is achieved by the development of a new test setup and a new sample geometry. Paired with finite element modeling the fracture properties, fracture toughness and strength, can be extracted while creating a stable crack for oxidizing and healing experiments. Chapter 4 is a further development on the methodology whereby oxidative healing events in spark plasma sintered Ti_2AlC can be quantified in one sample.

In chapters 5 and 6 specific MAX-phases are addressed and investigated starting from their synthesis via pressureless or spark plasma sintering to their oxidation behavior concluding in determination of their crack-healing capacity. Chapter 5 focuses on Ti_3SiC_2 and its healing behavior as a bulk material. Chapter 6 concentrates on Ta_2AlC and its oxidation behavior at lower temperatures (<800 °C).

Chapter 7 concludes the thesis and presents a demonstration of various self-healing materials under application relevant conditions. Two pre-damaged MAX phases (Cr_2AlC and Ti_2AlC) and a cracked ceramic composite (Al_2O_3/TiC) are exposed to realistic conditions in a lab scale combustor. At temperatures of 1100 °C and a lower oxygen partial pressure than in lab experiments they show crack-healing behavior. This study is a first and important step to bridge the gap towards industrial utilization.

References

[1] P. D. Mangalgiri, *Composite materials for aerospace applications,* Bulletin of Materials Science **22**, 657 (1999).

[2] W. D. Callister and D. G. Rethwisch, *Materials science and engineering: an introduction*, 7th ed., Vol. 7 (Wiley New York, 2007).

[3] S. van der Zwaag, ed., *Self healing materials: an alternative approach to 20 centuries of materials science* (Springer, Dordrecht, the Netherlands, 2007).

[4] S. R. White, N. Sottos, P. Geubelle, J. Moore, M. Kessler, S. Sriram, E. Brown, and S. Viswanathan, *Autonomic healing of polymer composites,* Nature **409**, 794 (2001).

[5] S. van der Zwaag and E. Brinkman, eds., *Self Healing Materials - Pioneering Research in the Netherlands* (IOP Press, Amsterdam, The Netherlands, 2015).

[6] M. D. Hager, P. Greil, C. Leyens, S. van der Zwaag, and U. S. Schubert, *Self-healing materials,* Advanced Materials **22**, 5424 (2010).

[7] H. M. Jonkers, A. Thijssen, G. Muyzer, O. Copuroglu, and E. Schlangen, *Application of bacteria as self-healing agent for the development of sustainable concrete,* Ecological Engineering **36**, 230 (2010).

[8] S. Yoshioka and W. Nakao, *Methodology for evaluating self-healing agent of structural ceramics,* Journal of Intelligent Material Systems and Structures **26**, 1395 (2014).

[9] A. Susa, S. van der Zwaag, and S. J. Garcia, *Room temperature self healing polyetherimides based on a long chain aliphatic diamine,* in *Self healing materials - pioneering research in the Netherlands*, edited by S. van der Zwaag and E. Brinkman (IOP Press, the Netherlands, 2015) pp. 19–26.

[10] S. J. Kalista Jr, *Self-healing of thermoplastic poly (ethylene-co-methacrylic acid) copolymers following projectile puncture,* Master's thesis, Virginia Tech (2003).

[11] P. Greil, *Generic principles of crack-healing ceramics,* Journal of Advanced Ceramics **1**, 249 (2013).

[12] K. Ando, B. S. Kim, M. C. Chu, S. Saito, and K. Takahashi, *Crack-healing and mechanical behaviour of Al_2O_3/SiC composites at elevated temperature,* Fatigue & Fracture of Engineering Materials & Structures **27**, 533 (2004).

[13] F. F. Lange and T. K. Gupta, *Crack healing by heat treatment,* Journal of the American Ceramic Society **53**, 54 (1970).

[14] W. Sloof, A.-S. Farle, and L. Shen, *Intrinsic autonomous crack healing in MAX phase ceramics,* in *Self healing materials - pioneering research in the Netherlands*, edited by S. van der Zwaag and E. Brinkman (IOP Press, Amsterdam, The Netherlands, 2015) pp. 115–123.

[15] S. Li, L. Xiao, G. Song, X. Wu, W. G. Sloof, and S. van der Zwaag, *Oxidation and crack healing behavior of a fine-grained Cr_2AlC ceramic,* Journal of the American Ceramic Society **96**, 892 (2013).

[16] G. M. Song, Y. T. Pei, W. G. Sloof, S. B. Li, J. De Hosson, and S. van der Zwaag, *Oxidation-induced crack healing in Ti_3AlC_2 ceramics,* Scripta Materialia **58**, 13 (2008).

[17] G. M. Song, V. Schnabel, C. Kwakernaak, S. van der Zwaag, J. M. Schneider, and W. G. Sloof, *High temperature oxidation behaviour of Ti_2AlC ceramic at 1200°c,* Materials at High Temperatures **29**, 205 (2012).

[18] W. Jeitschko, H. Nowotny, and F. Benesovsky, *Kohlenstoffhaltige ternäre verbindungen (h-phase),* Monatshefte für Chemie / Chemical Monthly **94**, 672 (1963).

[19] W. Jeitschko, H. Nowotny, and F. Benesovsky, *Ti_2AlN, eine stickstoffhaltige h-phase,* Monatshefte für Chemie / Chemical Monthly **94**, 1198 (1963).

[20] W. Jeitschko, H. Nowotny, and F. Benesovsky, *Die h-phasen Ti_2InC, Zr_2InC, Hf_2InC und Ti_2GeC,* Monatshefte für Chemie und verwandte Teile anderer Wissenschaften **94**, 1201 (1963).

[21] M. W. Barsoum and T. El-Raghy, *Synthesis and characterization of a remarkable ceramic: Ti_3SiC_2,* Journal of the American Ceramic Society **79**, 1953 (1996).

[22] D. G. Bekas, K. Tsirka, D. Baltzis, and A. S. Paipetis, *Self-healing materials: A review of advances in materials, evaluation, characterization and monitoring techniques,* Composites Part B: Engineering **87**, 92 (2016).

[23] K. Ando, K. Furusawa, M. C. Chu, T. Hanagata, K. Tuji, and S. Sato, *Crack-healing behavior under stress of mullite/silicon carbide ceramics and the resultant fatigue strength,* Journal of the American Ceramic Society **84**, 2073 (2001).

[24] S. Li, G. Song, K. Kwakernaak, S. van der Zwaag, and W. G. Sloof, *Multiple crack healing of a Ti_2AlC ceramic,* Journal of the European Ceramic Society **32**, 1813 (2012).

[25] A.-S. Farle, C. Kwakernaak, S. van der Zwaag, and W. G. Sloof, *A conceptual study into the potential of $M_{n+1}AX_n$-phase ceramics for self-healing of crack damage,* Journal of the European Ceramic Society **35**, 37 (2015).

2

A conceptual study into the potential of $M_{n+1}AX_n$-phase ceramics for self-healing of crack damage

Healing is a matter of time,
but it is sometimes also a matter of opportunity.

Hippocrates

This chapter has been published in the Journal of the European Ceramic Society **35**, 37 (2015) [1]. Authors: Ann-Sophie Farle, Cees Kwakernaak, Sybrand van der Zwaag, Willem G. Sloof

Recently, autonomous crack-healing has been reported for Ti_2AlC and Ti_3AlC_2 both being $M_{n+1}AX_n$ (MAX) phase ceramics. The desirable healing behavior is due to the formation of a stable, well adhering oxide with a high relative volume expansion and having mechanical properties close to those of the matrix. The present analysis aims to predict the occurrence of similar autonomous high temperature crack healing behavior in other MAX phase materials on the basis of postulated primary and secondary criteria analyzing their reported thermodynamic, thermo-kinetic and mechanical properties. The analysis correctly identified Ti_2AlC and Ti_3AlC_2 as suitable MAX phase variants for autonomous high temperature crack healing. Also other Al-containing MAX phases seem promising, of which Ti_2AlC and V_2AlC were identified as worth a detailed investigation of their crack healing behavior. Of the Si-containing MAX phase compounds only Ti_3SiC_2 met the criteria for autonomous high temperature crack healing.

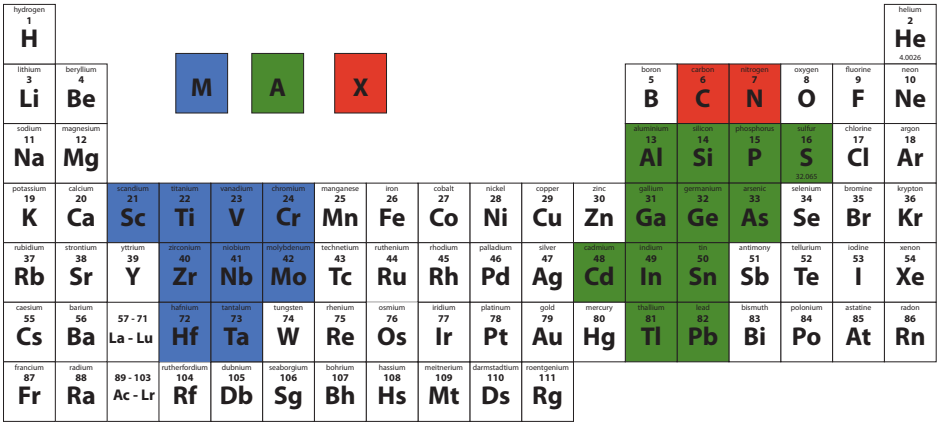

Figure 2.1: Periodic table with labeled $M_{n+1}AX_n$ phase components.

2.1. Introduction

Damage tolerance and prevention have been leading paradigms in the design of structural materials. However the principle of damage management as employed in self-healing materials is gaining increasing interest throughout all material classes [2–4]. Early approaches to heal micro cracks autonomously have employed embedded micro capsules containing a liquid healing agent in the matrix material such that upon the occurrence of a crack the healing agent 'flows' into the crack and restores mechanical integrity. The concept has been demonstrated to work successfully for concrete [5], polymeric systems [6] and oxide ceramics [7, 8], respectively. Recently, another route towards self-healing, applicable to an attractive high performance ceramic material without incorporation of discrete healing particles, has been discovered using a special form of oxidative filling of the crack. This principle of intrinsic self-healing was demonstrated for the first time with fine grained Ti_3AlC_2 [9]. Autonomous strength recovery and multiple crack-healing was also demonstrated for a related compound Ti_2AlC [10, 11].

Both ternary compounds belong to the family of so-called MAX phase materials [12–14]. The general formula is $M_{n+1}AX_n$, where n equals 1, 2 or 3, M is an early transition metal, A is an A group element (mostly IIIA and IVA, like Al and Si), and X is C or N, see Figure 2.1. The MAX phase compounds have an atomic layered and hexagonal crystal structure [12]. The crystalline unit cell contains two sub units, viz.: $M_{n+1}AX_n$ layers are interrupted by layers of pure A, which form an ABABAB structure. Due to their structure, MAX phase materials exhibit unique combinations of mechanical, thermal and electric properties some of which are common in metals and some of which are characteristic

for ceramics [12, 15]. Like conventional ceramics these MAX phases are stable up to high temperatures and are corrosion resistant [14–16]. The high thermal conductivity makes the MAX phases thermal shock resistant. Their static strength is maintained up to high temperatures, above which creep will become the limiting factor [17, 18].

Being a non-oxidic material the MAX phases will undergo oxidative decomposition at higher temperatures. The oxidation behavior varies from an excellent oxidation resistance (due to the formation of a protective oxide layer, as in Ti_2AlC) to a very poor resistance (leading to a fast and full conversion into the oxidic state, as in Hf_2SnC) [12]. Extensive studies on the so-called 211 and 312 Ti-Al-C compounds revealed the formation of a well-bonded protective Al_2O_3 layer at temperatures above 900 °C, as a result of the strong MX covalent bond in the MAX phase restricting the activity of Ti [19]. The desirable oxidation behavior of Ti_3AlC_2 has been utilized to heal cracks with an average width of 5 µm during high temperature annealing in air [9]. Multiple filling of sequentially opened cracks has been demonstrated for Ti_2AlC making use of the regain of the initial oxidation resistance provided by the Al_2O_3 scale [20].

Such a combination of excellent high temperature properties and autonomous high temperature crack healing behavior would make MAX phase materials attractive candidates for high temperature applications, where the material is exposed to thermal cycles, mechanical loading and oxidation. These conditions are encountered in e.g. power or propulsion generation equipment, raw material production and recycling facilities.

The present work aims at identifying equally desirable crack healing behavior for other compounds among the more than 75 $M_{n+1}AX_n$ phases ($n < 3$) known, see Table 2.1. The evaluation of the expected oxidation and crack-healing behavior as of all 211 and 312 MAX phases is performed on the basis of six postulated criteria.

2.2. Self-Healing of $M_{n+1}AX_n$-phase ceramics

Extrinsic or intrinsic self-healing behavior requires that at least three minimal requirements are met: the healing agent must i) 'flow' to the crack, ii) fill the volume opened by the crack and iii) adhere to crack surfaces [2]. In the case of $M_{n+1}AX_n$ phases oxidation at the crack surfaces leading to a sufficient volume expansion substitutes the 'flow' requirement. Hence, the high temperature crack healing potential of MAX phase materials can be evaluated by a simultaneous analysis of four postulated primary criteria: preferential oxidation of the A-element, fast diffusion of A-element, volume expansion upon oxidation and adhesion of the oxidation product to the matrix. Furthermore, the mechanical quality of the crack filling oxide is evaluated by comparing its Young's modulus and coefficient of thermal expansion with the parent MAX phase. The latter two criteria are considered at the secondary criteria bringing the total number of criteria to be evaluated for MAX phase compounds as yet not-tested for their high temperature healing potential to six.

Of the 12 A-elements considered for MAX-phases arsenic, phosphor, sulfur and lead can be excluded 'a priori' due to the low melting or sublimation points of their oxides. As a result the remaining MAX phase compounds to be evaluated only contain Al, Si, Ge, Ga, In, Sn, Tl or Cd as the A element. This selection excludes $M_{n+1}AX_n$ phases with $n \geq 3$.

Table 2.1: Table of known $M_{n+1}AX_n$ with $n \leqslant 3$ phases by M and A element

M/A	Al	Si	Ge	Ga	As	P	S	In	Sn	Tl	Pb	Cd	c
Ti	Ti_2AlC Ti_2AlN Ti_3AlC_2 Ti_3AlN_2	Ti_3SiC_2 Ti_2SiC[a] Ti_2SiN[a]	Ti_2GeC Ti_3GeC_2	Ti_2GaC Ti_2GaN	Ti_2AsC[b]	Ti_2PC[b]	Ti_2SC	Ti_2InC Ti_2InN	Ti_2SnC Ti_3SnC_2	Ti_2TlC	Ti_2PbC	Ti_2CdC	21
Cr	Cr_2AlC	Cr_3SiC_2[d] Cr_2SiC[d]	Cr_2GeC	Cr_2GaC Cr_2GaN		Cr_2PC[d]	Cr_2SC[d]						8
V	V_2AlC V_3AlC_2[c]	V_3SiC_2[a] V_2SiC[a]	V_2GeC	V_2GaC V_2GaN	V_2AsC	V_2PC	V_2SC[d]						10
Sc	Sc_2AlC			Sc_2GaC[d] Sc_2GaN[d]				Sc_2InC[d]		Ti_2TlC[d]			5
Nb	Nb_2AlC Nb_4AlC_3	Nb_3SiC_2[a]	Nb_2GeC[c]	Nb_2GaC	Nb_2AsC	Nb_2PC	Nb_2SC	Nb_2InC	Nb_2SnC				10
Mo		Mo_3SiC_2[d]		Mo_2GaC									2
Zr	Zr_2AlC[d] Zr_2AlN[d]	Zr_3SiC_2[d]					Zr_2SC	Zr_2InC Zr_2InN	Zr_2SnC	Zr_2TlC Zr_2TlN	Zr_2PbC		10
Hf	Hf_2AlC[d] Hf_2AlN[d]	Hf_3SiC_2[d]					Hf_2SC[d]	Hf_2InC	Hf_2SnC Hf_2SnN	Hf_2TlC	Hf_2PbC		9
Ta	Ta_2AlC Ta_3AlC_2	Ta_3SiC_2[d]		Ta_2GaC									4
c	16	12	5	11	3	4	6	7	6	5	3	1	79

[a] Stable and metastable.
[b] Unstable.
[c] Synthesized as thin film.
[d] Calculated data available.

2.2.1. Preferential oxidation of A-element

A simplified prediction of the oxidation sequences in multi-compound systems can be obtained from the Gibbs free energy of oxide formation (ΔG^0) of its pure constituents. Plots of the Gibbs free energy values of oxidation reactions versus temperature normalized to 1 mol of O_2 are referred to as Ellingham diagrams [21]. The more negative the Gibbs free energy of oxide formation is, the more stable the oxide will be. Thus the element in the MAX phase that forms the most stable oxide (i.e. with the lowest ΔG^0) may be selectively oxidized [22]. The ΔG^0 values of the possible A- and M-oxides at room temperature against their respective melting temperatures are shown in Figure 2.2.

Oxides ranging in the lower values for ΔG^0 are more stable and thus are more likely to form than competing oxides with less negative values. When aiming for A-element oxidation it is necessary to identify M-elements for which M-A combinations would favour the formation of an A-oxide. For instance, Al_2O_3 has been shown to be the healing product in case of oxidation of Ti and Cr containing Al-based MAX phases [20, 23], in accordance with the data in Figure 2.2. All M-oxides, other than Sc_2O_3 have a less negative value of ΔG^0, making them less likely than that of Al_2O_3. In general the oxidation reactions of the M-oxides have lower values than the A-elements Al and Si. Oxidation of the Ti-Ge-C 312 and 211 MAX phases, for example, leads to formation of rutile and only minor amounts of GeO_2 [24, 25]. The observed preferential TiO_2 formation corresponds with the lower ΔG^0 of the Ti oxidation reaction than that of GeO_2. Thallium, tin, germanium and indium are unlikely to form a stable oxide when competing with possible

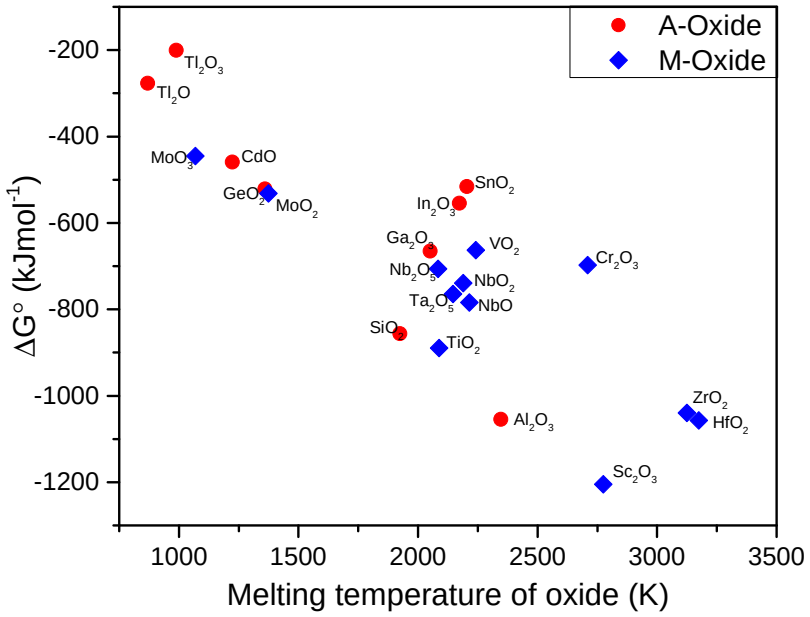

Figure 2.2: Standard Gibbs free energy of oxide formation for selected MAX phase constituents.

M-element oxidation. The M-element, molybdenum can be combined with the highest number of group A-elements (Ga, In, Si and Al).

Evaluating the Gibbs energy of oxide formation (see Figure 2.2) the Al containing 312 and 211 MAX phases Ti_2AlC, Ti2AlN, Ti_3AlC_2, Ti3AlN2, Cr_2AlC, Cr_3AlC_2, V_2AlC, V_3AlC_2, Nb_2AlC, Zr_2AlC, Zr_2AlN, Ta_2AlC and Ta_3AlC_2 are likely to preferentially form Al_2O_3 upon oxidation while at the same time suppressing the formation of M-oxides. Similarly, some Si containing MAX phases feature a higher ΔG^0 for their M-oxides than SiO_2. However to date only Ti_3SiC_2 has been successfully synthesized. Other MAX phases have been predicted by ab initio calculations, but have not been synthesized yet, cf. Table 2.1. Of these theoretical MAX phases, the following compounds may fulfill the criterion of preferential oxidation of the A-element as well: Cr_2SiC, Cr_3SiC_2, V_2SiC, V_3SiC_2, Nb_3SiC_2, Mo_3SiC_2, and Ta_3SiC_2. Additionally Mo_2GaC is also a candidate for preferential oxidation of the A-element.

The displayed ΔG^0 values correspond to an activity of one for each element while by approximation the activities of A elements should be normalized to the atomic fraction of the element. However, such a refinement does not change the relative order of the oxide stabilities.

In case of small ΔG^0 differences between A- and M-elements, the competing oxidation reactions can lead to mixtures (layering) of different oxidation products and ternary

oxides with possible beneficial attributes. An example of such is the ternary oxide $ZrSiO_4$, formed between SiO_2 and ZrO_2 ($\Delta G^0 = -176\,kJ\,mol^{-1}$). Other possibilities among the considered M- and A-oxides are Tl_2CrO_4 and Al_2TiO_5 . The former can form at temperatures above 126 °C while Al_2O_3 and TiO_2 do not react below 1226 °C.

2.2.2. Dominant diffusion of A-element

At the initial stages of crack healing by selective oxidation of the A- or M-element in the MAX phase at the fresh fracture surface the diffusion rate of the most reactive element will determine the kinetics, whereas at the later stages the rate of diffusion of oxygen through the existing oxide at the fracture surface may govern the kinetics [26].

In MAX phase ceramics, which have a layered hexagonal structure with MX-groups separated by pure A-element layers [12], weak MA bonds compared to strong MX bonds favour fast transport of the A-element, due to a higher atom mobility [27, 28]. Strong covalent bonds in the $M_{n+1}AX_n$ layers restrain the movement of the transitional metals, while constituents of groups 13 and 14 (A-elements) are comparatively mobile. Hence anisotropy in atom mobility is observed parallel and perpendicular to the basal plane of the hexagonal MAX phase crystal structure [29].

Few studies have investigated the orientation dependent propagation of constituents within the layered hexagonal structure of the $M_{n+1}AX_n$ phases. Based on an interdiffusion study of Si-, Ge- and Al-containing MAX phases it can be estimated that the diffusion of A-elements is faster by a factor of at least 200 than the diffusion of the M-elements [30]. In the subsequent analysis we simplify the problem by considering the diffusion in the $M_{n+1}X_n$ and A layers separately. By comparing the diffusivity of M-elements in their respective carbides to the self-diffusivity of A-elements, the atomic propagation behavior parallel to the basal plane can be predicted.

The migration energy of Al in Ti_2AlC, with a value of 0.83 eV, is slightly higher than the self-diffusion value in Al, but lower than that in TiAl, 0.61 eV and 1.23 eV respectively [31]. In an ensuing publication, Liu et al. [32] compared the Al migration energy to that of other A-elements Sn, Ga, Cd, In and Pb in Ti_2AC, concluding that all values were lower than for diffusion of Al in Ti_2AlC, with 0.66, 0.75, 0.53, 0.63, and 0.10 eV respectively. These results support the reasoning for using our simplified approach to approximate the initial diffusion behavior of MAX phase ceramics.

The Arrhenius plot of selected diffusion data for M elements in their respective carbides and A-elements is shown in Figure 2.3 [33–37]. Although each data set is restricted to a different temperature regime, a clear general trend of accelerated self-diffusion can be distinguished. Aluminum, indium and tin, according to Figure 2.3, diffuse faster along the basal plane of a titanium containing MAX phase, encouraging their selective oxidation.

Reviewing the Arrhenius plot also indicates that a faster diffusion and hence a faster oxidation is to be expected for Al, In, and Sn when in combination with any of the shown M-carbides or nitrides. Si diffusion is favorable in most combinations, but could be slower than the diffusion of V in VC and Zr in ZrN. This leaves Ti_2AlC, Ti_3AlC_2, V_2AlC, V_3AlC, Nb_2AlC, Zr_2AlC, Zr_2AlN, Ti_2SnC, Ti_3SnC_2, Nb_2SnC, Zr_2SnC, Ti_2InC, Nb_2InC, Zr_2InC, Zr_2InN, Ti_3SiC_2 and the theoretical Nb_3SiC_2, Zr_3SiC_2 as the potentially attractive crack healing MAX phases.

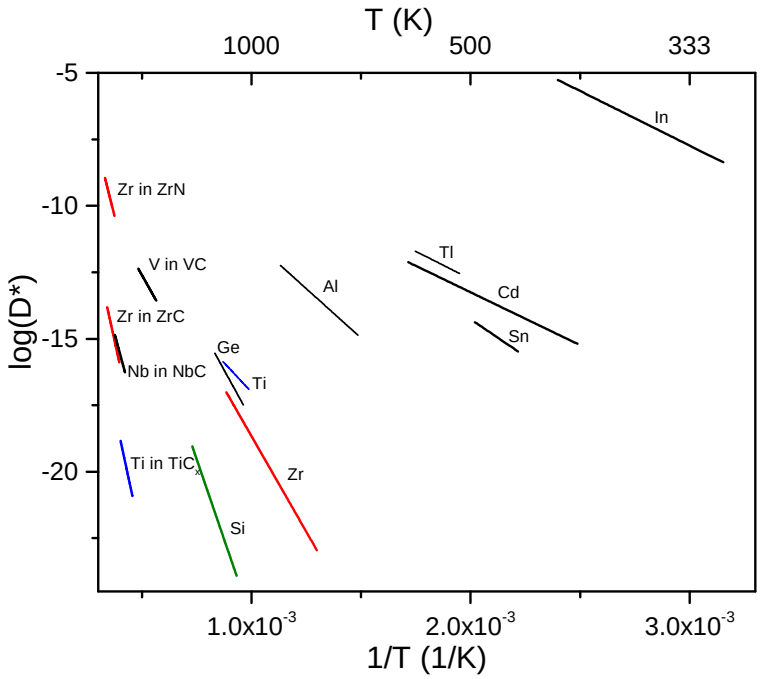

Figure 2.3: Arrhenius plot of diffusion coefficients of selected metals through their respective carbides and the self-diffusion of A-elements.

In the present analysis MAX-phases containing Ta, Cr, Hf, Ga and/or Nb were not considered due to a lack of data for their self-diffusion or transport through their respective carbides and nitrides.

Having discussed the supply of A- or M-atoms to the reaction interface, it is important to keep in mind that at longer time scales oxide growth is governed by inward diffusion of oxygen. Al_2O_3 is an excellent inhibitor of further oxidation, and being responsible for the good oxidation resistance attributed to such materials as Ti_2AlC and Ti_3AlC_2. Hence for the healing of wider cracks or for multiple healing events at smaller cracks, the time to heal properly increases significantly with the thickness of the oxide layer formed. If the oxidation of the MAX phase was to lead to the formation of ZrO_2, such an oxide would allow continuous transport of oxygen to the underlying matrix, ultimately never sealing the exposed area [38].

2.2.3. Volume expansion upon oxidation

In contrast to intrinsic self-healing in polymers, where cracks are healed by a 'zipper-effect', bringing together the two opposing crack surfaces, thermal oxidation aims to fill the void with new material. Thus the filling material must take up a certain volume to fully seal any crack damage. Two extreme oxidation scenarios for MAX phase ceramics

are to be considered: i) a full oxidation where all constituents, the transition metal, the A-element and carbon (or nitrogen) oxidize and ii) a situation in which only the A-element reacts with the atmosphere providing the healing agent.

The relative volume expansion (RVE) due to oxidation of the A-element and assuming that the MAX phase maintains its structure and volume with an increase in A-element vacancies follows from:

$$M_{n+1}AX_n \longrightarrow M_{n+1}A_{1-x}X_n + xAO_v \tag{2.1}$$

Hence,

$$\text{RVE} = \frac{V_{M_{n+1}A_{1-x}X_n} + xV_{AO_v}}{V_{M_{n+1}AX_n}} \approx 1 + \frac{xV_{AO_v}}{V_{M_{n+1}AX_n}} \tag{2.2}$$

Considering the maximum tolerable Al depletion for Ti_2AlC of up to $Ti_2Al_{0.5}C$, as calculated by Wang et al. [39] and subsequent oxidation of Al without TiO_2 formation, Equation 2.1 yields a total relative volume increase of 38.5% (RVE=1.385) based on a molar volume of 25.574 cm^3 of Al_2O_3 and a molar volume of 33.182 cm^3 for Ti_2AlC. Changes in volume will hereafter be represented by the relative molar volume expansion (RVE) of products to matrix [Equation 2.2 and 2.4].

Full oxidation of the MAX Phase ceramics would lead to formation of M- and A-oxides (Equation 2.3) while the carbon or nitrogen oxidizes to a gaseous phase not contributing to the volume expansion. A comparison of initial volume to the solid oxide product volume shows the expansion potential. Overall, a full MAX phase disintegration leads to a higher volume increase than partial oxidation due to higher oxygen uptake.

$$M_{n+1}AX_n \longrightarrow (n+1)MO_{V_M} + AO_{V_A} + nXO_{V_x} \tag{2.3}$$

$$\text{RVE} = \frac{(n+1)V_{MO_{V_M}} + xV_{AO_{V_A}}}{V_{M_{n+1}AX_n}} \tag{2.4}$$

For example, the formation of Al_2O_3 and TiO_2 upon full degradation of Ti_2AlC with loss of C in the form of gaseous CO or CO_2 and excluding mixed oxide formation, would theoretically yield a relative volume expansion of 1.52, an increase of 9.6% compared to the previously shown partial oxidation.

An optimal crack filling MAX phase will maintain its stability with minimal decomposition among A-element depletion and have a relative volume expansion greater than 1 (RVE $\geq$ 1). Fortunately, all MAX phase compounds have a RVE greater than 1, see Figure 2.4a and b. Most investigated MAX phases show a relative volume expansion for partial oxidation of the A-element between 1.4 and 1.6. The highest values are calculated for Ge-containing compounds especially Cr_2GeC with a RVE of 1.9. Cd oxidation on the other hand leads to the lowest relative expansion with an RVE of only 1.1.

The two oxidation scenario's showing the highest relative volume expansion are those for Cr_2GeC, V_2GeC, Ti_2GeC and Ti_3SiC_2. These can thus be considered most promising for larger crack gap filling.

In practice, contrary to the previously assumed scenarios, a combined and complex oxidation and decomposition reaction is most likely to occur and has commonly been

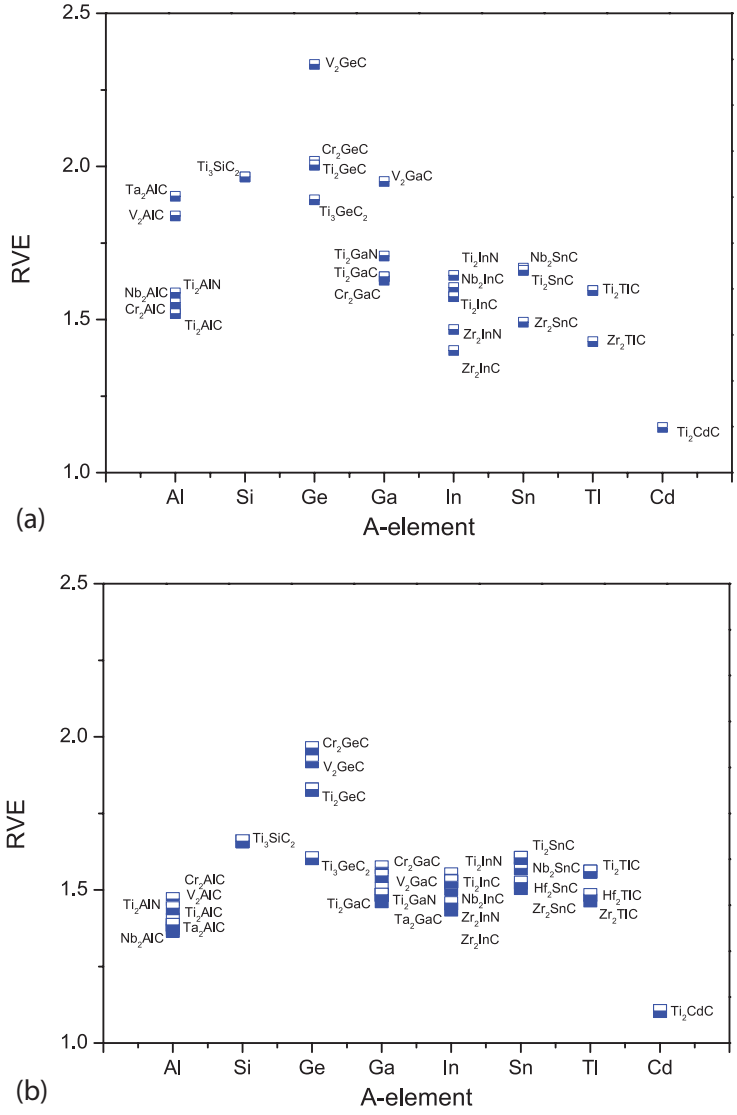

Figure 2.4: Relative Volume Expansion (RVE) (a) upon partial oxidation of the A-element and (b) upon full oxidation of the MAX phase.

reported [40–42]. For example, studies have shown that the oxidation of Ti_2AlC proceeds via a two-step process, where a combined TiO_2 and Al_2O_3 formation occurs, but the crack filling and healing reaction is dominated primarily by the Al_2O_3 formation [42][38]. Furthermore, consumption of the group 13 element leads to a depletion zone, usually consisting of the binary metal carbide such as Cr_7C_3 in Cr_2AlC, or a Ti enriched layer in Ti_2AlC, between oxide and original material [23, 43]. The thickness and thus volume of said depletion zone depends strongly on the diffusion rate of A-elements to the reaction surface as well as the oxygen permeability of the surface oxide [44, 45].

2.2.4. Adhesion

Strength recovery of MAX phase ceramics after healing cracks by selective oxidation is only possible when the adhesion between the oxide filling the crack gap and the parent MAX phase is of a sufficient level to restore its load bearing capacity. In such a case, the energy required to separate the healing oxide from the MAX phase should be comparable or larger than the cohesion of the MAX phase. This adhesion energy of the interface between the MAX phase and the oxide is defined as the 'work of adhesion' [46]:

$$W_{ad} = -(\gamma^{surf}_{MAX} + \gamma^{surf}_{oxide}) + \gamma^{interface}_{MAX/oxide} \tag{2.5}$$

The surface energies of the MAX phase (γ^{surf}_{MAX}) and the oxide (γ^{surf}_{oxide}) are estimated from the surface enthalpy of each element that constitutes the interface weighted by the molar surface density [47, 48]. The interface energy ($\gamma^{interface}_{MAX/oxide}$) is determined by the interaction energies of the atoms at either site of the interface. These interaction energies are estimated from solution enthalpies of an element at one side of the interface dissolved in another element at either side of the and vice versa. Data on the enthalpy of solutions are scarce, but can be estimated using a semi-empirical macroscopic atom model [48]. A detailed description of such calculations can be found elsewhere [49].

To demonstrate the approach, the work of adhesion of the interface between the A-element oxide and the parent MAX phases Ti_2AlC (Ti_3AlC_2), Ti_3SiC_2 and Ta_2AlC was calculated, see Figure 2.5. For the Al-containing MAX phases, two interfaces were considered, viz. $M_{n+1}AX_n$ (0 0 0 1)//α-Al_2O_3(1 1 -2 0) and $M_{n+1}AX_n$ (1 1 -2 0)//α-Al_2O_3(1 1 -2 0), respectively, with different terminations of the MAX phase lattice; see Figure 2.6. For Ti_3SiC_2 the interfaces with α-cristobalite (1 1 1) and rutile (1 1 0) were analyzed.

In all cases the interface with $M_{n+1}AX_n$ (0 0 0 1) terminated by the M-element offers the strongest adhesion (9 Jm^{-2} for Ti_3AlC_2 and Ti_2AlC, and 11 Jm^{-2} for Ta_2AlC), while the interface with $M_{n+1}AX_n$ (1 1 -2 0) has an adhesion level between 1 to 3 Jm^{-2} lower. The adhesion between Ti_3SiC_2 and the oxides differs substantially between α-cristobalite (approx. 6.7 Jm^{-2}) and rutile (approx. 9.8 Jm^{-2}). Compared to the cohesion of the MAX phases (approx. 7 Jm^{-2} for the bonding between the A and MX layers) the adhesion between MAX and oxide is always stronger. Hence, for the optimal self-healing MAX phases aimed for in this analysis, full strength recovery is anticipated provided a full filling of the original crack volume is obtained.

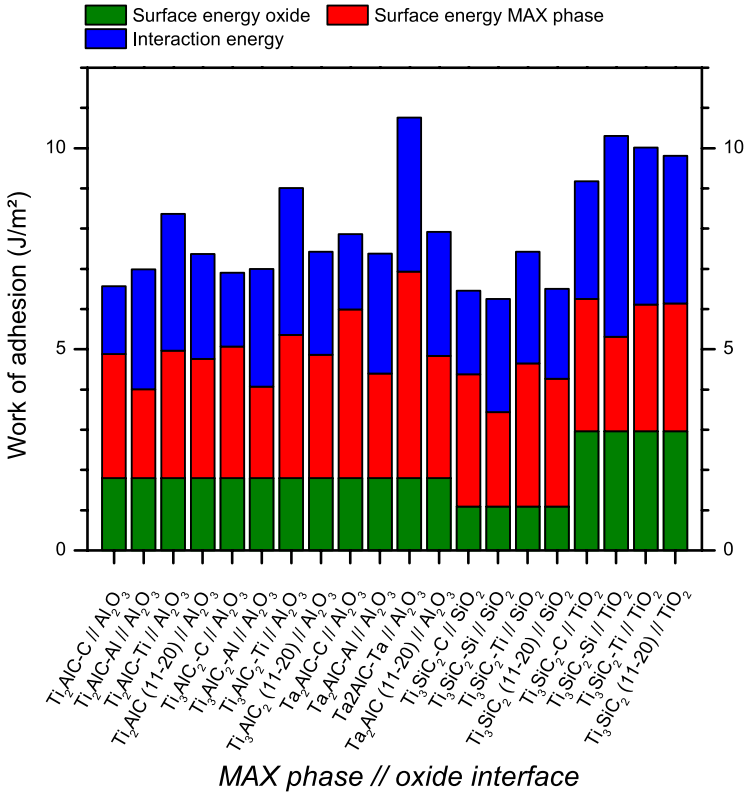

Figure 2.5: The work of adhesion for various MAX phases and their A-element oxide. The MAX phases with (0001) oriented surfaces terminate with C, M (=Ti, Ta) or A (=Al, Si) and are designated as $M_{n+1}AC_n$ – terminating elements. The oxide surface orientation is (11-20), (111) and (110) for Al_2O_3, SiO_2 and TiO_2, respectively, and terminate with oxygen atoms (except TiO_2 which also has Ti atoms at its surface).

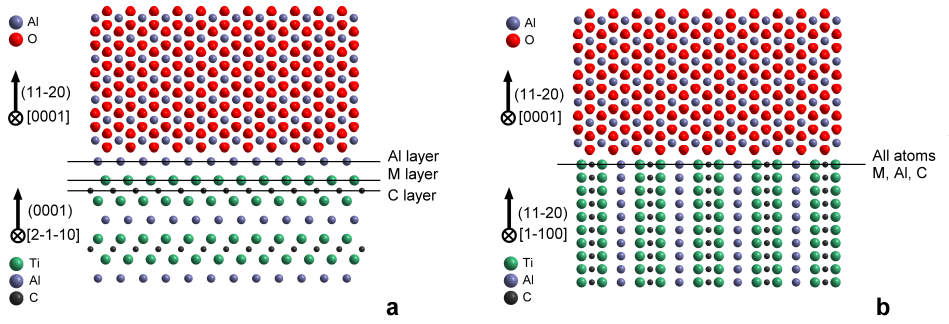

Figure 2.6: The interfaces considered are (a) MAX-phase (0001) // Al_2O_3 (11-20) and (b) MAX-phase (11-20) // Al_2O_3 (11-20) (b). The possible terminations of M- and A-element and C-atoms of the MAX phase are indicated by the solid lines. The composition of the (11-20) terminating plane of the MAX-phase in (b) does not change with depth and all elements are present.

2.3. Properties of the healed MAX-phase

Micro-cracks are filled with an oxide generated by selective oxidation of one or more constituents, resulting in a 'scar zone' with possibly different mechanical, thermal and electrical properties. For optimal self-healing MAX phases the thermo-mechanical properties of this reaction product should not deviate too much from those of the original MAX phase compound. To this end two additional secondary criteria are imposed to define MAX phase compounds with optimal healing characteristics.

2.3.1. Match of the coefficients of thermal expansion (CTE)

Not only the formation of new phases leads to volume changes. Also temperature changes lead to (smaller) volume changes. For the healed crack to be insensitive to temperature changes and not to open again due to thermal stresses, it is favourable to ensure a minimal mismatch in thermal expansion coefficients between matrix and healing agent. If a large difference in expansion behavior occurs, stresses can be induced leading to new crack formation or spallation [9].

The known coefficients of thermal expansion known for MAX phases and for their A-oxides are displayed in Figure 2.7. Assuming healing by selective oxidation of the A-element, the healed zone will consist of A-oxide only. Ignoring any stresses due to oxide growth, ideally there is no mismatch in thermal expansion and thus no risk of stress development due to temperature fluctuations. If the healed zone has a smaller CTE than the original matrix compressive stresses can be expected in the oxide upon cooling, which may be tolerated. Stronger expansion or shrinkage of healing agent in comparison to the MAX phase may result in undesirable tensile stresses in the brittle healed zone. Hence compounds for which the CTE of the A-oxide is substantially higher than that of the MAX phase are considered to be less suitable.

Almost perfect CTE matching can be found in Ta_2AlC with the MAX phase having an expansion value of 8.3 x 10^{-6} K^{-1}, compared to a CTE of 8.5 x 10^{-6} K^{-1} for alumina, a deviation of just 2.3%. Very close matching is also observed for Ti_2AlC, Nb_2AlC, Ti_3AlC_2 and

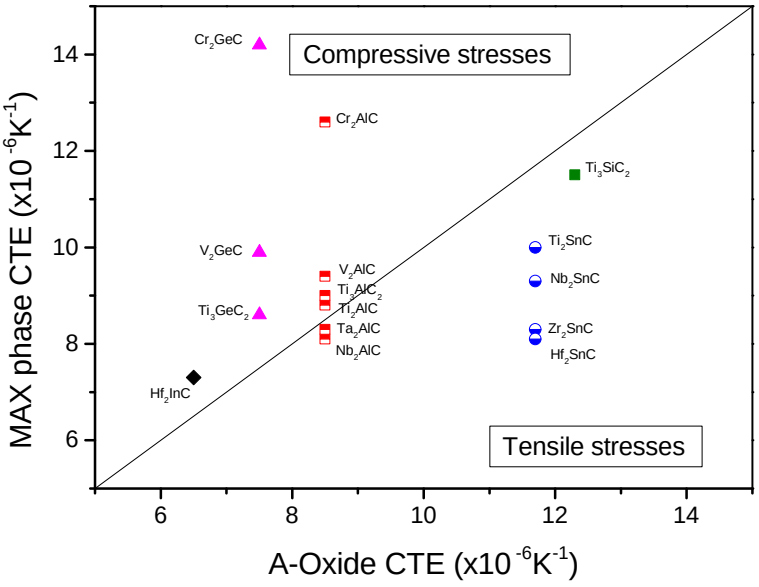

Figure 2.7: Coefficient of thermal expansion (CTE) for MAX phases and A-element oxides.

Ti_3SiC_2 with small differences in coefficients of thermal expansions of 3.5%, 4.7%, 5.9% and 6.5%, respectively. Hf_2InC, Ti_3GeC_2, V_2GeC, Cr_2GeC, Cr_2AlC and V_2AlC would also be potentially attractive MAX phase compounds since the expected mismatch would cause compressive stresses within the scar zone upon cooling.

2.3.2. Match of the Young's moduli

The relative Young's or Elastic moduli of the oxide formed and the original compound also play a role in the mechanical stability of the healed crack, in particular for fully healed cracks. If the Young's modulus of the oxide is lower than that of the parent phase, the stresses in the scar zone remain low and there is no stress concentration at the scar region upon external mechanical loading. However, if the Young's modulus of the oxide is higher, there is a concentration of stress in the scar region upon external mechanical loading, leading to preferential re-cracking of the healed region.

Available data for elastic moduli of MAX phases and their respective A-oxides are shown in Figure 2.8. The formed oxides generally display a high stiffness, which can deviate significantly from that of the relatively flexible parent MAX phase. Tin containing compounds show a maximum deviation of approximately 30%, where only Ti_2SnC has a higher modulus than the healing agent.

Ti_3SiC_2, Ti_2SnC, as well as Ta_2AlC, Ti_3AlC_2, Ti_2AlN, Ti_2AlC, Hf_2SnC and Nb_2SnC can be considered to have well matching A-oxides because of a relative modulus difference less than 30%.

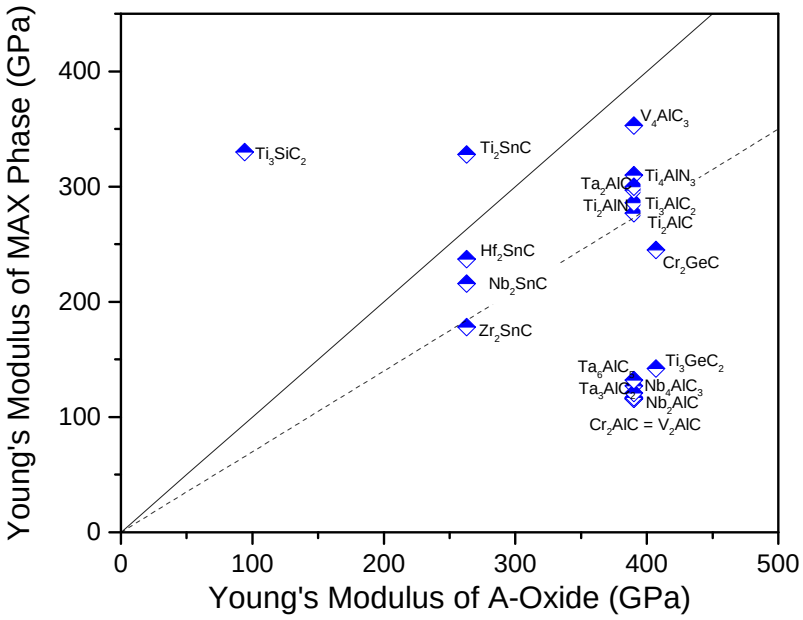

Figure 2.8: Young's Moduli of MAX phases and their respective A-element oxides. Upon loading negligible stresses in oxide if: $E_{MAX} > E_{oxide}$ (see straight line). Significant stresses can arise when E_{oxide} is more than 30% larger than E_{MAX}; see dotted line.

2.4. Conclusions

Evaluation of the primary selection criteria for self-healing MAX phase compounds being the formation of a stable (non-oxygen transparent) oxide upon selective oxidation of the A-element, a relatively high diffusivity of the A-element to ensure fast oxidation, a sufficient volume expansion to fill a crack gap and a good adhesion correctly identified known self-healing MAX phases, Ti_2AlC, Ti_3AlC_2 and Cr_2AlC as being optimal candidates. Ti_3AlC_2 and Ti_2AlC also meet secondary selection criteria as comparable coefficient of thermal expansion (CTE) and Young's Modulus of the healing oxide than that of the parent MAX phase matrix. Cr_2AlC, however, has a larger CTE than the healing oxide, which may lead to compressive stresses in the healed region.

Additional MAX phase compounds that fulfill the requirements for crack healing, by high temperature selective oxidation, are V_2AlC, V_3AlC_2, Nb_2AlC, Zr_2AlC, Zr_2AlN and Ti_3SiC_2. Crucial diffusion data for Mo_2GaC, Cr_2AlC, Cr_3AlC_2, Ti_2AlN, Ti_3AlN_2, Ta_2AlC and Ta_3AlC_2 lacking, yet these compounds meet all other primary criteria. For all MAX phases meeting the primary scrutiny the adhesion energy between the healing oxide and the adjacent MAX phase is in all cases higher than its cohesion energy.

Evaluation of the secondary criteria reveals Ta_2AlC, Ti_3SiC_2 and Ti_2AlC are likely to demonstrate optimal self-healing properties.

References

[1] A.-S. Farle, C. Kwakernaak, S. van der Zwaag, and W. G. Sloof, *A conceptual study into the potential of $M_{n+1}AX_n$-phase ceramics for self-healing of crack damage,* Journal of the European Ceramic Society **35**, 37 (2015).

[2] S. van der Zwaag, N. H. van Dijk, H. M. Jonkers, S. D. Mookhoek, and W. G. Sloof, *Self-healing behaviour in man-made engineering materials: Bioinspired but taking into account their intrinsic character,* Philosophical Transactions: Mathematical, Physical and Engineering Sciences **367**, 1689 (2009).

[3] H. Mihashi and T. Nishiwaki, *Development of engineered self-healing and self-repairing concrete-state-of-the-art report,* Journal of Advanced Concrete Technology **10**, 170 (2012).

[4] A. Stankiewicz, I. Szczygieł, and B. Szczygieł, *Self-healing coatings in anti-corrosion applications,* Journal of Materials Science **48**, 8041 (2013).

[5] C. M. Dry, *Three designs for the internal release of sealants, adhesives, and waterproofing chemicals into concrete to reduce permeability,* Cement and Concrete Research **30**, 1969 (2000).

[6] G. Galgali, E. Schlangen, and S. van der Zwaag, *Synthesis and characterization of silica microcapsules using a sustainable solvent system template,* Materials Research Bulletin **46**, 2445 (2011).

[7] K. Ando, B. S. Kim, M. C. Chu, S. Saito, and K. Takahashi, *Crack-healing and mechanical behaviour of $Al_2O_{3/}SiC$ composites at elevated temperature,* Fatigue & Fracture of Engineering Materials & Structures **27**, 533 (2004).

[8] T. Osada, W. Nakao, K. Takahashi, and K. Ando, *Kinetics of self-crack-healing of alumina/silicon carbide composite including oxygen partial pressure effect,* Journal of the American Ceramic Society **92**, 864 (2009).

[9] G. M. Song, Y. T. Pei, W. G. Sloof, S. B. Li, J. De Hosson, and S. van der Zwaag, *Oxidation-induced crack healing in Ti_3AlC_2 ceramics,* Scripta Materialia **58**, 13 (2008).

[10] G. M. Song, *11 - self-healing of max phase ceramics for high temperature applications: evidence from Ti_3AlC_2,* in *Advances in Science and Technology of Mn+1axn Phases*, edited by I. M. Low (Woodhead Publishing, 2012) pp. 271–288.

[11] X. Yang, J. Wan, C. Dai, Y. Zhang, W. Mao, Y. Zhou, and C. Lu, *Finite element analysis of crack propagation and fracture mechanical properties of freestanding 8 wt.% Y_2O_3–ZrO_2 coatings,* Surface and Coatings Technology **223**, 87 (2013).

[12] M. W. Barsoum, *The $M_{n+1}AX_n$ phases: A new class of solids; thermodynamically stable nanolaminates,* Progress in Solid State Chemistry **28**, 201 (2000).

[13] M. W. Barsoum and T. El-Raghy, *The MAX phases: Unique new carbide and nitride materials,* American Scientist **89**, 334 (2001).

[14] P. Eklund, M. Beckers, U. Jansson, H. Hogberg, and L. Hultman, *The $M_{n+1}AX_n$ phases: Materials science and thin-film processing,* Thin Solid Films **518**, 1851 (2010).

[15] M. W. Barsoum, *Physical properties of the max phases,* in *Encyclopedia of Materials: Science and Technology (Second Edition)*, edited by K. H. J. B. Editors-in Chief: , W. C. Robert, C. F. Merton, I. Bernard, J. K. Edward, M. Subhash, and V. Patrick (Elsevier, Oxford, 2006) pp. 1–11.

[16] L.-O. Xiao, S.-B. Li, G. Song, and W. G. Sloof, *Synthesis and thermal stability of Cr_2AlC,* Journal of the European Ceramic Society **31**, 1497 (2011).

[17] M. W. Barsoum, T. H. Scabarozi, S. Amini, J. D. Hettinger, and S. E. Lofland, *Electrical and thermal properties of Cr_2GeC,* Journal of the American Ceramic Society **94**, 4123 (2011).

[18] Z. M. Sun, *Progress in research and development on max phases: A family of layered ternary compounds,* International Materials Reviews **56**, 143 (2011).

[19] X. H. Wang and Y. C. Zhou, *Layered machinable and electrically conductive Ti_2AlC and Ti_3AlC_2 ceramics: a review,* Journal of Materials Science & Technology **26**, 385 (2010).

[20] S. Li, G. Song, K. Kwakernaak, S. van der Zwaag, and W. G. Sloof, *Multiple crack healing of a Ti_2AlC ceramic,* Journal of the European Ceramic Society **32**, 1813 (2012).

[21] N. Birks, G. H. Meier, and F. S. Pettit, *Introduction to the High-Temperature Oxidation of Metals*, 2nd ed. (Cambridge University Press, New York, United States of America, 2006).

[22] T. J. Nijdam, L. P. H. Jeurgens, and W. G. Sloof, *Modelling the thermal oxidation of ternary alloys - compositional changes in the alloy and the development of oxide phases,* Acta Materialia **51**, 5295 (2003).

[23] D. E. Hajas, M. to Baben, B. Hallstedt, R. Iskandar, J. Mayer, and J. M. Schneider, *Oxidation of Cr_2AlC coatings in the temperature range of 1230 to 1410°c,* Surface and Coatings Technology **206**, 591 (2011).

[24] S. Gupta, A. Ganguly, D. Filimonov, and M. W. Barsoum, *High-temperature oxidation of Ti_3GeC_2 and $Ti_3Ge_0 \cdot 5Si_0 \cdot 5C_2$ in air,* Journal of The Electrochemical Society **153**, J61 (2006).

[25] B. Anasori, E. N. Caspi, Y. Elraheb, and M. W. Barsoum, *On the oxidation of Ti_2GeC in air,* Journal of Alloys and Compounds **580**, 550 (2013).

[26] C. Wagner, *Reaktionstypen bei der oxydation von legierungen,* Zeitschrift für Elektrochemie, Berichte der Bunsengesellschaft für physikalische Chemie **63**, 772 (1959).

[27] M. W. Barsoum and M. Radovic, *Elastic and mechanical properties of the max phases, Annual Review of Materials Research, Vol 41*, Annual Review of Materials Research Annual Review of Materials Research, **41**, 195 (2011).

[28] T. Liao, J. Wang, M. Li, and Y. Zhou, *First-principles study of oxygen incorporation and migration mechanisms in Ti_2AlC,* Journal of Materials Research **24**, 3190 (2009).

[29] Y. Bai, X. He, Y. Sun, C. Zhu, M. Li, and L. Shi, *Chemical bonding and elastic properties of Ti_3AC_2 phases (A=Si, Ge, and Sn): A first-principle study,* Solid State Sciences **12**, 1220 (2010).

[30] A. Ganguly, M. W. Barsoum, and R. D. Doherty, *Interdiffusion between Ti_3SiC_2–Ti_3GeC_2 and Ti_2AlC–Nb_2AlC diffusion couples,* Journal of the American Ceramic Society **90**, 2200 (2007).

[31] J. Wang, Y. Zhou, T. Liao, J. Zhang, and Z. Lin, *A first-principles investigation of the phase stability of Ti_2AlC with Al vacancies,* Scripta Materialia **58**, 227 (2008).

[32] B. Liu, J. Y. Wang, J. Zhang, J. M. Wang, F. Z. Li, and Y. C. Zhou, *Theoretical investigation of a-element atom diffusion in Ti_2AC (A = Sn, Ga, Cd, In, and Pb),* Applied Physics Letters **94**, 181906 (2009).

[33] M. Beyeler and Y. Adda, *Détermination des volumes d'activation pour la diffusion des atomes dans l'or, le cuivre et l'aluminium,* J. Phys. France **29**, 345 (1968).

[34] D. Mathiot, *Gold, self-, and dopant diffusion in silicon,* Physical Review B **45**, 13345 (1992).

[35] J. D. Meakin and E. Klokholm, *Self-diffusion in tin single crystals,* Transactions of the Metallurgical Society of AIME **218**, 463 (1960).

[36] S. Sarian, *Diffusion of 44Ti in TiC_x,* Journal of Applied Physics **40**, 3515 (1969).

[37] V. S. Eremeev and A. S. Panov, *Diffusion of carbon in vanadium and titanium carbides,* Soviet Powder Metallurgy and Metal Ceramics **6**, 306 (1967).

[38] Y. M. Ovchinnikov, S. V. Karpachev, A. D. Neuimin, and S. F. Pal'guev, *The oxygen permeability of zirconia ceramics,* Refractories **6**, 520 (1966).

[39] C.-J. Wang and C.-Y. Huang, *Effect of TiO_2 addition on the sintering behavior, hardness and fracture toughness of an ultrafine alumina,* Materials Science and Engineering: A **492**, 306 (2008).

[40] B. Cui, D. D. Jayaseelan, and W. E. Lee, *Tem study of the early stages of Ti_2AlC oxidation at 900°c,* Scripta Materialia **67**, 830 (2012).

[41] Y. C. Zhou, H. Y. Dong, and X. H. Wang, *High-temperature oxidation behavior of a polycrystalline Ti_2SnC ceramic,* Oxidation of Metals **61**, 365 (2004).

[42] G. M. Song, V. Schnabel, C. Kwakernaak, S. van der Zwaag, J. M. Schneider, and W. G. Sloof, *High temperature oxidation behaviour of Ti_2AlC ceramic at 1200°c,* Materials at High Temperatures **29**, 205 (2012).

[43] D. J. Tallman, B. Anasori, and M. W. Barsoum, *A critical review of the oxidation of Ti_2AlC, Ti_3AlC_2 and Cr_2AlC in air,* Materials Research Letters **1**, 115 (2013).

[44] D. B. Lee, T. D. Nguyen, and S. W. Park, *Long-time oxidation of Cr_2AlC between 700 and 1,000 °c in air,* Oxidation of Metals **77**, 275 (2012).

[45] J. C. Rao, Y. T. Pei, H. J. Yang, G. M. Song, S. B. Li, and J. T. M. De Hosson, *Tem study of the initial oxide scales of Ti_2AlC,* Acta Materialia **59**, 5216 (2011).

[46] J. M. Howe, *Bonding, structure and properties of metal/ceramic interfaces,* MRS Online Proceedings Library **314**, null (1993).

[47] L. Vitos, A. V. Ruban, H. L. Skriver, and J. Kollar, *The surface energy of metals,* Surface Science **411**, 186 (1998).

[48] F. R. de Boer, R. Boom, W. M. Mattens, A. R. Miedema, and A. K. Niessen, *Cohesion in Metals: Transition Metal Alloys. Vol. 1*, Vol. 1 (North-Holland Physics Publishing Elsevier Science Publishers B.V., Amsterdam, the Netherlands, 1989).

[49] I. J. Bennett, J. M. Kranenburg, and W. G. Sloof, *Modeling the influence of reactive elements on the work of adhesion between oxides and metal alloys,* Journal of the American Ceramic Society **88**, 2209 (2005).

3

Determination of fracture strength and fracture energy of (metallo-) ceramics by a wedge loading methodology and corresponding cohesive zone-based finite element analysis

You make experiments and I make theories. Do you know the difference? A theory is something nobody believes, except the person who made it. An experiment is something everybody believes, except the person who made it.

Albert Einstein

This chapter has been submitted to Engineering Fracture Mechanics. Authors: Ann-Sophie Farle,Jayaprakash Krishnasamy, Sergio Turteltaub, Cees Kwakernaak, Sybrand van der Zwaag, Willem G. Sloof

A wedge loaded testing methodology to determine the fracture strength and energy of (semi-) brittle (metallo-)ceramics is presented. The methodology combines a tailored specimen geometry and a comprehensive finite element analysis based on cohesive zone modeling. The use of a simulation-based approach to extract both fracture strength and energy from experimental data avoids the inherent inaccuracies found in closed-form expressions that rely on a priori assumptions about the deformation field. Results from wedge splitting tests on Ti_3SiC_2 and Ti_2AlC (MAX phase) materials are used to illustrate the procedure. The simulation-based approach is further validated by comparing the fracture strength and fracture energies predicted by the proposed method and those indicated by a conventional four-point bending fracture toughness test (ASTM standard). The new protocol offers the possibility to measure not only the fracture properties of brittle material in its pristine state but also in the healed state.

3.1. Introduction

Testing procedures to accurately quantify the fracture strength and fracture energy of materials typically depend on a variety of factors such as the material's elastic characteristics (compliant or stiff) and its fracture response (ductile or brittle). The absolute values may also depend on loading rates, the measured primary response variables such as loads and displacements and the post-processing of the recorded data. Ease of sample preparation, insensitivity to non-defined parameters and repeatability of the results also plays a significant role in the design of a testing procedure.

For brittle materials, it is also known that the measured fracture properties depend on the ratio between the size of the critical flaw(s) and the zone where the stress concentrates in the sample (e.g., the measured fracture strength in a tensile test would typically be different from that in a bending test). Bending tests have been accepted as the simplest yet least precise test method to determine fracture strength and fracture energy of brittle materials [1, 2]. Bending tests commonly require controlled pre-cracks, which are difficult to produce and measure in most (semi-) brittle materials [2, 3]. Moreover, this test, assuming a machining induced pre-crack in the material, may overestimate the fracture toughness and is highly sensitive to machining induced surface imperfections [3]. The sensitivity to surface flaws furthermore creates the necessity for higher sampling sizes to compensate for measurement error. In addition to the aforementioned difficulties, the quantification of crack-healing efficiency in self-healing materials requires methods to create stable cracks. Chevron-notched specimens can negate problems caused by pre-cracking attempts so in this sense this sample geometry is generally viewed as an improvement compared to samples without chevrons [2]. Furthermore, when setting the requirements for an optimally informative test method, it is clear that an ideal test should not only report the load-displacement data but also the actual crack length at every stage of the cracking process. For the determination of the crack length both optical [4] and acoustical methods [5] are available while in specific cases also X-ray tomographic methods [6] can be used.

Aside from the physical testing requirements defined above, an important aspect of a testing methodology is the interpretation of the measured data. The quantities of interest, fracture strength and fracture (propagation) energy, are typically not measured directly but rather need to be derived from the measured response variables such as loads and actual crack dimensions. For fracture properties, the traditional approach has relied on using the theory of Linear Elastic Fracture Mechanics (LEFM), which, often in combination with analytical solutions for simple geometries or finite element simulations (FEM) for complex geometries, is used to derive closed-form expressions from which the fracture strength and/or the fracture toughness can be computed (i.e., a critical value of the stress intensity fracture at which a crack propagates) [7, 8]. An alternative approach is to conduct finite element (FEM) numerical simulations of the fracture test using a Cohesive Zone Modelling (CZM) approach. In combination with the experimental data, the simulations can be used to extract the fracture properties of the material taking into account the whole fracture process, namely nucleation and propagation of a crack. CZM combines ingredients found in stress-based and energy-based formulations for fracture mechanics. CZM has been implemented in conjunction with cohesive elements and, more recently, within the so-called eXtended Finite Element Method (XFEM). This

methodology overcomes some intrinsic limitations of the (traditional) LEFM approach since it can model both nucleation and propagation of cracks. CZM, with either cohesive elements or XFEM, has been applied, for example, in [9] to predict the fracture behavior of adhesive joints, in [10] for the analysis of delamination in fiber-reinforced polymer (FRP) beams, in [11] to simulate the crack propagation in wood, in [12] to predict the fatigue crack nucleation and propagation in quasi-brittle materials, in [13] to estimate the fracture toughness of free standing 8 wt. % Y_2O_3–ZrO_2 (8YSZ) coatings and in [14] to analyze a specimen geometry to enhance crack stability for brittle materials and to improve closed-form formulas by deriving the so-called geometrical factor for different specimen dimensions. Other relevant work includes [15], where simulations were conducted to predict the fracture properties of asphalt using a semi-circular bend test (SCB), and [16] where simulations were used to demonstrate the variability and anisotropy of fracture toughness of cortical bone tissue using the load-displacement curve obtained from the three-point bending tests.

While the accurate determination of the fracture properties of pristine (brittle) materials is demanding as it is, with the recent development of self-healing ceramic materials, a new requirement also has to be taken into account, namely that the sample is not split into separate pieces in the determination of the fracture strength and the fracture energy. Only if the crack is contained within the sample, the sample can be exposed to a simple (thermal) healing treatment not requiring uncontrolled manual realignment and clamping of the two fracture surfaces. The test set-up as described here, meets this important requirement.

So the aim of the work is to develop a fracture test method and data analysis protocol to determine both the fracture strength and the fracture toughness of a pristine brittle material in such a manner that after initial fracture testing the sample is in a state suitable for subsequent thermal healing and determination of the fracture properties of the healed sample. The current approach is demonstrated for two semi-brittle MAX phase ceramics, which not only have attractive mechanical properties at ambient and high temperatures [17] but also recover their mechanical strength upon high temperature annealing [6, 13, 18]. In the present analysis we only focus on the determination of the fracture properties in the pristine state. The determination of the fracture properties of these materials in a healed state is subject of a separate publication.

3.2. Experimental and Modelling

3.2.1. Specimen Design

The new chevron-notched, wedge-loaded specimen geometry (WLS) is shown in Figure 3.1. The basal half-length HW is chosen as 0.48W, where W is the longest height of the sample. A curvature with a radius of 52° as the base allows sample self-alignment under loading conditions. A chevron notch tip is located at a depth of 10 mm. The contact edges of the notch opening are rounded with a radius of 1 mm to minimize the friction with the loading-wedge.

A 90° guide-groove is machined into the side of the sample to reduce the thickness by half (BN/B=0.5). The recommended thickness of B=5 mm is within the limits set by the ASTM E647 standard for compact tension specimen [19]. In this study, samples with

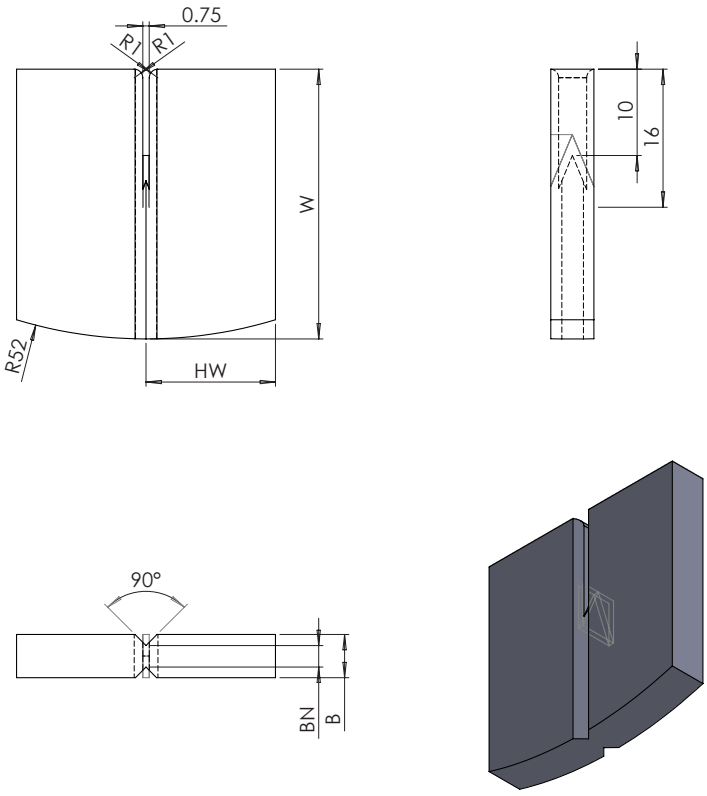

Figure 3.1: Wedge splitting test specimen geometry with lengths in mm.

a basal half-length HW of 12 mm, a height W of 25 mm and thickness B=5 mm were used.

3.2.2. Samples and Test Setup

Samples of Ti_2AlC and Ti_3SiC_2 were synthesised by reactive sintering in a spark plasma sintering (SPS) furnace (HP D 25 SD, FCT Systeme GmbH, Germany). Ti_3SiC_2 starting powders of Ti (100 µm, >99.5%, TLS Technik GmbH & Co., Germany), Si (45 µm, > 99.99 %, TLS Technik GmbH & Co., Germany) and TiC (< 10 µm, 99%, ChemPur, Germany) were mixed for 4 hours using a Turbula T2C Mixer (Willy A. Bachofer, Switzerland) with 5 mm alumina balls. Powder mixtures with molar ratios of Ti : Si : TiC with Ti and Si as 1 and varying TiC , viz.: 1.4 and 1.5, were sintered at 1500 °C for 4 h in 40 mm graphite moulds under a uniaxial pressure of 50 MPa. Similarly, Ti_2AlC was sintered from Ti, Al (45 µm, > 99.99%, TLS Technik GmbH & Co., Germany) and graphite (6 µm, > 99.5, Graphit Kropfmühl AG, Germany) in a ratio of 0.85 : 1.05 : 1.15 at 1400 °C for 30 min. The phase purity of the samples was determined via X-ray diffraction using a Bruker D8 ADVANCE diffractometer (Bruker, Germany) in the Bragg-Brentano geometry with a graphite monochromator and Co Kα radiation. The recorded X-ray diffractrograms were processed with Bruker software DIFFRAC.EVA 4.1 software. Elastic properties were determined by Vickers indentation using a hardness tester (Zwick/Z2.5, Germany). Indents were created by loading the indenter with 5 N s^{-1} up to 50 N, holding for 12 s and unloading with 3.7 N s^{-1}. The density of the material was measured with the Archimedes method using an analytical balance (Mettler Toledo AG-204, Switzerland) according to ASTM B 962 [20]. All Ti_2AlC and Ti_3SiC_2 samples were more than 92% dense.

All machining was carried out by electric discharge machining (EDM) with wire diameters of 0.25 and 0.1 mm.

The test setup is shown schematically in Figure 3.2. Tests were performed using a 100 kN electro-mechanical load frame (Series 5500R, Instron, USA) that was fitted with a 10 kN load cell to suit the recorded load levels. The sample was placed on a flat stainless steel base-plate without further clamping. The quenched and tempered steel 10° wedge was lowered into the sample groove until it reached a pre-load of approximately 10 N.

Tests were carried out under closed-loop displacement control, with a fixed crosshead displacement rate of 0.01 or 0.1 mm s^{-1}. Crosshead displacement signal was calibrated by compression tests with strain gauge control to correct for rig deformation under the applied loads. The crosshead motion was stopped when a load drop of 50 % from peak load was recorded. Upon termination, the crosshead motion was reversed leading to retraction of the wedge. Unloading curves were not recorded.

The recording of the acoustic events during the fracturing was performed with a Physical Acoustics module (PCI-2, 2 channel 40 MHz 18 bit data-acquisition combined with ILS40 pre-amplifiers). Registration and post-processing were executed with the Physical Acoustics AEWin 1.70 (2005) software module. Prior to testing, two microphones were attached with paraffin wax to the right and left of the sample groove to allow registration of acoustic emission signals during the experiments. The sampling rate employed was 2 MHz with a 20 dB amplification factor. An acoustic event was recorded if the signal level of any microphone exceeded 5 mV. Every event was separately recorded as a waveform file containing 2048 points at 0.5 µs intervals. The energies recorded varied in a wide range between 1 aJ to 1 nJ. A cumulative energy as a function of time,

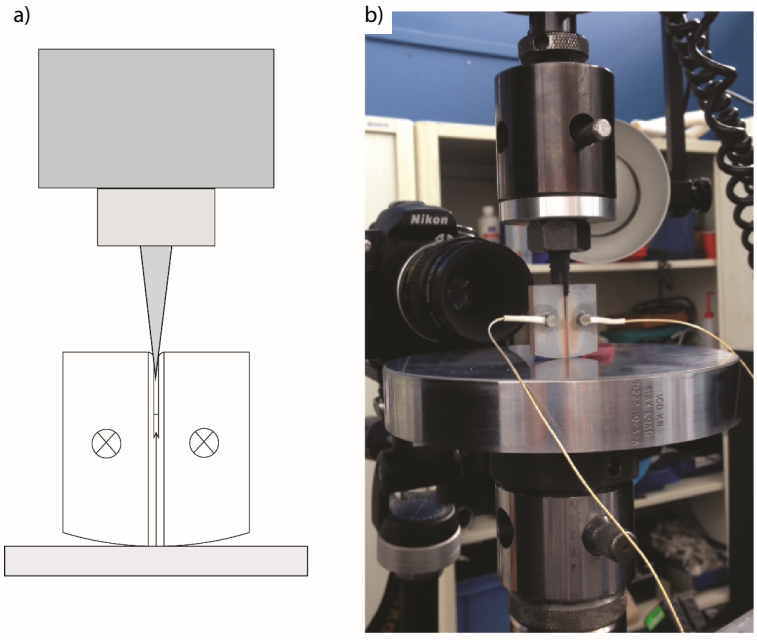

Figure 3.2: Test setup of chevron-notched, wedge-loaded specimen (WLS) with microphone positions indicated (a) schematic and (b) actual test setup.

termed the “acoustic energy”, was obtained through post-processing of the acoustic events. Final crack lengths and microstructure were determined by optical microscopy using a digital microscope (Keyence VHX-100, Osaka, Japan) and scanning electron microscopy (SEM), type JSM 6500F (JEOL Ltd., Tokyo, Japan) equipped with an energy dispersive spectrometer (EDS, type: ThermoFisher UltraDry 30 mm^2 detector) for X-ray microanalysis (XMA) and with Noran System Seven software package for data acquisition and analysis. Surfaces and cross-sections, prepared by cutting with a diamond wafering blade, were ground using SiC paper up to 4000 grit and polished with diamond suspension up to 1 µm.

3.2.3. FEM with cohesive zone modeling

The extraction of fracture material properties is based on simulating the actual experimental set up using a Finite Element approach with cohesive zone modelling. The finite element model of the chevron-notched, wedge-loaded specimen (WLS) test set up is shown in Figure 3.3. For computational efficiency, the specimen is modelled as a two-dimensional domain under plane stress assumption. To simulate the three-dimensional features of the specimen, the chevron notch and the groove in the specimen geometry are modelled using a variable thickness. The fracture process is simulated using cohesive elements that are inserted at the interfaces of all bulk elements in the regions where crack(s) are expected to initiate and propagate, in particular at the chevron and groove. A bilinear traction-separation relation is used to describe the local nucleation and crack-

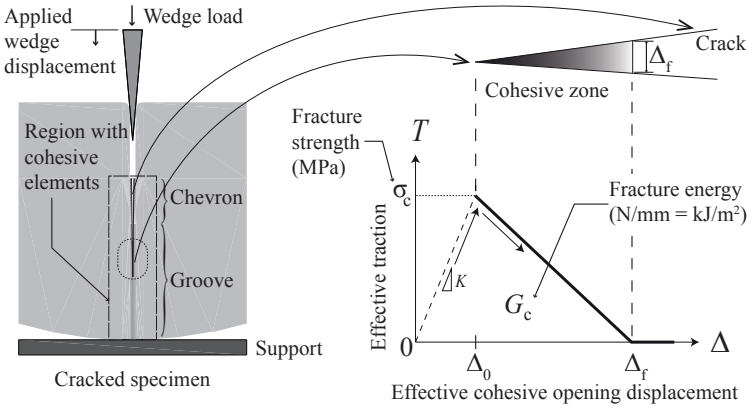

Figure 3.3: Numerical model of wedge splitting test specimen with a bilinear cohesive relation implemented in cohesive elements to simulate the fracture process during testing. The area under the curve corresponds to the fracture energy per unit area required to fully separate the cohesive surface.

opening process within the numerical sample as shown in Figure 3.3. The critical traction corresponds the maximum effective traction value that can be transmitted through the cohesive surface (fracture strength) and the area under the curve corresponds to the fracture energy required to fully separate the cohesive surface at a given location (i.e., per unit newly cracked area). The initial response of the cohesive surface before fracture is characterized by a cohesive stiffness whose value is chosen as large as possible to avoid artificial compliance but still preventing a (numerically) singular response. After reaching the fracture strength, the progressive degradation of the load-carrying capacity of the cohesive zone is captured by a linear softening relation until the load is zero, which is interpreted as a fully-formed crack where no load can be transmitted for subsequent increases in the cohesive opening displacement. The effective cohesive opening displacement and the effective traction combine contributions from components that are normal and tangential to the cohesive surface. The cohesive relation is applicable for pure mode I (normal), pure mode II (tangential) or mixed-mode openings depending on the deformation at a given location (see, e.g., [21, 22] for details).

A fine mesh is used in the region of interest (groove and chevron) and a coarser mesh is used in other regions. The mesh in the region of interest is chosen in accordance to the cohesive zone length l_{fpz}, which is defined here as

$$l_{fpz} = \frac{EG_c}{\sigma_c^2} \tag{3.1}$$

where E is taken as the Young's modulus of the material. The characteristic element size is chosen such that the cohesive zone can be accurately resolved, i.e., the cohesive zone spreads among several cohesive elements. The boundary conditions in the simulations are chosen such that they closely reproduce the testing conditions. The displacement of the top of the wedge is prescribed as a function of time according to the loading rate whereas the bottom of the support plate is modeled as simply-supported.

Table 3.1: Specimen properties used in the model

Specimen	E_s	ν_s
Ti_3SiC_2	320 GPa	0.2
Ti_2AlC	260 GPa	0.18

The wedge and the support are included in the simulation as deformable parts. Contact friction between the wedge and the specimen is modeled using Coulomb's model with a coefficient of kinematic friction. The elastic responses of the wedge and the specimen are modeled using isotropic and linear relations with Young's modulus and Poisson's ratio taken as E_w=200 GPa, ν_w=0.3 and, for the specimens, as specified in Table 3.1.
where the subscript refers to the wedge (w) or specimen (s). The elastic properties of the specimens are obtained from published data [23–25] and verified with indentation tests whereas the wedge properties are taken from the wedge material's specification. The support is modeled as an elastic material that approximates a rigid body with frictionless contact used at the interface of the support and the specimen. Preliminary simulations including plasticity in both the specimen and the wedge were carried out to determine its likelihood of occurrence and its possible effect on the results. It was concluded that plastic behavior is confined to a small region close to the cracks and its effect cannot be separated from the cohesive relation (i.e., at the length scale of the simulation, it is possible to model the bulk response of the material as elastic and use a cohesive relation to capture the inelastic behavior).

Since the purpose of the simulations is to determine the fracture properties of the specimen, a parametric analysis was carried out varying the effective fracture strength and the effective fracture energy G_c . In addition, it is known that for a wedge-splitting test, friction can play a significant role [3]. Consequently, distinct values of the (kinematic) friction coefficient f used in Coulomb's model were considered.

3.2.4. Simulation Setup

To simulate the test, a downward displacement of the top of the wedge is specified. Upon contact with the specimen, the specimen undergoes a loading dominated by an opening mode (mode I), although the actual loads at the crack tip are obtained from the simulation. The corresponding reaction force at the top of the wedge, which is obtained as a result of the simulation, is recorded throughout the simulation.

The procedure to extract the fracture material properties is as follows:

1. A preliminary elastic simulation is carried out for different values of the coefficient of friction. The value of f for which the *initial slope* of the simulation coincides with the initial slope of the experimental data to within a desired tolerance is then used for subsequent steps. If the experimental and the simulation responses deviate from a linear curve, then it is recommended to match the average slope until the onset of cracking as measured from the acoustic emission.

2. With a chosen (fixed) coefficient of friction, a parametric analysis including fracture is carried out for different values of the fracture strength and fracture energy.

3. For each pair of values of fracture strength and energy, the wedge load is obtained as a function of the wedge displacement. This prediction is compared with the experimental response. The actual fracture material properties are taken as those for which the simulation provides the best approximation to the experimental data. In accordance with the CZM approach, the best fit is obtained by comparing the predicted and the experimentally-obtained maximum load and total energy dissipated. For an independent verification, the crack length predicted in the simulation is also recorded as a function of the wedge displacement and compared with the experimental data.

3.3. Results and Discussion

3.3.1. Experimental Results

XRD analysis of the Ti_3SiC_2 samples revealed only minor amounts of TiC as a second phase in all samples. The variance in precursor ratios had no effect on the final composition. According to XRD results spark plasma sintering of elemental powders resulted in pure Ti_2AlC samples. Ti_3SiC_2 samples consists of slightly elongated grains with a length between 20 and 80 µm. Ti_2AlC specimen have a similar morphology with grains of 50 µm (± 20 µm) maximum length and a width of max. 25 µm.

The measured wedge load as a function of the wedge displacement for the samples tested is shown in Figure 3.4a for Ti_3SiC_2 and in Figure 3.4b for Ti_2AlC.

Figure 3.4 also shows the measured crack length and cumulative acoustic signal as a function of the wedge displacement for one representative Ti_3SiC_2 sample and one Ti_2AlC sample. The crack growth curve for the Ti_3SiC_2 sample shows a slow and controlled crack propagation. For the Ti_2AlC sample, the crack growth is mostly controlled except during the transition from the chevron to the groove where the crack length increased abruptly. However, subsequent crack growth in the groove proceeded in a controlled fashion. Based on preliminary tests where the loading was interrupted at fixed intervals and the crack length was optically measured (not reported here for conciseness), a reasonably good correlation is found between crack propagation and acoustic energy, which indicates that this parameter can be used to estimate crack length. The experimental results shown in Figures 3.4 were conducted continuously so the acoustic energy was normalized using only the crack length at the end of the experiment, which was measured by optical and scanning electron microscopy. The final crack length recorded for the Ti_3SiC_2 sample was 9.6 mm and for Ti_2AlC sample was 11.36 mm, measured from the tip of the chevron notch.

According to the acoustic data shown in Figure 3.4, crack formation in the chevron occurred before the peak load was reached. Crack development in the chevron notch starts in the early stages of testing, at relatively low load levels. For Ti_3SiC_2 samples, as shown in Figure 3.4a, the peak load appears to occur before the crack front moves from the chevron to the uniform groove. For Ti_2AlC samples this transition apparently occurs during a fast propagation stage, so it is not possible to uniquely correlate the peak load and a specific crack length, but the data suggests that the peak load was also reached before the crack front moves from the chevron to the uniform groove. This observation is relevant since some formulas published in the literature assume that the peak load

coincides with an a-priori known crack length, which is not the case in the present study according to the acoustic measurements. Simulation results support this conclusion, see below.

As shown in Figure 3.4a, the load displacement curves of the individual Ti_3SiC_2 samples are relatively close to each other, reaching a peak load at approximately the same wedge displacement. The average peak load for Ti_3SiC_2 is approximately 180 N. In contrast, the Ti_2AlC samples showed more variability as observed in Figure 3.4b. The peak load was reached at distinct values of the wedge displacement. Consequently, the average peak load for Ti_2AlC, which is approximately 210 N, does not exactly coincide with the peak load of the average response, which is slightly lower as shown in Figure 3.4b. Nonetheless, the average response is used for comparison purposes with the simulation results as detailed in the next section.

3.3.2. Fracture Properties

In accordance with the procedure outlined in Section 3.2, the first step is to determine the coefficient of friction between the wedge and the sample. The wedge load as a function of the wedge displacement for distinct possible values of the coefficient of friction is shown in Figure 3.5a for the Ti_3SiC_2 samples and in Figure 3.5b for the Ti_2AlC samples. The simulations also include the fracture behavior for reference purposes, although only the initial elastic response is required to determine the value of . For the values considered, the best match for the (average) initial response is attained with a coefficient of friction for the Ti_3SiC_2 samples and for the Ti_2AlC samples, which are within the range of published values [26].

With the chosen coefficients of friction, simulations were conducted for distinct values of the fracture strength and the fracture energy. The wedge force as a function of the wedge displacement is shown in Figure 3.6 for a fixed value of the fracture energy and various values of the fracture strength of the Ti_3SiC_2 and Ti_2AlC samples. Similarly, Figure 3.7 indicates the load-displacement response for a fixed value of the fracture strength and various values of the fracture energy.

Table 3.2: Fracture strength and fracture energy of Ti_2AlC and Ti_3SiC_2 as determined in the simulations

Material	Fracture strength σ_c	Fracture energy G_c
Ti_3SiC_2	180 MPa	$0.725\,\mathrm{N\,mm^{-1}}$
Ti_2AlC	175 MPa	$1.2\,\mathrm{N\,mm^{-1}}$

From Figure 3.6 it can be observed that, as anticipated, the fracture strength mostly affects the peak load, but the rest of the curve is somewhat similar for a fixed value of the fracture energy. In contrast, as shown in Figure 3.7, both the peak load and the energy dissipated in the process increase with increasing fracture energy for a fixed fracture strength. A comparative analysis of the results shown in Figures 3.6 and 3.7 indicate that the peak load depends both on the fracture strength and the fracture energy. The fracture strength controls the early stage (nucleation) of cracks in the chevron while the fracture energy controls its subsequent propagation throughout the chevron and the groove. From the set of values considered in the simulations, the best fit for the average response of the Ti_3SiC_2 and Ti_2AlC samples are found in Table 3.2.

(a)

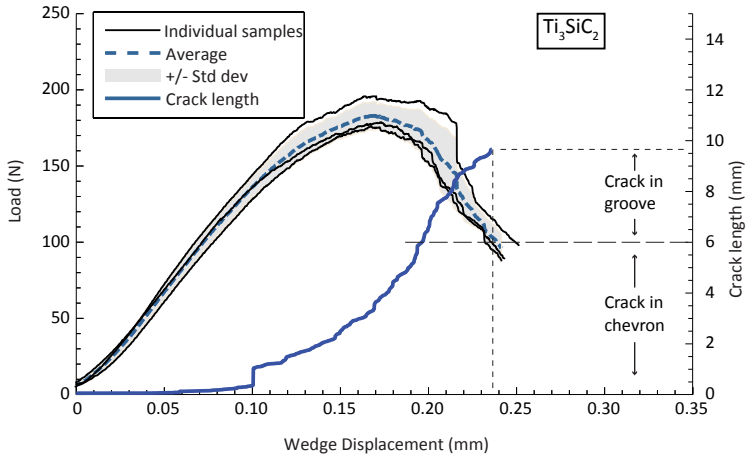

(b)

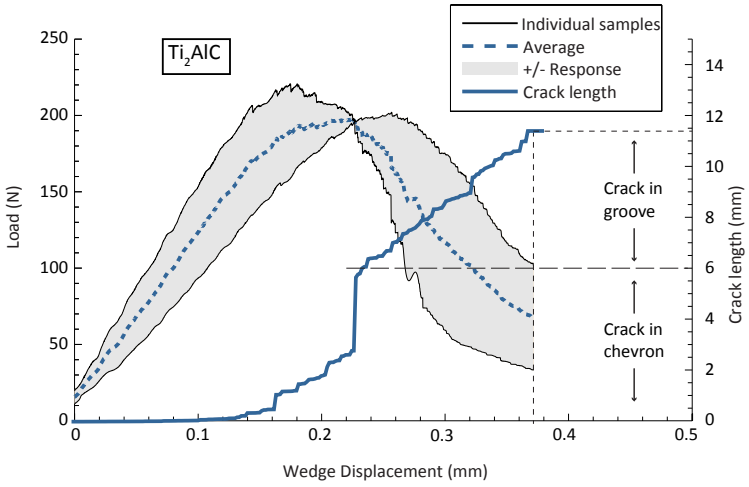

Figure 3.4: Wedge load (left axis) and normalized crack length (right axis) versus wedge displacement for Ti_3SiC_2 and Ti_2AlC samples. The dashed blue line represents the average between the samples. The crack length is deduced from the acoustic energy and it is normalized using a directly measured crack length, namely (a) 9.6 mm for Ti_3SiC_2 adnd (b) 11.36 mm for Ti_2AlC, at the end of the test.

(a)

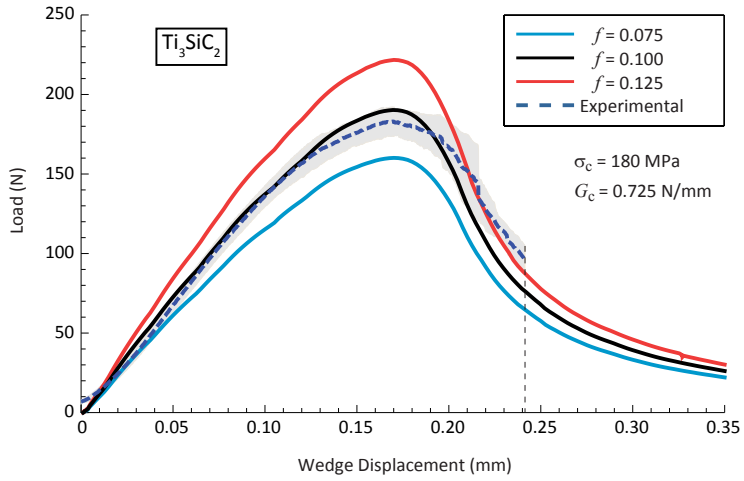

(b)

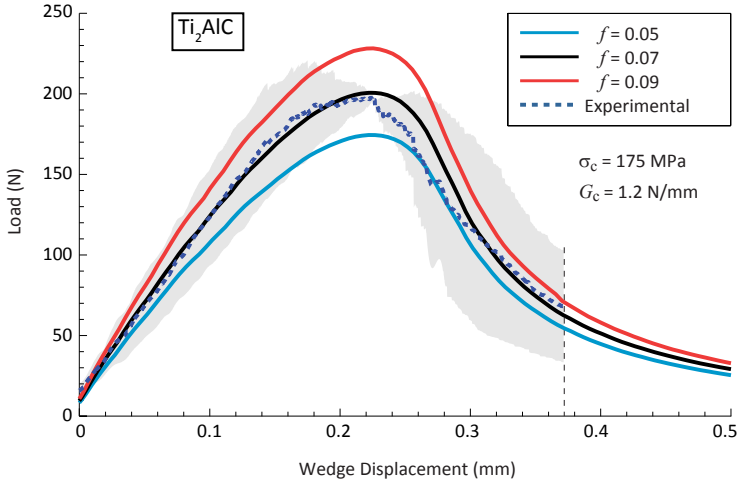

Figure 3.5: Wedge load as a function of wedge displacement for three distinct values of the coefficient of friction between the wedge and the Ti_3SiC_2 and Ti_2AlC specimens. In accordance with the geometry shown in Figure 3.3, higher coefficients of friction effectively provide stiffer initial responses.

(a)

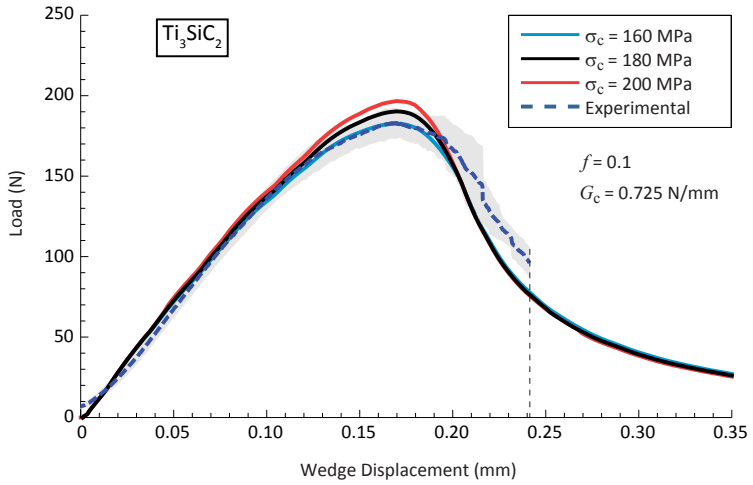

(b)

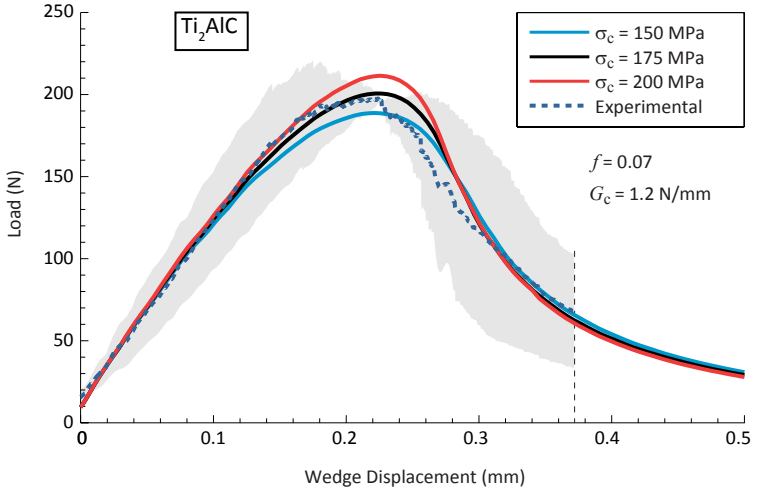

Figure 3.6: Wedge load as a function of wedge displacement for three distinct values of the fracture strength and for a fixed fracture energy of 0.725 N mm^{-1} for the Ti_3SiC_2 specimens and 1.2 N mm^{-1} for the Ti_2AlC specimens. Within the range of values analyzed for (a) Ti_3SiC_2 (160 MPa to 200 MPa) and (b) Ti_2AlC (150 MPa to 200 MPa), the difference in response is mainly reflected in the peak load.

(a)

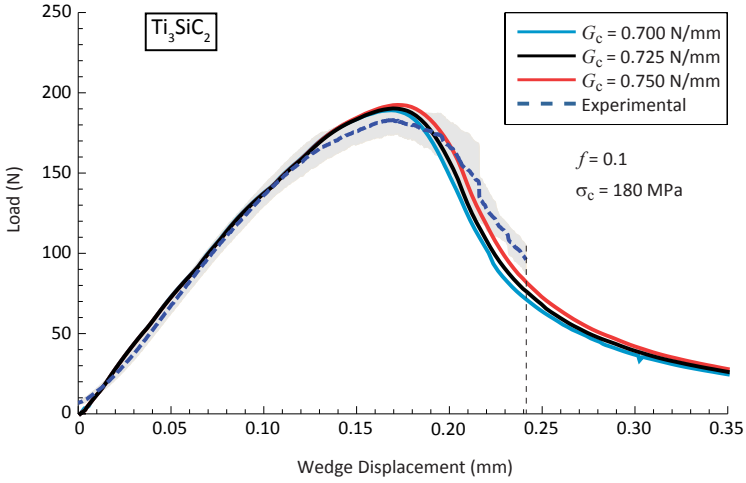

(b)

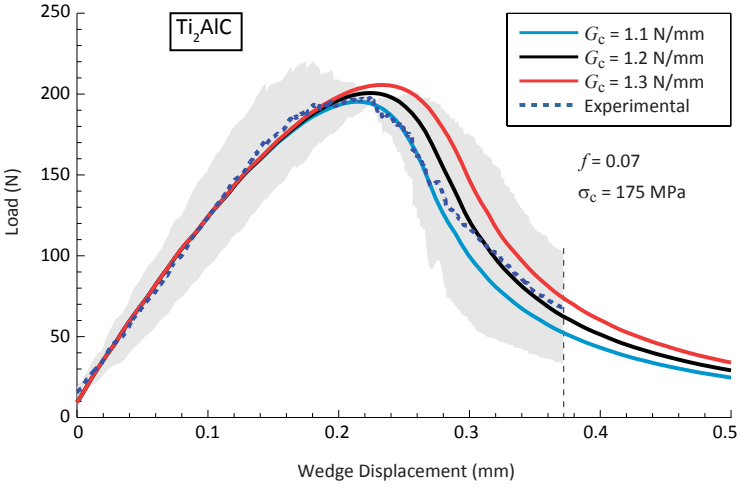

Figure 3.7: Wedge load as a function of wedge displacement for three distinct values of the fracture energy and for a fixed fracture strength of 180 MPa for the Ti_3SiC_2 specimens and 175 MPa for the Ti_2AlC specimen. As expected, the effective energy dissipated (measured as the area under the curves) increases for increasing values of the fracture energy. The best fit in terms of energy as well as the peak load is obtained with (a) a fracture strength of 180 MPa and a fracture energy of 0.725 $N\,mm^{-1}$ for Ti_3SiC_2 and (b) a fracture strength of 175 MPa and a fracture energy of 1.2 $N\,mm^{-1}$ for Ti_2AlC.

To verify the capacity of the simulations to reproduce the experimental results, the predicted and measured crack length as a function of wedge displacement are shown in Figure 3.8 for the same values used in the results shown in Figure 3.6 (i.e., variable strength) and in Figure 3.9 for the same values used in the results shown in Figure 3.7 (i.e., variable fracture energy).

The simulation results shown in Figures 3.8 and 3.9 indicate that the crack nucleates in the chevron and initially grows linearly as a function of wedge displacement. As the crack front approaches the transition region from the chevron to the groove (see Figures 3.1, 3.2 and 3.3), the rate of growth increases. Subsequently, the growth rate decreases as the crack front further advances into the uniform groove. For the Ti_3SiC_2 samples, as shown in Figures 3.8a and 3.9a, it can be observed that the simulations are in good agreement with the evolution of the crack length as deduced from the acoustic signal. For the Ti_2AlC samples, as shown in Figures 3.8b and 3.9b, the simulations initially over-predict the crack length (as deduced from the acoustic signal) but, after a sudden crack propagation, the experimental and simulated evolutions approximately coincide.

Comparing Figures 3.8a and 3.9a for the Ti_3SiC_2 samples and Figures 3.8b and 3.9b for the Ti_2AlC samples, it can be observed that for both materials the initial crack length is more sensitive to variations in fracture strength and, conversely, the final crack length is more sensitive to variations in fracture energy.

Using the best fit fracture parameters, it can be seen that the instant when the crack front moves from the chevron to the uniform groove corresponds to a wedge displacement of 0.2 mm for the Ti_3SiC_2 samples and 0.25 mm for the Ti_2AlC samples (see Figure 3.8). Using these values in the horizontal axis in Figure 3.6 it can be seen that the simulation predicts that the peak load occurs when the crack is still in the chevron (this effect is more pronounced for the Ti_3SiC_2 sample than for the Ti_2AlC sample).

For the range of fracture strength analyzed, the simulations predict a similar total crack length at the end of the loading, which matches relatively well the experimental value. This finding suggests that crack length may be used to estimate the fracture properties, but it may not be sufficiently sensitive to differentiate between distinct values. Differentiation between response curves are amplified as the crack front moves from the chevron to the groove, but the inherent uncertainty of acoustic-based crack length measurement suggests that it is better to extract material properties from the load-displacement curve as indicated above.

3.4. Comparison of simulation-based approach with a standardized procedure: four-point bending test with chevron-notched specimen.

The methodology described in the present work involves two novel aspects compared to existing (standardized) tests, namely the geometry of the specimen and the simulation-based approach to extract material properties. To cross-validate the simulation-based approach, the method was also applied to a standardized geometry for determining fracture toughness in brittle materials. To this end, a ASTM four-point bending test with a chevron-notched specimen was used as benchmark (Standard C1421-16 [2]). The comparison is done at the level of the post-processing of the data by comparing the

(a)

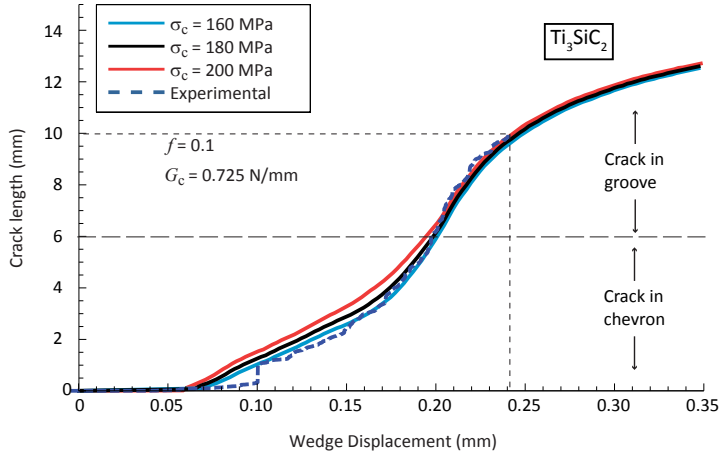

(b)

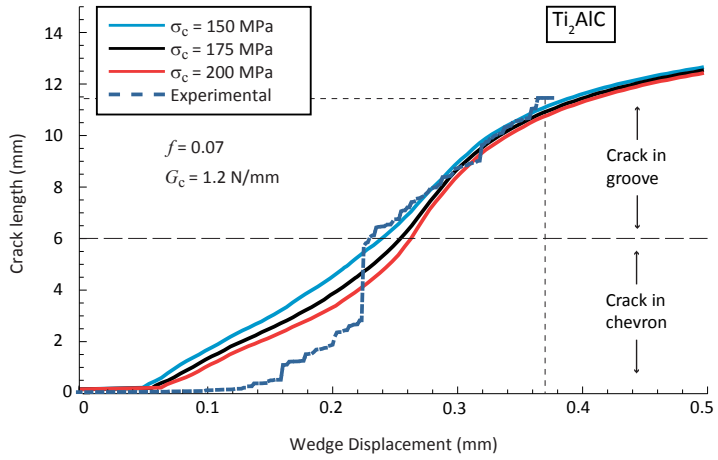

Figure 3.8: Crack length as a function of wedge displacement for three distinct values of the fracture strength and for a fixed fracture energy of 0.725 N mm^{-1} for the Ti_3SiC_2 and Ti_2AlC samples.

(a)

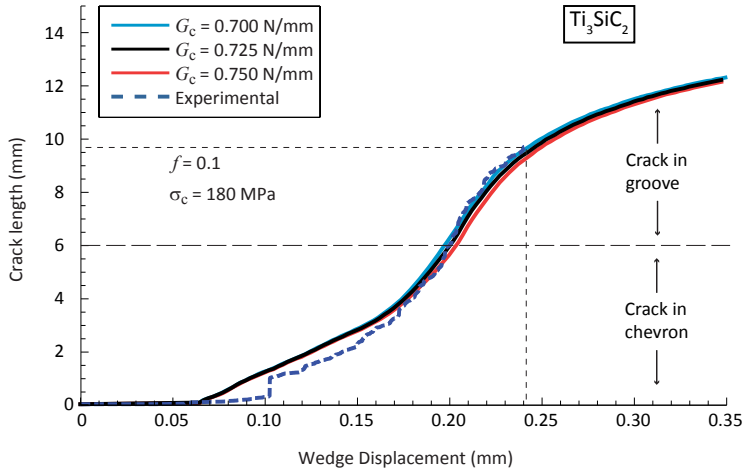

(b)

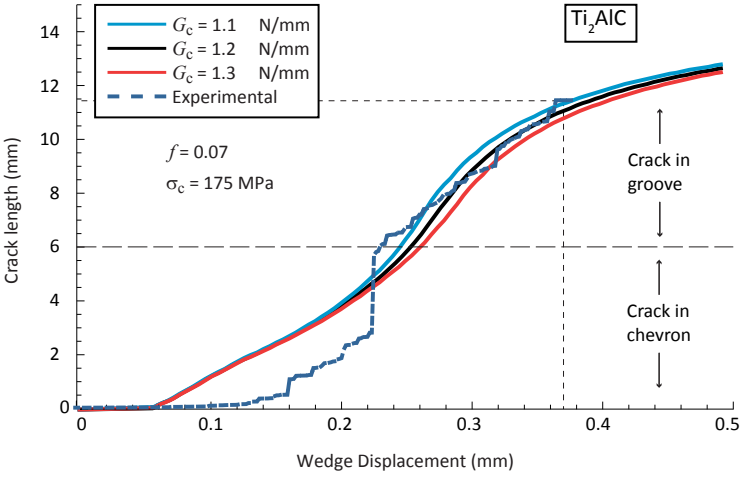

Figure 3.9: Crack length as a function of wedge displacement for three distinct values of the fracture energy and for a fixed fracture strength of 180 MPa for the Ti_3SiC_2 samples and 175 MPa for the Ti_2AlC samples. The initial crack growth, starting around a wedge displacement of 0.07 mm in the simulations, occurs in the chevron. The crack growth rate as a function of the wedge displacement is initially approximately linear. The subsequent change in slope corresponds to the transition from the chevron to the groove, which approximately coincides with the peak load.

simulation-based procedure and a standardized closed-form expression to extract fracture properties. Since the standardized four-point bending test is designed to extract the critical value of the stress intensity factor under nominal mode I conditions, it is necessary to relate this material property to the fracture energy. Assuming plane stress conditions and a small plastic zone, then the fracture energy can be related to the toughness as

$$G_C = \frac{K_{IC}^2}{E_S} \tag{3.2}$$

where E_S is the Young's modulus of the specimen. For a given geometry of the chevron-notched specimen used in the four-point bending test, the ASTM standard provides a formula that uses the peak load recorded in the experiment to compute the critical stress intensity factor [2]. The ASTM model is plotted as a solid line in Figure 3.10. For the numerical simulations based on the cohesive zone, the procedure is as follows:the fracture properties are given (fracture strength and fracture energy) and the test is simulated. The fracture energy is computed from the critical stress intensity factor and given elastic properties (in this case with a Young's modulus of 280 GPa) while representative values of the fracture strength are chosen. The outcome of the simulation is the peak load, which is indicated in Figure 3.10 (discrete data points) for five values of the fracture strength, ranging from 100 MPa to 500 MPa. For each value of the fracture strength, a fitted curve is indicated to better visualize the predictions of the simulations. From Figure 3.10 it can be observed that if the material is sufficiently brittle (i.e., relatively low fracture energy to strength ratio), the ASTM formula and the cohesive-zone simulation-based results provide comparable predictions, albeit for a limited range of fracture strengths. However, for higher values of the fracture energy, typically found in semi-brittle materials, the simulations predict a higher peak load. Note that this is only a qualitative comparison as it is not possible to ascribe a better accuracy to either procedure without access to a third reference approach deemed more precise. However, it can be concluded that for brittle materials (as intended in the ASTM analysis), the two procedures are somewhat similar while for semi-brittle and more ductile materials, the two methodologies provide different results.

The chevron-notched, four-point bending test (ASTM E399 [27]) was applied to five samples of Ti_3SiC_2 and five samples of Ti_2AlC from the same batches as the ones used in the wedge splitting test. The samples were machined from the bulk specimen by spark erosion and ground to a surface finish of 3 µm polish. However, it was not possible to achieve stable crack propagation in any sample even for relatively low loading rates. The ASTM standard considers a test to be valid only if stable crack growth can be achieved, hence these (invalid) tests are not reported in detail here. However, it is interesting to mention that the peak loads recorded would have predicted a significantly lower fracture energy compared to the values obtained from the wedge splitting test. It is also relevant to mention that the peak loads for the Ti_3SiC_2 samples were consistently lower than those of the Ti_2AlC samples, yet showing a similar relative ranking as the wedge splitting test (i.e., Ti_2AlC samples are tougher than the Ti_3SiC_2 samples). The most important observation, however, is that the wedge-splitting test allowed for a controlled crack growth whereas this was not possible to achieve with the four-point bending test.

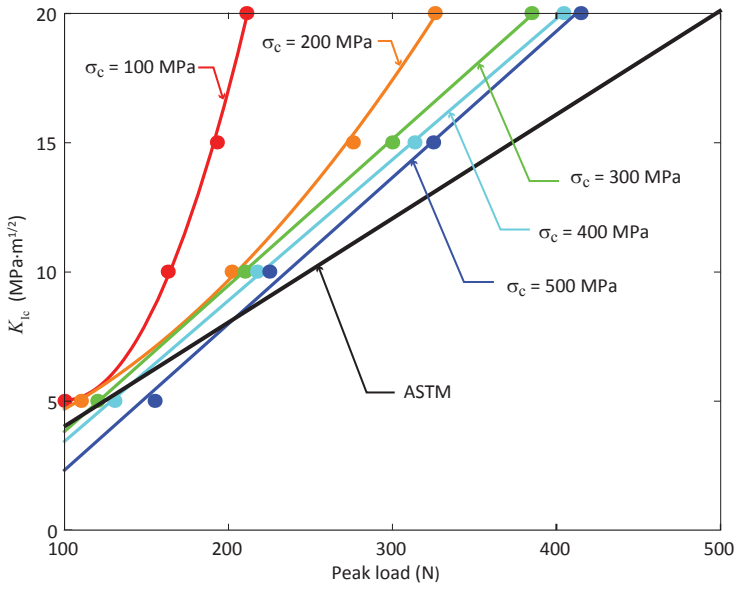

Figure 3.10: Critical stress intensity facture (fracture toughness) in a chevron-notched, four-point bending specimen. The black line is obtained based on ASTM C1421-16 [2] using the peak load as independent variable. The circles represent peak loads predicted from cohesive zone-based simulations for given fracture strengths and fracture energies, from which the corresponding critical stress intensity factors are estimated assuming plane stress conditions. The corresponding lines are interpolations of the simulation points.

This demonstrates the significant benefit of the new proposed geometry for the purpose of testing healing efficiency in self-healing materials.

3.5. Summary and Conclusions

A new chevron-notched, wedge-loaded specimen and testing method are proposed to retrieve the intrinsic fracture properties from semi-brittle materials using matching finite element calculations based on cohesive zone elements. The combination of simple test setup and advanced simulations allows unique and accurate determination of both the crack initiation and the crack propagation properties of (semi-) brittle materials while minimizing commonly necessary simplifications and assumptions. The addition of acoustic emission recording proves to be a strong tool to determine crack initiation and for tracking of crack length extension.

One important advantage of the proposed testing geometry and loading is that it allows to control crack growth and prevents full separation of the specimen. This is a critical requirement for testing self-healing materials in order to facilitate healing of the cracked surfaces. The latter approach was applied in Ti_2AlC samples that were cracked using a wedge-splitting test, healed and re-tested twice. Results of the self-healing testing will be presented elsewhere.

The simulations can be used to establish a simple closed-form formula for this geometry based on curve fitting. However, this would require extensive validation before it can be established as a standardized method, which is beyond the scope of the present work.

References

[1] M. Bengisu, *Engineering Ceramics*, 1st ed., Engineering Materials (Springer-Verlag Berlin Heidelberg, 2001).

[2] ASTM C1421 - 16, *Standard Test Methods for Determination of Fracture Toughness of Advanced Ceramics at Ambient Temperature*, Standard (ASTM International, West Conshohocken, PA, USA, 2016).

[3] S. W. Freiman and J. J. Mecholsky, *Fracture mechanics tests,* in *The Fracture of Brittle Materials* (John Wiley & Sons, Inc., 2012) pp. 32–67.

[4] W. Cai and J. Bisschop, *Optical method for measuring slow crack growth in cementitious materials,* Materials and Structures **45**, 1613 (2012).

[5] T. Whitlow, E. Jones, and C. Przybyla, *In-situ damage monitoring of a SiC/SiC ceramic matrix composite using acoustic emission and digital image correlation,* Composite Structures **158**, 245 (2016).

[6] W. G. Sloof, R. Pei, S. A. McDonald, J. L. Fife, L. Shen, L. Boatemaa, A.-S. Farle, K. Yan, X. Zhang, S. van der Zwaag, P. D. Lee, and P. J. Withers, *Repeated crack healing in max-phase ceramics revealed by 4d in situ synchrotron x-ray tomographic microscopy,* Scientific Reports **6**, 23040 (2016).

[7] L. Banks-Sills, *Update: Application of the finite element method to linear elastic fracture mechanics,* Applied Mechanics Reviews **63**, 020803 (2010).

[8] D. Nunez, K. Surana, A. Romkes, and J. Reddy, *J-integral for mode I linear elastic fracture mechanics in h, p, k mathematical and computational framework,* International Journal of Computational Methods in Engineering Science and Mechanics **10**, 345 (2009).

[9] R. Campilho, M. Banea, F. Chaves, and L. da Silva, *extended finite element method for fracture characterization of adhesive joints in pure mode i,* Computational Materials Science **50**, 1543 (2011).

[10] S. Esna Ashari and S. Mohammadi, *Fracture analysis of frp-reinforced beams by orthotropic XFEM,* Journal of Composite Materials **46** (2011), 10.1177/0021998311418702.

[11] L. P. Qiu, E. C. Zhu, and J. W. G. van de Kuilen, *Modeling crack propagation in wood by extended finite element method,* European Journal of Wood and Wood Products **72**, 273 (2014).

[12] Y. Xu and H. Yuan, *Computational analysis of mixed-mode fatigue crack growth in quasi-brittle materials using extended finite element methods,* Engineering Fracture Mechanics **76**, 165 (2009).

[13] X. Yang, J. Wan, C. Dai, Y. Zhang, W. Mao, Y. Zhou, and C. Lu, *Finite element analysis of crack propagation and fracture mechanical properties of freestanding 8 wt.% Y_2O_3–ZrO_2 coatings,* Surface and Coatings Technology **223**, 87 (2013).

[14] B. N. Jaya and V. Jayaram, *Crack stability in edge-notched clamped beam specimens: modeling and experiments,* International Journal of Fracture **188**, 213 (2014).

[15] I. Lancaster, H. Khalid, and I. Kougioumtzoglou, *Extended FEM modelling of crack propagation using the semi-circular bending test,* Construction and Building Materials **48**, 270 (2013).

[16] S. Li, L. Xiao, G. Song, X. Wu, W. G. Sloof, and S. van der Zwaag, *Oxidation and crack healing behavior of a fine-grained Cr_2AlC ceramic,* Journal of the American Ceramic Society **96**, 892 (2013).

[17] M. W. Barsoum, *Physical properties of the MAX phases,* in *Encyclopedia of Materials: Science and Technology (Second Edition)*, edited by K. H. J. B. Editors-in Chief: , W. C. Robert, C. F. Merton, I. Bernard, J. K. Edward, M. Subhash, and V. Patrick (Elsevier, Oxford, 2006) pp. 1–11.

[18] S. Li, G. Song, K. Kwakernaak, S. van der Zwaag, and W. G. Sloof, *Multiple crack healing of a Ti_2AlC ceramic,* Journal of the European Ceramic Society **32**, 1813 (2012).

[19] ASTM E647 - 15e1, *Standard Test Method for Measurement of Fatigue Crack Growth Rates*, Standard (ASTM International, West Conshohocken, PA, USA, 2015).

[20] ASTM B962-15, *Standard Test Methods for Density of Compacted or Sintered Powder Metallurgy (PM) Products Using Archimedes' Principle*, Standard (ASTM International, West Conshohocken, PA, USA, 2015).

[21] T. Hille, A. Suiker, and S. Turteltaub, *Microcrack nucleation in thermal barrier coating systems,* Engineering Fracture Mechanics **76**, 813 (2009).

[22] S. A. Ponnusami, S. Turteltaub, and S. van der Zwaag, *Cohesive-zone modelling of crack nucleation and propagation in particulate composites,* Engineering Fracture Mechanics **149**, 170 (2015).

[23] C. Gilbert, D. Bloyer, M. Barsoum, T. El-Raghy, A. Tomsia, and R. Ritchie, *Fatigue-crack growth and fracture properties of coarse and fine-grained Ti_3SiC_2,* Scripta Materialia **42**, 761 (2000).

[24] M. W. Barsoum, T. H. Scabarozi, S. Amini, J. D. Hettinger, and S. E. Lofland, *Electrical and thermal properties of Cr_2GeC,* Journal of the American Ceramic Society **94**, 4123 (2011).

[25] Y. P. Gan, X. K. Qian, X. D. He, Y. X. Chen, S. N. Yun, and Y. Zhou, *Structural, elastic and electronic properties of a new ternary-layered Ti_2SiN,* Physica B-Condensed Matter **406**, 3847 (2011).

[26] M. H. R. G. A. V. H. Romanus and P. Schaaf, *Tribological behavior of selected $M_{n+1}AX_n$ phase thin films on silicon substrates,* Surface and Coatings Technology **257**, 286 (2014).

[27] ASTM E399 - 12e3, *Standard Test Method for Linear-Elastic Plane-Strain Fracture Toughness K1C of Metallic Materials*, Standard (ASTM International, West Conshohocken, PA, USA, 2012).

4

Determination of the recovery of fracture mechanical properties of Ti_2AlC upon high temperature oxidation

An abnormal reaction to an abnormal situation is normal behavior.

Viktor E. Frankl

Co-contributors: Sathis A. Ponnusami, Sergio Turteltaub, Sybrand van der Zwaag, Willem G. Sloof

In this chapter, the recovery of fracture mechanical properties of a cracked sample of Ti_2AlC, upon high temperature oxidation is investigated using an experimental-numerical approach in combination with a newly developed test setup. A wedge-induced fracture test is used to allow the determination of the fracture mechanical properties of not only the virgin material but also that of the healed crack. A cohesive zone fracture mechanics-based crack healing model is utilized to model the cracking behavior in both conditions and to determine the values for fracture strength as well as fracture energy. In order to showcase the features of the model, parametric studies are conducted with varying the properties of healing material and the ratio of healed to total crack length. Further, healing efficiency is defined in terms of strength and energy recovery and their utility is demonstrated using the results of the parametric analysis. Fracture and healing experiments are conducted on a single Ti_2AlC specimen and the results are compared with the modeling outcomes.

4.1. Introduction

Quantification of self-healing efficiency in MAX-phase and composite ceramics relies on the comparison of reference, damaged and healed bending samples to determine a rough estimate of the strength regain through oxidation [1, 2]. The current experimental approach in which each sample can yield only data for only one particular condition (virgin, cracked or healing) leads to a high material consumption, a growing error margin and somewhat incomparable results. As discussed previously, in Chapter 3, the standard four-point bending test [3] requires stable crack propagation to be considered valid, something not commonly achieved with MAX-phase ceramics. Furthermore, while being relatively tough, four-point bending testing leads to full sample splitting and this mode of fracture renders it useless for quantitative determination of the recovery of its mechanical and fracture properties upon high temperature annealing

The new sample geometry, experimental setup and data processing protocol proposed in Chapter 3 allow controlled crack growth along a designated path without complete splitting of the sample and extraction of fracture energy and strength via finite element modeling using cohesive zone elements. Due to the crack tip being located within the sample at the end of the first fracture experiment, the partially cracked sample can thereafter be heat treated and re-cracked to determine the composite properties after healing. The direct comparison of the fracture response in both conditions for a single SPS produced Ti_2AlC sample is reported here. Ti_2AlC was selected as the MAX phase material to be used as its high temperature healing behavior is relatively well documented.

Cracks in Ti_2AlC are healed by the formation of dense and well-adhering Al_2O_3 that forms into the crack tips, as demonstrated by in-situ high resolution 3D X-ray tomography [4]. Furthermore, simple bending tests showed a strength regain of bulk Ti_2AlC for up to seven healing cycles [1]. While the work reported in this chapter deals with only one (technically successful) multi-step cracking & healing experiment, we believe the results reported here give a realistic indication of the actual material behavior and potential of the technique.

4.2. Experimental

4.2.1. Samples and test setup

Reactive sintering of Ti_2AlC was performed using a spark plasma sintering (SPS) furnace (HP D 25 SD, FCT Systeme GmbH, Germany). Starting powders of Ti (100 µm, >99.5 %, TLS Technik GmbH & Co., Germany), Al (45 µm, > 99.99 %, TLS Technik GmbH & Co., Germany) and Graphite (> 99.5, 6 µm, Graphit Kropfmühl AG, Germany) were mixed in a molar ratio of 0.85 : 1.05 : 1.15 for 12 h using a Turbula T2C Mixer (Willy A. Bachofer, Switzerland) with 5 mm alumina balls. Ti_2AlC disks with a diameter of 40 mm and 5 mm thickness were sintered at 1400 °C for 30 min.

The phase purity of the samples was determined via X-ray diffraction using a Bruker D8 ADVANCE diffractometer (Bruker, Germany) in the Bragg-Brentano geometry with a graphite monochromator and Co Kα radiation. The recorded X-ray diffractrograms were processed with Bruker software DIFFRAC.EVA 4.1 software. Elastic properties and Vickers Hardness were determined by Vickers indentation using a hardness tester (Zwick/Z2.5, Germany). Indents were created by loading the indenter with 5 N s^{-1} up to 50 N, hold-

ing for 12 s and unloading with 3.7 $N s^{-1}$. The density of the material was measured with the Archimedes method using an analytical balance (Mettler Toledo AG-204, Switzerland) according to ASTM B-962 [5]. The Ti_2AlC samples had a relative density of 95% or higher.

All machining was carried out by electric discharge machining (EDM) with wire diameters of 0.25 and 0.1 mm.

The details of the chevron-notched, wedge-loaded specimen geometry (WLS) can be found elsewhere (Chapter 3). Here, samples with a basal half-length HW of 12 mm, a height W of 25 mm and thickness B=5 mm were used. Experiments were carried out using a 100 kN electro-mechanical load frame (Series 5500R, Instron, USA) that was fitted with a 10 kN load cell to suit the recorded load levels. The sample was placed on a flat steel base-plate without further clamping. The quenched and tempered steel 10° wedge was lowered into the sample grove until it reached a pre-load of approximately 10 N.

Tests were carried out under closed-loop displacement control, with a fixed crosshead displacement rate of 0.01 or 0.1 $mm s^{-1}$, monitored by a dynamic strain gauge extensometer (2620 Series, Instron). The crosshead motion was stopped when a load drop of 50% from peak load was recorded. To determine the residual load bearing capacity reloading of an un-oxidized specimen was performed up to 95% load drop. Upon termination, the crosshead motion was reversed leading to retraction of the wedge. Unloading curves were not recorded.

All tests were accompanied by the recording of the acoustic events during the fracturing process, using the Physical Acoustics module (PCI-2, 2 channel 40 MHz 18 bit data-acquisition combined with ILS40 pre-amplifiers). Registration and post-processing were performed using the Physical Acoustics AEWin 1.70 (2005) software module. Prior to each experiment, two microphones were attached to the right and left of the sample groove with paraffin wax. The sampling rate of 2 MHz with a 20 dB amplification factor were used. An acoustic event was recorded if the signal level of any microphone exceeded 5 mV. The energies recorded varied in a wide range between 1 aJ to 1 nJ. A cumulative energy as a function of time, termed the "acoustic energy", was obtained through post-processing of the acoustic events.

Samples subjected to healing were oxidized at 1200 °C for 2 h in laboratory air using an alumina tube furnace (LTF 16/75/610, Lenton, UK) and cooled with a rate of 10 °C min^{-1}.

4.2.2. Crack healing model

The crack healing model utilised in this work is adopted from [6] and is briefly outlined here for completeness. The healing model is a composite-based constitutive model for simulating the recovery of fracture properties upon activation of crack healing. The traction (or the stress) components of the composite law, t^c is expressed as a weighted sum of the traction contributions, t^o and t^h respectively, from the original and the healed material (i.e the new material formed out of the matrix material and deposited in the original crack gap) as given in the following equation,

$$t^c = (1-w)\,t^o + w\,t^h \tag{4.1}$$

where the superscripts o and h represents original and healing materials respectively.

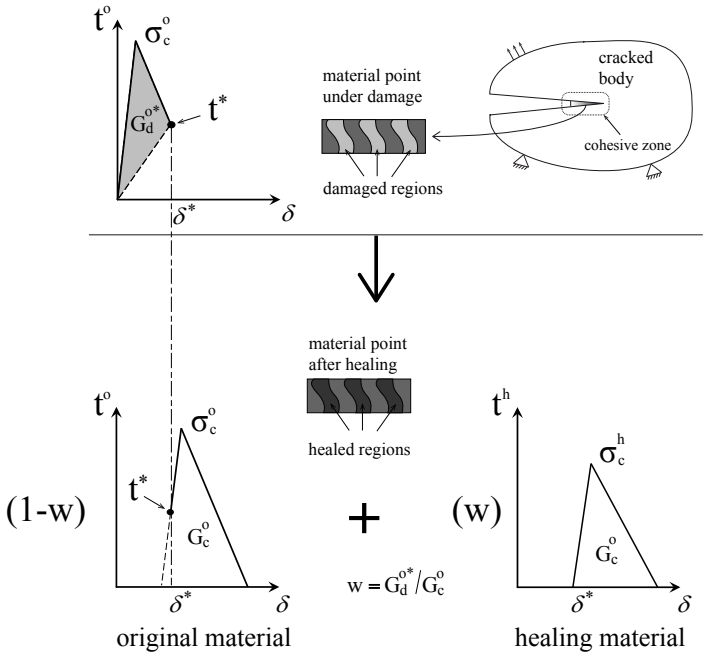

Figure 4.1: Schematic description of crack healing model utilized in this work. A composite traction-separation law is derived from a weighted sum of original and healing material phases.

One of the primary parameters in the model is the weighting factor, w. The variable, w, correspond to the volume (or in the case of a 2D analysis: area) fraction of healed material. A schematic of the traction-separation laws for a material point under damage and healing is shown in Figure 4.1.

The value of the weighting factor, w, varies from 0 to 1. Upon healing activation, a value $w = 0$ represents zero equivalent damaged area fraction of the original material at a given material point (or in other words, original material is fully intact) and $w = 1$ represents the condition at which the healing material would fully occupy the previously damaged material point. A primary interest in the self-healing materials community is to quantify the recovery of the mechanical properties upon healing. Two main recovery factors or efficiencies could be relevant to quantify the effect of healing. First, the percentage increase in the peak load before and after healing of the fractured specimen, given by η_p in equation 4.2a. And the second, the percentage gain in the amount of energy that can be dissipated during fracture of the cracked specimen before and after healing, given by η_g in equation 4.2b. These two factors given below, are utilized to arrive at quantification of property recovery from the resulting load-displacement response of virgin and healed samples.

$$\eta_p = \frac{P_h - P_r}{P_o - P_r} \tag{4.2a}$$

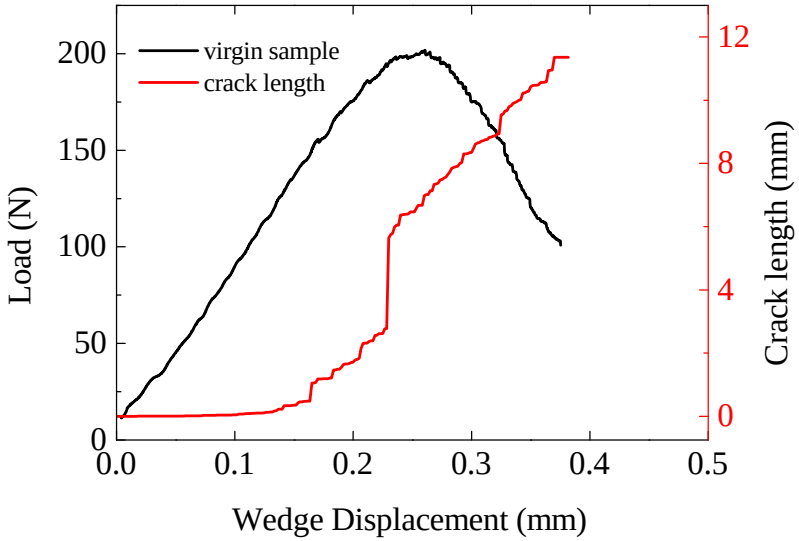

Figure 4.2: Load-displacement curve and corresponding acoustic emission signal normalized to the final recorded crack length of 11.36 mm of virgin Ti_2AlC.

$$\eta_g = \frac{G_h - G_r}{G_o - G_r} \tag{4.2b}$$

where the subscripts h, r and o stand for healed, fracture and original sample, respectively.

4.3. Results and discussion

4.3.1. Material characterization

Ti_2AlC synthesized by spark plasma sintering from elemental powders resulted in high purity dense material, according to XRD. The average grain is around 50 ± 20 µm in length and 25 µm wide. Density measurements revealed less than 5% porosity. Vickers indentation tests with loads of 50 to 1000 N revealed a constant Vickers hardness of 2.5 GPa.

4.3.2. Fracture response of the virgin sample

The fracture response of Ti_2AlC to wedge loading was previously discussed and analyzed in Chapter 3. The crack growth is stable during loading, as can be seen from the recorded acoustic emission data shown in Figure 2. The transition from chevron notch to groove causes a jump in crack growth and cracking begins before peak load is reached. The final crack length, as determined by scanning electron microscopy, is 11.36 mm.

For the Ti_2AlC sample considered here, finite element simulations of the wedge test using cohesive elements are conducted with varying parameters that include friction

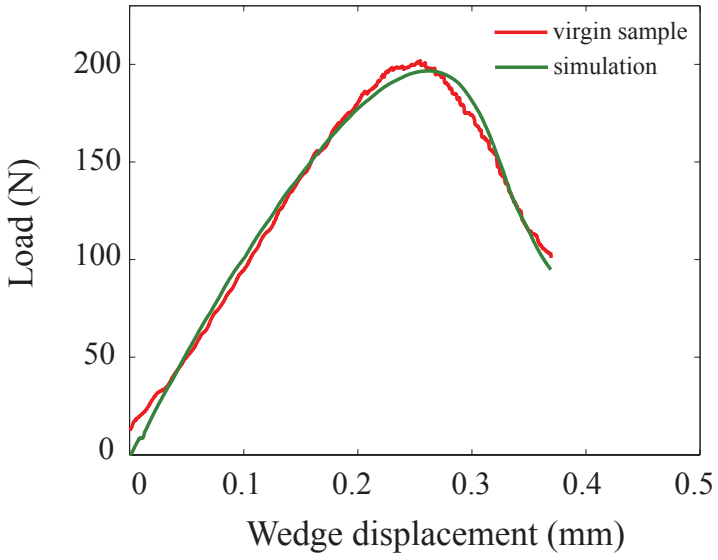

Figure 4.3: Load-displacement response of virgin specimen. Comparison between experiment and simulation. Material properties used for the simulation: fracture strength is 200 MPa, fracture energy is 1.5 N mm^{-1}, Young's modulus is 260 GPa, friction coefficient is 0.05.

coefficient, fracture strength and fracture energy of the material. Young's modulus of the Ti_2AlC ceramic is well documented in the literature and a value of 260 GPa is used in the simulations. The friction coefficient is tuned to a value such that the initial slope of the load-displacement response from the simulations matches with the experiments and a value of 0.05 was obtained.

A range of fracture property values (strength and fracture energy) are considered as a set of parametric simulations, and the simulations are compared with the experimental load-wedge displacement curve and the crack area- wedge displacement curves. The crack area refers to the surface area of the crack created during the fracture process as determined by acoustic emission and assuming a linear relation between the transient integrated acoustic emission signal and the transient crack area (crack length x actual sample width at the crack tip position). The constant in this relation was determined from the final crack length 11.36 mm and the total integrated acoustical signal up to the corresponding wedge displacement (excluding unloading effects). It should be mentioned that experiments using long range optical microscopy and digital image capturing to track the crack tip position did not lead to a final set-up and data handling process to determine the actual crack tip position during sample loading with enough accuracy.

The simulations for a fracture strength of 200 MPa and a fracture energy equal to 1.5 N mm^{-1} yielded an excellent agreement between experimental and computed behavior for both data sets as shown in in Figures 4.3 and 4.4.

It can be observed that the actual initiation of the crack is well captured in the sim-

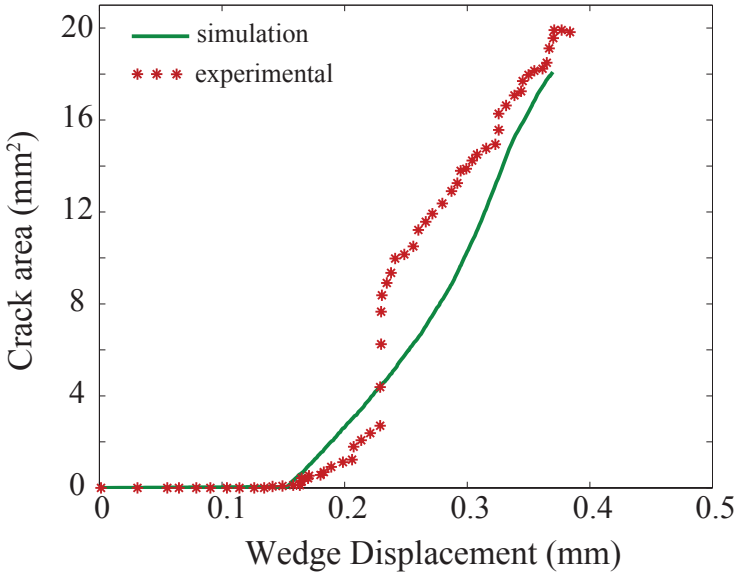

Figure 4.4: Evolution of crack growth. Comparison of crack area between experiment and simulation.

ulation while the actual evolution of the crack area with increasing wedge displacement shows a slightly bigger deviation, but well within the expected variability of such a tough ceramic.

4.3.3. Healing behavior

The total testing protocol of the experiment reported here consisted of three cracking cycles with two intermediate healing cycles. Healing treatments were conducted in air at 1200 °C for 2 h. The oxidation treatments resulted in a total surface oxide scale of 350 µm. According to post-mortem sample investigations, oxidative crack filling was found for a crack length of approx. 4 mm. Hence, the remaining approx. 7 mm of the crack at the onset of the third wedge-loading cycle were unfilled.

As known, Ti_2AlC heals micro cracks by formation of Al_2O_3 and minor amounts of TiO_2 [1, 4, 7]. The double oxidation treatment at 1200 °C for 2 h of the Ti_2AlC sample considered here resulted in a mixture of both oxides. Rutile is present almost to the same extent as Al_2O_3.

The oxidation treatment of cracks induced in wedge loaded Ti_2AlC resulted in a lower degree of crack gap filling than previously reported, [4] possibly due to a larger crack gap (± 10 µm), but not fully understood at this point.

According to post-mortem cross-section analysis, cracks in the Ti_2AlC WLS propagated roughly along the same path during each loading. Consecutive cracks weave in and out of the oxides formed during a previous healing step, see Figure 4.5.

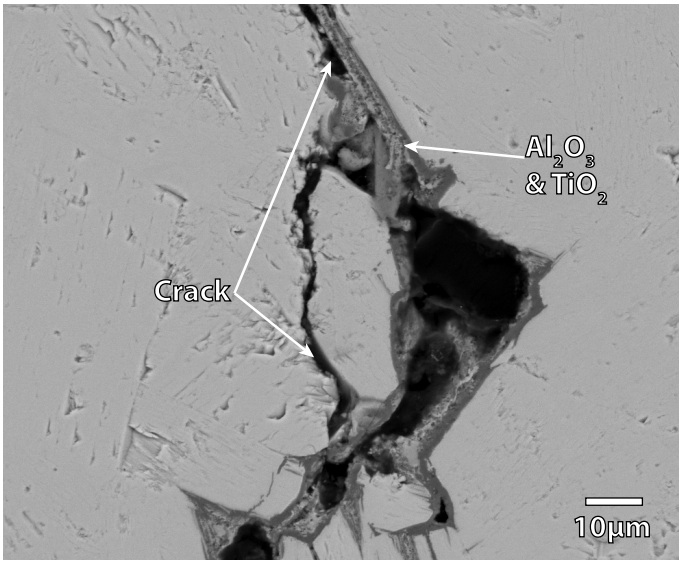

Figure 4.5: SEM backscattered electron image of cross-sectioned Ti_2AlC sample cracked 3 times with two intermediate healing treatments. The final induced crack runs through the previously formed TiO_2 and Al_2O_3, as indicated.

4.3.4. Fracture response of the healed sample

For reference, a separate Ti_2AlC wedge-loaded specimen was subjected to loading, unloading and reloading without any intermediate healing procedure. The goal being to show that the peak load is a good qualitative indicator of healing. The initial fracture proceeded in an identical manner to others, previously described here and in Chapter 3. The test was stopped after a load drop of 50% from 220 N, i.e. final value at 110 N, was recorded.

The peak load recorded after re-loading corresponded to the last measured loading point of the initial test, i.e. 110 N. This agreement of peak load and residual load bearing capacity, seen when no oxidation treatment is applied, can be considered the benchmark behavior for non-healed materials.

The experimental and simulation based quantification of healing efficiency of Ti_2AlC require clear and reliable data on loading, wedge-displacement and crack length. During re-loading after a first oxidation treatment at 1200 °C for 2 h, technical difficulties rendered the results insufficient for a simulation based evaluation. Specifically, the wedge-displacement recording was deemed unrealistic (visual observation and recorded values did not coincide) and hence unreliable.

We thus present the final recorded loading curve, after two oxidation treatments at 1200 °C at 2 h and an intermediate loading experiment. The objective, to demonstrate self-healing quantification by means of experiment and a cohesive zone based finite element modeling is not impaired by use of the final load-displacement recording.

The peak load of 160 N for the wedge loaded Ti_2AlC specimen treated twice at 1200 °C for 2 h clearly exceeds the residual load of approx. 100 N of the virgin sample, see Figure

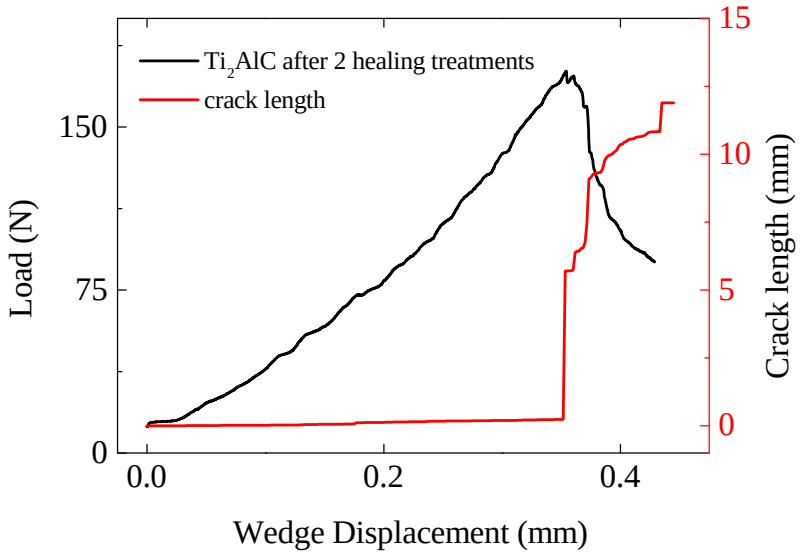

Figure 4.6: Load-displacement curve and corresponding acoustic emission signal of Ti_2AlC after 2 crack-healing cycles and a final crack length of 11.9 mm.

4.6. In line with the benchmark experiment described above (no oxidation treatment), this result clearly indicates that a recovery of fracture properties has been achieved.

As mentioned earlier, one of the key parameters that decide the healing efficiency is the extent to which the crack is filled and healed by the formation of well-adhering oxides. The healing product formed by oxidation of Ti_2AlC is assumed to be mainly alumina, which is a strong but brittle material in relation to the original material, i.e. Ti_2AlC. In this context, the strength of the healing material is taken equal to 400 MPa and the fracture energy is assumed to be 0.1 $N\,mm^{-1}$ as against the values 200 MPa and 1.5 $N\,mm^{-1}$ for Ti_2AlC.

To demonstrate the effect of crack filling, different ratios of the healed to total crack length, l_h/l_c are considered in the simulations and the results are reported. The resulting load-displacement responses for five different ratios are shown in Figure 4.7. It is worth mentioning that the initial crack length, l_c, is the length of the crack after first cracking of the specimen and before any healing process is started. From the results, it can be seen that with increase in the ratio of the healed crack length to the total crack length, the recovery of the load increases.

To better visualize the recovery of the load carrying capability, the two efficiencies defined earlier are used. From the plots shown in Figure 4.8, it can be observed that if the crack is completely healed by high strength alumina, complete recovery of mechanical properties is obtained both in terms of strength and fracture energy, revealed through the data points corresponding to 100% efficiency. It is worth recalling that, the healed product acts as a perfect bonding phase between the crack faces, resulting in post-healed

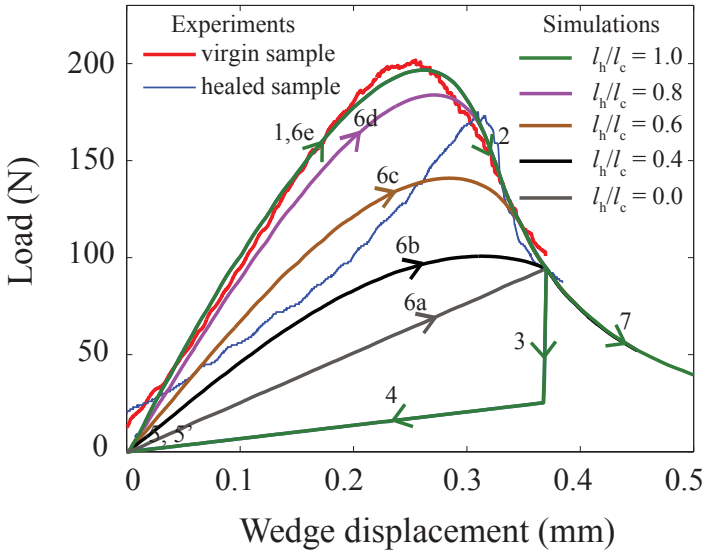

Figure 4.7: Load-displacement responses for varying ratios of healed length to total crack length. 1,2 ⟶ loading (cracking); 3,4,5 ⟶ unloading; 5,5' ⟶ healing phase; 5',6,7 ⟶ reloading post healing

crack initiating and growing in a different path in the matrix (or original) material. For cases in which partial healing is considered, the efficiencies decreases as shown in the figure. For instance, for a healed crack length ratio of 0.5, the strength and energy-based healing efficiencies are about 20% and 40% respectively. This indicates that strength recovery is more affected by the healed length ratio than the fracture energy recovery. It is to be noted that the strength and energy that is referred to, are related to specimen properties rather than material properties.

According to the results shown in Figure 4.7 the best match of simulation to experimental loading curve is found for a ratio between 0.6 and 0.8 of healed to original crack length. This approximately corresponds to a healing efficiency of up to 80% in terms of strength. As fracture energy is a measure of the area beneath the load-displacement curve, the best match ratio of l_h/l_c = 0.6 results in a healing efficiency of approx. 55% (Figure 4.8).

The experimentally resolved value of 0.4 for l_h/l_c does not match the amount of healing the model assumes necessary for the recorded load-displacement curve. The effect of TiO_2 formation within the crack, modifying the healing material properties, is neglected in the simulation approach.

Finally, it should be stated that the path of the crack as observed experimentally is not explicitly modeled at the level of the actual microstructure in the healed crack. The incomplete healing and oxide mixture leads subsequent cracks to wind in and out of the scar zone, as shown in Figure 4.5. The simulation cannot, at this point, capture the crack evolution through areas of incomplete oxide filling, but assumes full ideal healing

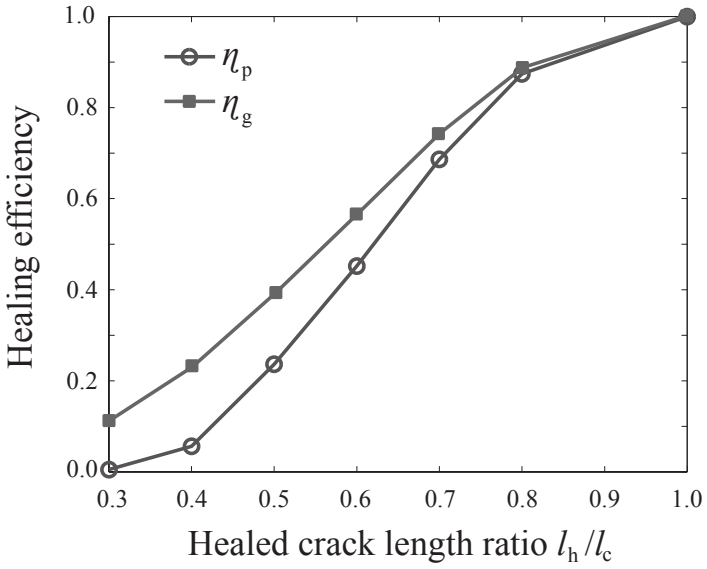

Figure 4.8: Healing efficiency with reference to recovered specimen strength η_p and fracture energy η_g.

in oxidized areas.

4.4. Conclusions

Determination of healing efficiency in terms of fracture strength and fracture energy by combination of experiments and advanced simulations was successfully demonstrated for Ti_2AlC. Wedge-loaded samples underwent two healing cycles (cracking-healing being one cycle) before recording the final load displacement curve to determine the fracture strength and fracture energy after healing.

Two healing treatments at 1200 °C for 2 h lead to a measurable increase in the peak-load, i.e. 160 N versus the residual load-bearing capacity of 100 N. Finite element calculations based on cohesive zone elements determined the healing efficiency in terms of strength to be approx. 80%. In terms of fracture energy an efficiency of 55% was established.

Further experimental studies are needed to determine the exact healing oxide properties (mixture of TiO_2 and Al_2O_3), which can be used to improve and validate the model to increase the accuracy of healing efficiency quantification.

References

[1] S. Li, G. Song, K. Kwakernaak, S. van der Zwaag, and W. G. Sloof, *Multiple crack healing of a Ti_2AlC ceramic,* Journal of the European Ceramic Society **32**, 1813 (2012).

[2] G. M. Song, Y. T. Pei, W. G. Sloof, S. B. Li, J. De Hosson, and S. van der Zwaag, *Oxidation-induced crack healing in Ti_3AlC_2 ceramics,* Scripta Materialia **58**, 13 (2008).

[3] ASTM E399 - 12e3, *Standard Test Method for Linear-Elastic Plane-Strain Fracture Toughness K1C of Metallic Materials*, Standard (ASTM International, West Conshohocken, PA, USA, 2012).

[4] W. G. Sloof, R. Pei, S. A. McDonald, J. L. Fife, L. Shen, L. Boatemaa, A.-S. Farle, K. Yan, X. Zhang, S. van der Zwaag, P. D. Lee, and P. J. Withers, *Repeated crack healing in MAX-phase ceramics revealed by 4d in situ synchrotron x-ray tomographic microscopy,* Scientific Reports **6**, 23040 (2016).

[5] ASTM B962-15, *Standard Test Methods for Density of Compacted or Sintered Powder Metallurgy (PM) Products Using Archimedes' Principle*, Standard (ASTM International, West Conshohocken, PA, USA, 2015).

[6] S. A. Ponnusami, J.Krishnasamy, S. Turteltaub, and S. van der Zwaag, *A crack healing model for self-healing materials,* Engineering Fracture Mechanics (submitted).

[7] A.-S.Farle, L. Boatemaa, L. Shen, S. Gövert, J. B. W. Kok, M. Bosch, S. Yoshioka, S. van der Zwaag, and W. G. Sloof, *Demonstrating the self-healing behaviour of some selected ceramics under combustion chamber conditions,* Smart Materials and Structures **25**, 084019 (2016).

5

On the autonomous high temperature self-healing capacity of spark plasma sintered Ti_3SiC_2

Never tell me the odds.

Han Solo

Co-contributors: Guoping Bei, Toshio Osada, Sybrand van der Zwaag, Willem G. Sloof

We report on the healing and oxidation behavior of a Si-containing MAX-phase variant, Ti_3SiC_2. Oxidation of spark plasma sintered Ti_3SiC_2 at 1100, 1200 and 1300 °C *for up to* 45 h *revealed formation of dense TiO_2 and Si-oxide on the exposed sample surfaces. Healing of thermally shocked and mechanically fractured samples by annealing at* 1200 °C *for up to* 1 h *showed partial crack gap filling. A newly developed chevron notched, wedge loaded specimen (WLS) configuration was used to induce controlled cracks in order to semi-quantitatively assess the self-healing efficiency.*

5.1. Introduction

$M_{n+1}AX_n$-phase ceramics are materials composed of transition metals (M), elements from groups 14 and 15 (A) and Carbon or Nitrogen (X), exhibiting metal and ceramic like properties, such as high temperature strength and stability, semi-ductile failure mode and high thermal and electrical conductivity [1]. Furthermore, some of these ternary carbides have been shown to self-heal crack damage by autonomous, intrinsic high temperature oxidation. At temperatures above 1000 °C Ti_2AlC, Ti_3AlC_2 and Cr_2AlC can fill cracks by formation of dense, strong Al_2O_3, which adheres to the fracture surfaces and can reach into the depth of the cracks, as previously observed by in-situ time-resolved high-resolution synchrotron 3D X-ray tomography [2]. This crack closure by a strong and well adhering oxide leads to a partial or even complete restoration of the tensile strength [3] and is therefore highly desirable from an application perspective. More recent research work on oxidation induced crack healing in a Ti_2SnC MAX phase showed promising healing abilities at lower temperature (<1000 °C). After exposure of a thermally shocked Ti_2SnC specimen to 800 °C for 1 h in air, the electrical conductivity and three point bending strength could be almost fully recovered [4].

A previous study [5] (cf. Chapter 2) predicted which of the more than 75 known MAX phase compounds would also show such a desirable self-healing behavior at high temperatures. The prediction was made on the basis of a number of postulated criteria related to intrinsic (physical) material properties of both the initial material and the reaction product formed. The likelihood of desired oxide formation was predicted by analysis of Gibbs free energy of oxide formation for M and A-element constituents and the diffusivity of the oxidizing element. Expected A-element oxides were further investigated to supply a sufficient volume expansion and good adhesion to the matrix, as well as comparable coefficients of thermal expansion (CTE) and Young's moduli [5]. The study identified only one non-Al_2O_3 forming MAX phase to have self-healing potential: Ti_3SiC_2.

Ti_3SiC_2 is the first 312 MAX phase to be synthesised in bulk form, [6, 7] and hence has been thoroughly investigated from its synthesis to its tribological behavior [8–10], yet its oxidative crack-gap filling behavior and subsequent strength recovery have not yet been demonstrated. Ti_3SiC_2 synthesis routes have included reactive sintering [11], arc melting [12], mechanically induced self-propagating reaction [13] and magnetron sputtering [14], amongst others. Of the known MAX phases Ti_3SiC_2 exhibits one of the highest elastic moduli, 340 GPa [15], a high fracture toughness, KIC of 7.0 MPa$\sqrt{m}$ [8], as well as relatively high thermal expansion coefficient CTE of 9.1 x 10^{-6} K^{-1} [16].

Strength recovery of a cracked Ti_3SiC_2 specimen by high temperature oxidation is expected to be achieved mainly via SiO_2 formation, but some TiO_2 formation is possible too, as the Gibbs free energy of oxide formation is about the same. Healing by TiO_2 formation has previously been demonstrated in ceramic composites, such as Al_2O_3/TiC. Oxidation below 1200 °C under combustion conditions lead to lateral growth of TiO_2 into the crack depth[17]. Tensile strength of Al_2O_3 composites with 15 and 30 vol.% TiC could be fully regained by 1 h of oxidation at 800 °C [18]. The use of SiC particles as healing agents has been demonstrated in Mullite [19], Al_2O_3[20], Si_3N_4 [21] and ZrO_2 [22]. In all cases the SiC reacts upon damage to form SiO_2 with a volume expansion of up to 80 % to fill cracks. The additional crystallization and excellent bonding of SiO_2 to the matrix are due to a high exothermal heat development upon oxidation [23]. Nakao *et al.* [24]

showed that incorporation of 15 vol.% of 270 nm SiC particles in Al_2O_3 can lead to full strength recovery by oxidation at 1200 °C for 10 h.

To investigate the full potential of Ti_3SiC_2 for self-healing by high temperature oxidation, thermal gravimetric analysis of bulk spark plasma sintered samples was performed at 1100, 1200 and 1300 °C for 10 to 45 h. To qualitatively determine optimal healing conditions, thermally shocked samples were healed at different combinations of temperatures and time. A newly-developed chevron notched wedge loaded specimen (WLS) configuration, see Chapter 3 was used to induce controlled cracks to assess the recovery of fracture properties upon healing in a more quantitative manner.

5.2. Experimental

Samples of Ti_3SiC_2 were synthesized by direct synthesis in a spark plasma sintering (SPS) furnace (HP D 25 SD, FCT Systeme GmbH, Germany). Powders of Ti (100 µm, > 99.5 %, TLS Technik GmbH & Co., Germany), Si (45 µm, > 99.99 %, TLS Technik GmbH & Co., Germany) and TiC (< 10 µm, 99 %, ChemPur, Germany) were mixed for 4 h using a Turbula T2C Mixer (Willy A. Bachofer, Switzerland) with 5 mm alumina balls. Different starting compositions with molar ratios of Ti : Si : TiC with Ti and Si as 1 and varying TiC content, viz.: 1.4, 1.5, 1.6 and 1.8, were sintered at 1500 °C for 4 to 8 h in 20, 40 and 50 mm graphite moulds under a uniaxial pressure of 50 MPa.

All samples were characterized using a scanning electron microscope (SEM), type JSM 6500F (JEOL Ltd., Tokyo, Japan) equipped with an energy dispersive spectrometer (EDS, type: ThermoFisher UltraDry 30 mm2 detector) for X-ray microanalysis (XMA) and with Noran System Seven software package for data acquisition and analysis. Optical microscopy was carried out using a digital microscope (Keyence VHX-100, Osaka, Japan). Image analysis was carried out using ImageJ Image Processing and Analysis software [25]. All samples were ground using SiC paper up to 4000 grit and subsequently polished with diamond suspension down to 1 µm grains.

X-ray diffraction was performed using a Bruker D8 Advance diffractometer Bragg-Brentano geometry and Lynxeye position sensitive detector and Cu Kα radiation. Sample density was determined with the Archimedes method using an analytical balance (Mettler Toledo AG-204, Switzerland) according to ASTM B 962-15 [26].

Oxidation behavior of spark plasma sintered Ti_3SiC_2 was studied by thermogravimetric analysis (TGA) using a high performance symmetrical TGA system (TAG 16/18, Setaram Instrumentation, France) to eliminate buoyancy effects. Bulk samples were oxidized at different temperatures (1100, 1200, 1300 °C) for 10 to 45 h in flowing dry synthetic air, i.e. 40 sccm N_2 (purity > 5N) and 10 sccm O_2 (purity > 5N).

Preliminary healing tests were performed on thermally shocked half-disks with a radius of 10 mm of sintered Ti_3SiC_2. To create cracks, polished samples were thermally shocked from 850 °C (Muffler Carbolite furnace, Heraeus, Germany), by dropping them in water at room temperature. This resulted in a pattern of fine cracks throughout the samples, with typical crack widths of up to 2.5 µm. These microcracks were healed at 1100 and 1300 °C for 1 or 2 h in laboratory air using an alumina tube furnace (LTF 16/75/610, Lenton, UK).

Self-healing efficiency was determined in a slightly more quantitative way, using a newly developed dedicated chevron notched, wedge loaded specimen (WLS) geome-

try, described in Chapter 3. Unfortunately, the Finite Element Model connected to the new configuration was not applicable to the mode of crack filling observed and hence could not be used to extract more precise information on the material properties of the healed material. Tests are performed using a 100 kN electro-mechanical load frame (type 5500R, Instron, Norwood (MA), USA) which was fitted with a 10 kN load cell to suit the recorded load, while displacement is monitored by a dynamic strain gauge extensometer (2620 Series, Instron, Norwood (MA), USA). The sample is placed on a flat steel plate without further clamping. A 10° quenched and tempered steel wedge is lowered into the sample groove until a pre-load of approx. 10 N is reached. Further loading is carried out at a crosshead displacement speed of 0.01 mm min^{-1} up to a load drop of 50% from peak load, at which point the crosshead displacement is stopped automatically and the wedge is withdrawn. The developed procedure results in a single macroscopic crack which stops within the sample, creating a potentially ideal condition for subsequent high temperature healing and testing of the fracture properties of both the sample and the healing product formed in the crack.

The fractured wedge loaded specimens are healed at 1200 °C for 1 h in laboratory air using an open alumina tube furnace and cooled with a rate of 10 °C min^{-1} (LTF 16/75/610, Lenton, UK).

5.3. Results and Discussion

The XRD analysis of Ti-Si-TiC with variable TiC content after SPS sintering in Figure 5.1. The sintered samples consist mainly of Ti_3SiC_2 with some traces of TiC. The diffraction intensity of TiC decreased with TiC content in the starting materials and very weak diffraction peaks could be detected in the final products when the TiC content varied from 1.4 to 1.6 mol in the starting materials. The total content of homogeneously distributed second phases amounts to approx. 15 %, see Figure 5.2.

All samples have relative densities of more than 95 % and contain randomly oriented and elongated grains with and aspect ratio of 3:1 (major grain size is about 90 µm, minor grain size is about 30 µm).

5.3.1. Oxidation Behavior

Oxidation of Ti_3SiC_2 was investigated at 1100, 1200 and 1300 °C for 10 to 45 h. According to XRD measurements all oxidized Ti_3SiC_2 samples were covered by a layer of TiO_2 (rutile), cf. Figure 5.3. No SiO_2 phase is detected indicating that any SiO_2 formed was in an amorphous or nano-crystalline state.

Cross-sections revealed mixed Si-Ti oxides below a dense uniform layer of TiO_2 for all samples, see Figure 5.4. At 1100 and 1200 °C the rutile scale and the underlying mixed oxide are separated by porosity. At 1300 °C this area is taken up by SiO_2, which, according to SEM-XMA likely is amorphous SiO_2 (dark grey; between III and IV in Figure 5.4c). The matrix-outer oxide interface in all samples appears to be SiO_2.

The overall oxidation reaction can be summarized as [27]:

$$Ti_3SiC_2 + 6O_2 \rightarrow 3TiO_2 + SiO_2 + 2CO_2 \tag{5.1}$$

or

$$Ti_3SiC_2 + 1.5TiC + 9O_2 \rightarrow 4.5TiO_2 + SiO_2 + 3.5CO_2 \tag{5.2}$$

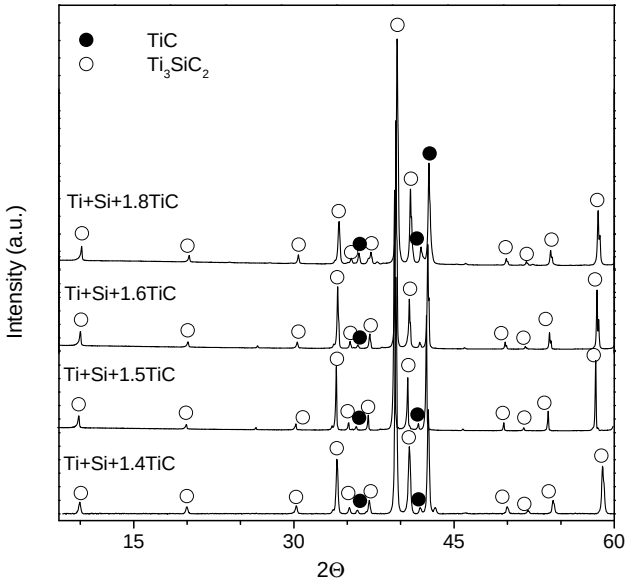

Figure 5.1: X-ray diffraction patterns for Ti_3SiC_2 spark plasma sintered from varying starting power molar ratios, viz.: Ti:Si:TiC = 1:1:X, with X equal to 1.4, 1.5, 1.6 and 1.8, respectively.

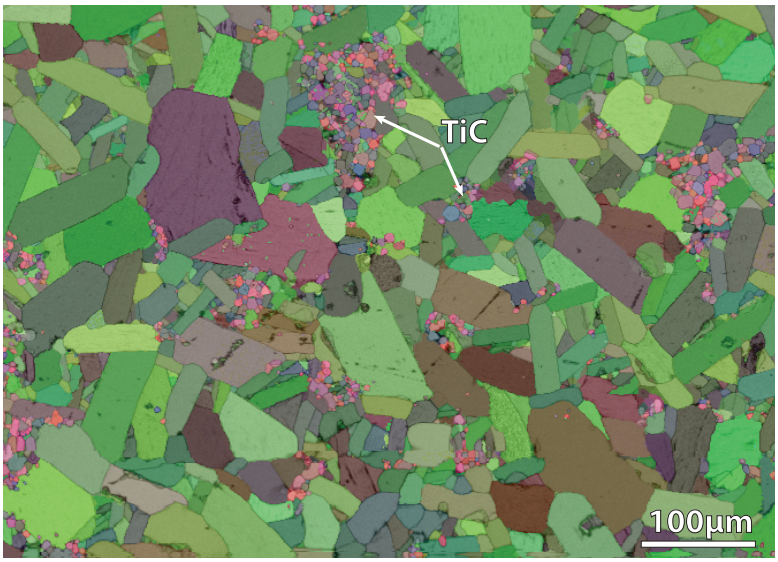

Figure 5.2: Microstructure of spark plasma sintered Ti_3SiC_2 from the starting composition of Ti:Si:TiC = 1:1:1.4, with TiC content indicated.

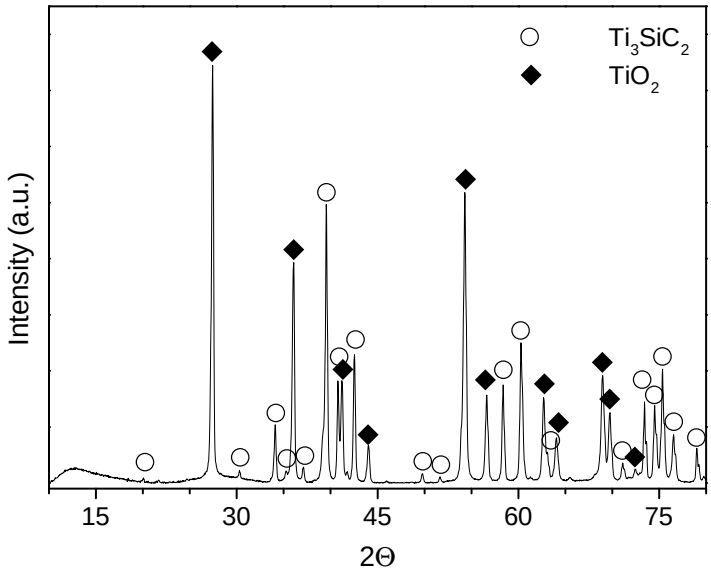

Figure 5.3: XRD pattern of Ti_3SiC_2 after oxidation at 1100 °C for 20 h.

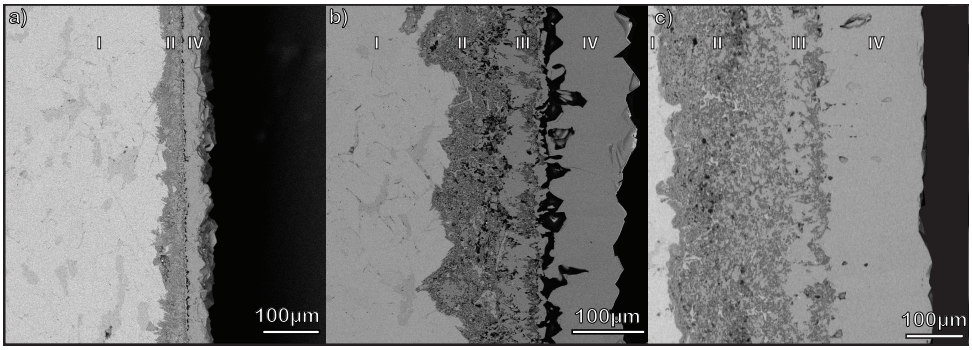

Figure 5.4: SEM backscattered electron images of cross-sectioned Ti_3SiC_2, oxidized at a)1100 °C for 20 h, b) 1200 °C for 20 h and c) 1300 °C for 10 h; with the following phase present and marked: MAX phase (I), mixed oxides of Si and Ti (II), Ti rich oxide layer (III) and pure dense TiO_2 (IV).

Carbon leaves the bulk material in form of gaseous CO_2, comparable to that shown in a previous study on Ta_2AlC oxidation [28](Chapter 6). According to Barsoum [29] and Lee [30] the Si is effectively immobile in the structure while the outward diffusion of Ti and inward diffusion of oxygen creates the dense rutile scale. The formation of cristobalite above 1240 °C, as observed by Barsoum [29], has not been confirmed in this study.

Samples of Ti_3SiC_2 oxidized at 1100, 1200 and 1300 °C were found to exhibit non-linear oxidation kinetics, see Figure 5.5. Oxidation at 1100 and 1200 °C initially proceeds parabolic and accelerates at longer holding times. At 1300 °C there is an initial deviation from parabolic kinetics. The datasets on the longer oxidation experiment at 1100 and 1200 °C show that there is excellent reproducibility.

The scale thickness in Figure 5.5a was calculated assuming all weight gain can be attributed to SiO_2 (cristabolite) and TiO_2 (rutile) in a ratio of 1:3. The maximum thickness derived for 10 h of oxidation at 1300 °C is 120 µm, which is significantly less than what is observed in the cross-sections. The discrepancy is due to the overestimation of the density for SiO_2 and the exclusion of porosity. Assuming a parabolic growth rate to hold true for most of the temperature-time domain explored, the recorded data results in an activation energy of 290 ± 10 kJ mol^{-1}, which is in good agreement with the value reported by Li *et al.* [31] (325 kJ mol^{-1}) and the values reported by Barsoum [27] (282 – 305 kJ mol^{-1}). The linear-parabolic kinetics at higher temperatures and longer times are not fully understood, but are generally associated with crack formation corresponding to the stress build up in the thick oxide layers [27].

A high sensitivity of the Ti_3SiC_2 oxidation rate to its TiC content and the duration of oxidation treatment has been named previously as a possible cause for the scatter in experimentally reported data [27, 30]. According to experimental results and a model, based on Wagner's oxidation theory, Ti_3SiC_2 with excess TiC is less oxidation resistant than pure Ti_3SiC_2 or Ti_3SiC_2-SiC [27].

For the conditions explored here, no cracks perpendicular or parallel to the surface were found in either oxide layer, though thermal stresses may occur due to the mismatch in thermal expansion coefficients, viz.: 6.8 - 8.3, 9 - 14 and 9.2 x 10^{-6} K^{-1} for TiO_2 (rutile), SiO_2 (crystabolite) and Ti_3SiC_2 [1, 32]. Cracking and spallation has been reported for

(a)

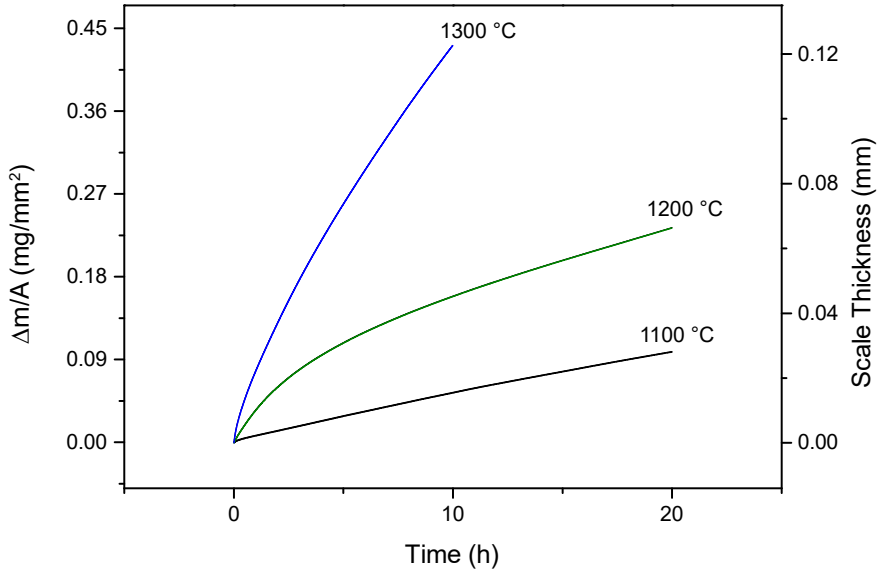

(b)

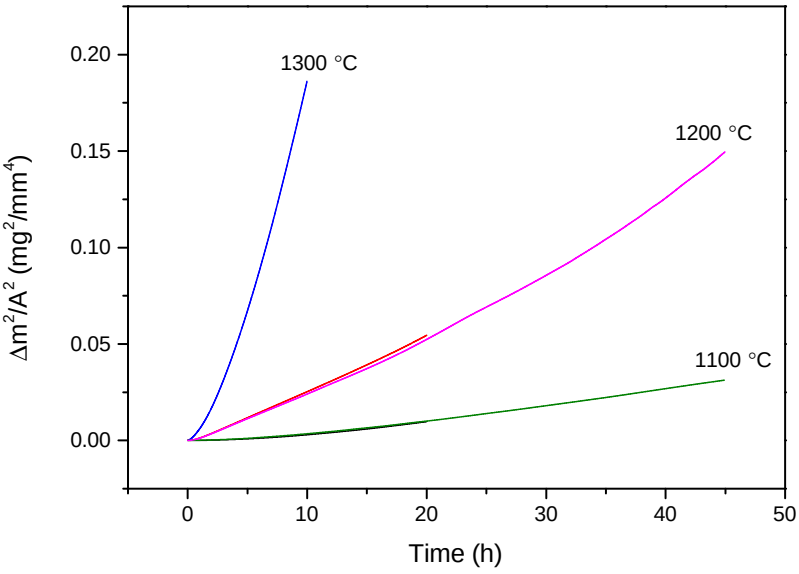

Figure 5.5: (a) Weight gain and calculated scale thickness for an oxide comprised of SiO_2:TiO_2 = 1:3 and (b) square or the normalized weight gain for isothermal oxidation in synthetic air for 10 to 20 h at 1100, 1200 and 1300 °C.

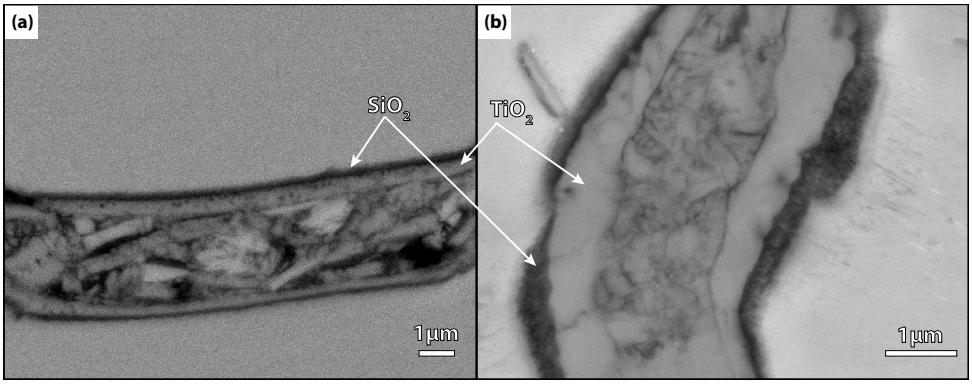

Figure 5.6: Crack in Ti_3SiC_2 (a) partially filled after oxidation at 1100 °C for 1 h and (b) fully filled after oxidation at 1300 °C for 1 h.

longer oxidation times or for oxidation at higher temperatures [29, 33].

Based on the results presented above, a crack width of 10 microns could be fully filled with oxides after 2 h of oxidation at 1100 °C, 1 h of oxidation at 1200 °C or approx. 45 min at 1300 °C.

5.3.2. Oxidative crack gap filling

To qualitatively determine optimal self-healing conditions for Ti_3SiC_2, oxidative crack gap filling was investigated for different temperatures (1100 up to 1300 °C) and times (1 and 2 h) using cracked samples produced via thermal shocking. Samples of varying starting composition, i.e. varying molar ratio of 1.4, 1.8 and 1.6 TiC with respect to Ti and Si, were used. As reported, the thermal shock treatment of Ti_3SiC_2 lead to crack patterns throughout the samples with maximum widths of approx. 5 µm.

Healing at 1100 °C for 1 h lead to complete filling of cracks smaller than 2.8 ± 0.3 µm. Cracks wider than that showed partial filling. All cracks exhibited oxidation products within their gap. An increase in oxidation time to 2 h had no measurable effect on the healing at 1100 °C.

At 1300 °C, oxidation for 1 h lead to full filling of all cracks produced by thermal shock. The increased temperature also resulted in a much larger surface oxide formation, of up to 80 µm.

The partially filled cracks in the 1100 °C samples were made up of SiO_2 at the crack wall interfaces, a rutile layer and coarse grains obstructing the crack gap, see Figure 5.6. The grains at the center of the crack are possibly non-reacted material, detached during cracking. At 1300 °C a progression of this morphology could be observed, where the oxides grown from both fracture surfaces have thickened and grains within the crack gap have oxidized to fill the entire volume, see Figure 5.6b.

The proposed reaction mechanism for oxidation and healing in Ti_3SiC_2 is:

$$Ti_3SiC_2 \rightarrow Ti_3C_2 + Si \tag{5.3}$$

$$Ti_3C_2 + 10O_2 \rightarrow 3TiO_2 + 2CO_2 \tag{5.4}$$

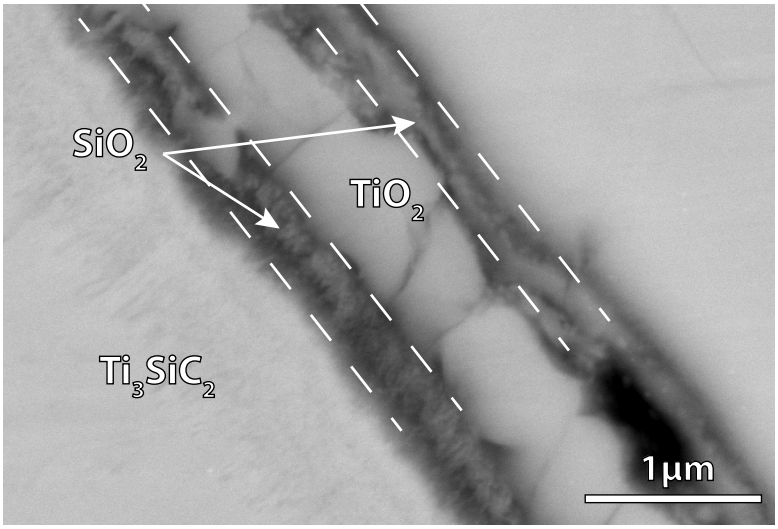

Figure 5.7: Crack in Ti_3SiC_2 after oxidation at 1300 °C for 1 h. Local compositions as identified by SEM-XMA are indicated.

$$Ti_3C_2 + 10O_2 \rightarrow 3TiO_2 + 2CO_2 \tag{5.5}$$

$$Si + O_2 \rightarrow SiO_2 \tag{5.6}$$

The de-intercalation of Si is a well-known process for the decomposition of MAX-phases [34, 35]. The relatively loose bonding of the Si atoms, leads to a high activity and mobility at elevated temperatures [36]. Upon liberation of Si the remaining Ti_3C_2 skeleton can relax into TiC_y which then proceed to oxidize. Titanium carbides are thermodynamically predicted to oxidize over Si, i.e. ΔG_{ox}(TiC) = -912.5 kJ mol^{-1}, ΔG_{ox}(Si) = -649 kJ mol^{-1}.

A comparable reaction process has been described for Ti_2SnC, where healing for 1 h at 800 °C resulted in a similar crack filling structure [4]. Hereby however the A-oxide (SnO_2), is sandwiched between M-oxide (TiO_2) interfaces [4]. It is presently unknown why an inverse crack gap filling is observed in Ti_3SiC_2 (i.e. the M-oxide (SiO_2) sandwiched between A-oxides (TiO_2)). It has been postulated that the combination of the reported high Ti-diffusion and the essentially immobile nature of the Si plays and important role [27].

Cracks generated during wedge loading experiments are expected to be wider (i.e. typically up to 10 µm) than those seen in the thermally shocked samples. The incomplete healing of cracks larger than 2.8 µm at 1100 °C for 2 h, large surface oxide scale formation at 1300 °C and the oxidation kinetics of Ti_3SiC_2 at 1100, 1200 and 1300 °C (cf. Figure 5.5), 1 h of oxidation at 1200 °C was used for the final study of healing and strength recovery in Ti_3SiC_2 using the wedge loading set-up.

5.3.3. Semi-quantitative healing efficiency of oxidized Ti_3SiC_2

Strength recovery and healing of Ti_3SiC_2 was measured using the chevron notched, wedge loaded specimen (WLS) described in the experimental section and in more detail in Chapter 3. As stated, samples were cracked and healed at 1200 °C for 1 h before re-cracking under identical circumstances. We report only the results of one fracture and healing experiment, but the results of the incomplete prior experiments suggest that the data reported here, reflects the behavior to be expected for this material quite well. All samples used for wedge-loaded crack-healing tests were synthesized from Ti:Si:TiC = 1:1:1.4 powder mixture.

Wedge loading of spark plasma sintered Ti_3SiC_2 WLS using the protocol described in the experimental section resulted in a crack of about 10 mm length. The width varied slightly along the crack length, but on average was around 9 ± 1 µm, with a sharp crack tip. The fracture strength of the virgin Ti_3SiC_2 sample is 180 MPa, which was previously extracted by simulation based extended finite analysis, cf. Chapter 3. After a single healing treatment at 1200 °C for 1 h, approx. 40 % of the crack gap is filled by oxide products.

The crack filling morphology is identical to the healing achieved at 1100 and 1300 °C for cracks up to 2.5 µm. Cracks wider than 5 µm show oxidation progression in form of rutile growth on SiO_2 from both crack faces, though insufficient to bridge the whole gap. Mixed course grained oxides, as shown in Figure 5.6 were not observed in the healed WLS. Oxidation occurs throughout the length of the crack, indicating that crack width, rather than length limited the crack filling efficiency.

Recorded load-displacement curves of the virgin and healed sample are shown in Figure 5.8. The proposed unloading of the virgin sample is shown with a dashed line, as it could not be recorded due to lodgement of the sample on the wedge. In in Figure 5.8 the wedge-displacement of the second recorded loading curve is corrected by a factor corresponding to the crack opening displacement remaining from the previous wedge-loading. In this case, a crack opening of 9.1 µm was observed via SEM at the chevron tip, corresponding to a difference in wedge displacement of approx. 0.06 mm, as indicated in Figure 5.8 (red arrow).

The difference in slope during loading from virginal to partially healed Ti_3SiC_2 is noteworthy and due to the change in nominal stiffness of the specimen. Partial crack gap filling modifies the apparent Young's modulus of the now composite-like material.

Even complete filling of the crack with the afore described sandwiched TiO_2-SiO_2 structure, a maximum Young's modulus of the healing composite would amount to E_{crack} ≈ 184 GPa, compared to the virginal Ti_3SiC_2 E-modulus of 320 GPa (Chapter 3). Any change in E-modulus leads to a change in slope for re-loading, even of an ideal healed material. The achieved peak load is dependent on fracture toughness and strength as reported in the previous chapter. However, for the incomplete filling of the crack with a semi-porous and amorphous phase the reported FEM model could not be used to estimate the fracture toughness and the crack propagation energy of the healed crack.

Beyond the change in slope, cracking begins earlier in the partially healed specimen, than in an intact sample. Crack initiation in the chevron notch of the virgin Ti_3SiC_2 WLS was shown by acoustic emission measurement to begin at approx.144 N of load, corresponding to a wedge displacement of 0.1 mm, see Chapter 3. The healed sample clearly shows crack development at approx.104 N, when a distinct change in slope ap-

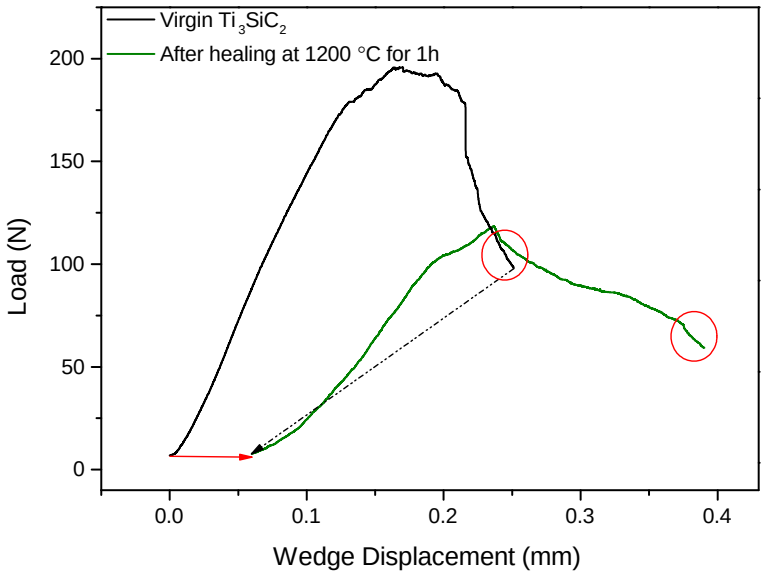

Figure 5.8: Load-Displacement curves of virgin and healed wedge loaded samples. The proposed unloading curve of the virgin sample is indicated (dashed black) and the second (green) curve was shifted to compensate for residual crack opening displacement (red arrow). The red circles show the identical material response for both materials for the final loading stages.

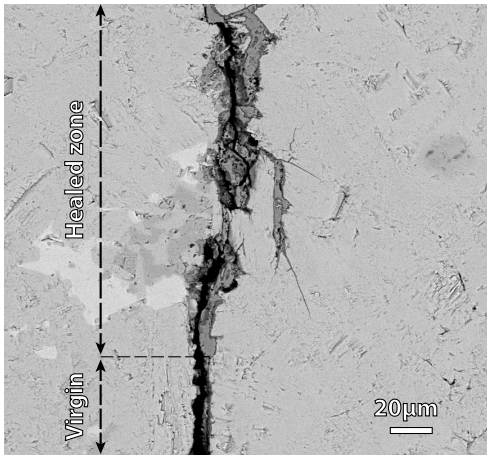

Figure 5.9: SEM-backscatter image of a crack propagating beyond the healed zone, into virgin material.

pears. Post-mortem crosssections show that the partially healed initial crack guides and contains the subsequent crack. The early onset of cracking at approx.104 N corresponds to the ease of fracture in the partially healed crack.

However, the healed sample, with partial crack gap filling, reaches a higher peak load than the residual load bearing capacity demonstrated by the virgin material. After healing at 1200 °C for 1 h the peak load exceeds the residual load bearing capacity of 98 N by approx. 20 %, peaking at 118 N, indicating mechanical healing.

Significantly, both curves display similar slopes towards the end of their respective loading sequences (see Figure 5.8), which can be considered evidence that crack propagation in the second recording has extended beyond the healed initial 10 mm crack. Further crack growth proceeds through virginal Ti_3SiC_2 material, prompting the same material response and hence load-displacement curve. Optical measurements confirm the crack growth beyond the previous healed crack lengths in all tested samples (yet not reported here). An example is shown in Figure 5.9, where the crack has extended through the previously partially healed zone, to propagate further into the virginal material.

5.4. Conclusions

Cracks in both thermally shocked and mechanically fractured Ti_3SiC_2 could be healed by oxidation at 1100, 1200 and 1300 °C. The combination of amorphous SiO_2 and dense TiO_2 (rutile) filled up to 40 % of a 10 mm long and up to 10 µm wide crack after oxidation at 1200 °C for 1 h. Wedge loading of a chevron notched specimen before and after thermal treatment shows that load bearing capacity of the damaged material could be restored partially. Given the imperfect crack filling the actual healing efficiency could not be determined quantitatively.

References

[1] M. W. Barsoum, *The $M_{n+1}AX_n$ phases: A new class of solids; thermodynamically stable nanolaminates,* Progress in Solid State Chemistry **28**, 201 (2000).

[2] W. G. Sloof, R. Pei, S. A. McDonald, J. L. Fife, L. Shen, L. Boatemaa, A.-S. Farle, K. Yan, X. Zhang, S. van der Zwaag, P. D. Lee, and P. J. Withers, *Repeated crack healing in MAX-phase ceramics revealed by 4d in situ synchrotron x-ray tomographic microscopy,* Scientific Reports **6**, 23040 (2016).

[3] G. M. Song, Y. T. Pei, W. G. Sloof, S. B. Li, J. De Hosson, and S. van der Zwaag, *Oxidation-induced crack healing in Ti_3AlC_2 ceramics,* Scripta Materialia **58**, 13 (2008).

[4] S. Li, G. Bei, X. Chen, L. Zhang, Y. Zhou, M. Mačković, E. Spiecker, and P. Greil, *Crack healing induced electrical and mechanical properties recovery in a Ti_2SnC ceramic,* Journal of the European Ceramic Society **36**, 25 (2016).

[5] A.-S. Farle, C. Kwakernaak, S. van der Zwaag, and W. G. Sloof, *A conceptual study into the potential of $M_{n+1}AX_n$-phase ceramics for self-healing of crack damage,* Journal of the European Ceramic Society **35**, 37 (2015).

[6] W. Jeitschko and H. Nowotny, *Die kristallstruktur von Ti_3SiC_2 — ein neuer komplexcarbid-typ,* Monatshefte für Chemie / Chemical Monthly **98**, 329 (1967).

[7] M. W. Barsoum and T. El-Raghy, *Synthesis and characterization of a remarkable ceramic: Ti_3SiC_2,* Journal of the American Ceramic Society **79**, 1953 (1996).

[8] H. Zhang, Y. Bao, and Y. Zhou, *Current status in layered ternary carbide Ti_3SiC_2, a review,* Journal of Materials Sciences and Technology **25**, 1 (2009).

[9] T. El-Raghy, M. W. Barsoum, A. Zavaliangos, and S. R. Kalidindi, *Processing and mechanical properties of Ti_3SiC_2: II, effect of grain size and deformation temperature,* Journal of the American Ceramic Society **82**, 2855 (1999).

[10] Y. Zhu, A. Zhou, Y. Ji, J. Jia, L. Wang, B. Wu, and Q. Zan, *Tribological properties of Ti_3SiC_2 coupled with different counterfaces,* Ceramics International **41**, 6950 (2015).

[11] J. Li and Y. Miyamoto, *Fabrication of monolithic Ti_3SiC_2 ceramic through reactive sintering of Ti/Si/2TiC,* Journal of materials synthesis and processing **7**, 91 (1999).

[12] S. Arunajatesan and A. H. Carim, *Symmetry and crystal structure of Ti_3SiC_2,* Materials Letters **20**, 319 (1994).

[13] S. B. Li, H. X. Zhai, G. P. Bei, Y. Zhou, and Z. L. Zhang, *Formation of Ti_3AlC_2 by mechanically induced self-propagating reaction in Ti-Al-C system at room temperature,* Materials Science and Technology **22**, 667 (2006).

[14] J. Emmerlich, P. Eklund, D. Rittrich, H. Högberg, and L. Hultman, *Electrical resistivity of $Ti_{n+1}AC_n$ (A =Si, Ge, Sn, n = 1–3) thin films,* Journal of Materials Research **22**, 2279 (2007).

[15] M. Radovic, M. Barsoum, A. Ganguly, T. Zhen, P. Finkel, S. Kalidindi, and E. Lara-Curzio, *On the elastic properties and mechanical damping of Ti_3SiC_2, Ti_3GeC_2, $Ti_3Si_{0.5}Al_{0.5}C_2$ and Ti_2AlC in the 300–1573 K temperature range,* Acta Materialia **54**, 2757 (2006).

[16] M. W. Barsoum, *Physical properties of the MAX phases,* in *Encyclopedia of Materials: Science and Technology (Second Edition)*, edited by K. H. J. B. Editors-in Chief: , W. C. Robert, C. F. Merton, I. Bernard, J. K. Edward, M. Subhash, and V. Patrick (Elsevier, Oxford, 2006) pp. 1–11.

[17] A.-S.Farle, L. Boatemaa, L. Shen, S. Gövert, J. B. W. Kok, M. Bosch, S. Yoshioka, S. van der Zwaag, and W. G. Sloof, *Demonstrating the self-healing behaviour of some selected ceramics under combustion chamber conditions,* Smart Materials and Structures **25**, 084019 (2016).

[18] S. Yoshioka, L. Boatemaa, S. van der Zwaag, W. Nakao, and W. G. Sloof, *On the use of TiC as high-temperature healing particles in alumina based composites,* Journal of the European Ceramic Society **36**, 4155 (2016).

[19] M. C. Chu, S. J. Cho, Y. C. Lee, H. M. Park, and D. Y. Yoon, *Crack healing in silicon carbide,* Journal of the American Ceramic Society **87**, 490 (2004).

[20] K. Ando, B. S. Kim, M. C. Chu, S. Saito, and K. Takahashi, *Crack-healing and mechanical behaviour of $Al_2O_{3/}SiC$ composites at elevated temperature,* Fatigue & Fracture of Engineering Materials & Structures **27**, 533 (2004).

[21] K. Takahashi, B.-S. Kim, M.-C. Chu, S. Sato, and K. Ando, *Crack-healing behavior and static fatigue strength of Si_3N_4/SiC ceramics held under stress at temperature (800, 900, 1000 °C),* Journal of the European Ceramic Society **23**, 1971 (2003).

[22] K. Houjou, K. Ando, and K. Takahashi, *Crack-healing behaviour of ZrO_2/SiC composite ceramics,* International Journal of Structural Integrity **1**, 73 (2010).

[23] T. Osada, W. Nakao, K. Takahashi, and K. Ando, *Self-crack-healing behavior in ceramic matrix composites,* in *Advances in Ceramic Matrix Composites*, edited by I. Low (Woodhead Publishing, 2014) pp. 410 – 441.

[24] W. Nakao, Y. Tsutagawa, and K. Ando, *Enhancement of in situ self-crack-healing efficient temperature region by SiC nanosizing,* Journal of Intelligent Material Systems and Structures **19**, 407 (2008).

[25] C. A. Schneider, W. S. Rasband, and K. W. Eliceiri, *NIH Image to ImageJ: 25 years of image analysis,* Nat Meth **9**, 671 (2012).

[26] ASTM B962-15, *Standard Test Methods for Density of Compacted or Sintered Powder Metallurgy (PM) Products Using Archimedes' Principle*, Standard (ASTM International, West Conshohocken, PA, USA, 2015).

[27] M. W. Barsoum, *Oxidation and reactivity with other gases,* in *MAX Phases: Properties of Machinable Ternary Carbides and Nitrides* (Wiley -VCH Verlag GmbH & co. KGaA, 2013) Chap. 6, pp. 187–236, 1st ed.

[28] A.-S. M. Farle, J. Stikkelman, S. van der Zwaag, and W. G. Sloof, *Oxidation and self-healing behaviour of spark plasma sintered Ta_2AlC,* Journal of the European Ceramic Society , (2017).

[29] M. W. Barsoum, T. ElRaghy, and L. U. J. T. Ogbuji, *Oxidation of Ti_3SiC_2 in air,* Journal of The Electrochemical Society **144**, 2508 (1997).

[30] D. B. Lee and S. W. Park, *Oxidation of Ti_3SiC_2 between 900 and 1200 °C in air,* Oxidation of Metals **67**, 51 (2006).

[31] S. Li, L. Cheng, and L. Zhang, *Oxidation behavior of Ti_3SiC_2 at high temperature in air,* Materials Science and Engineering: A **341**, 112 (2003).

[32] D. R. Uhlmann, H. K. Bowen, and W. Kingery, *Introduction to ceramics,* (1976).

[33] Z. Sun, Y. Zhou, and M. Li, *Cyclic-oxidation behavior of Ti_3SiC_2-base material at 1100°C,* Oxidation of Metals **57**, 379 (2002).

[34] W. K. Pang, I. M. Low, B. H. O. Connor, A. J. Studer, V. K. Peterson, Z. M. Sun, and J. P. Palmquist, *Comparison of thermal stability in MAX 211 and 312 phases,* Journal of Physics: Conference Series **251**, 012025 (2010).

[35] M. W. Barsoum and L. Farber, *Room-temperature deintercalation and self-extrusion of Ga from Cr_2GaN,* Science **284**, 937 (1999).

[36] J. Zeng, S. Ren, and J. Lu, *Phase evolution of Ti_3SiC_2 annealing in vacuum at elevated temperatures,* International Journal of Applied Ceramic Technology **10**, 527 (2013).

6

Oxidation and self-healing behavior of spark plasma sintered Ta_2AlC

Reserve your right to think,
for even to think wrongly is better than not to think at all.

Hypatia of Alexandria

This chapter has been published in the Journal of the European Ceramic Society [1]. Authors: Ann-Sophie Farle, Julia Stikkelman, Sybrand van der Zwaag, Willem G. Sloof

Self-healing and oxidation of spark plasma sintered Ta_2AlC was investigated using a newly developed wedge loaded compact specimen to determine strength recovery in a single specimen. Previous work had predicted dominant Al oxidation leading to dense and strong reaction products to result in favorable healing properties. However, crack-gap filling and strength recovery of Ta_2AlC were not achieved by oxidation at 600°*C. Oxidation below* 900°*C in synthetic and atmospheric air resulted in porous Ta-oxides, with no Al_2O_3 formation. Differential thermal analysis up to* 1200°*C revealed a two-step reaction process with the final products Ta_2O_5 and $TaAlO_4$. The study shows that the kinetics may overrule the self-healing MAX-phase design criteria based on thermodynamics.*

6.1. Introduction

$M_{n+1}AX_n$ phases, with n equalling 1, 2, 3, or higher, are composed of transition metals (M), elements from groups 14 and 15 (A) and carbon or nitrogen (X) and belong to the family of metallo-ceramics. The atomic layered structure results in a unique combination of high temperature strength and stability, a high mechanical hardness with a semi-ductile failure mode and high thermal and electrical conductivity. Recently it has been shown that some MAX phases demonstrate high temperature self-healing behavior [2, 3] when exposed to oxygen containing atmospheres. The healing behavior of the self-healing MAX phases, such as Ti_2AlC, Ti_3AlC_2 and Cr_2AlC, is the result of a well-adhering Al_2O_3 layer forming at the two opposing crack faces [4–6]. In-situ time-resolved high-resolution synchrotron 3D X-ray tomography [7] revealed the actual crack filling process with sub-micron resolution. The study demonstrated that the crack closure is not restricted to the crack mouth but proceeds along the crack faces into the depth of the sample. Because of the almost complete filling of the crack with well adhering and dense high strength Al_2O_3 the healing process can lead to a full recovery of 4-point bending strength [4].

Furthermore, the healing process does not rely on the presence of external healing particles, but is a response of the material itself. Healing of a specific crack can take place several times and significant strength recovery even after 6 successive fracturing and healing steps has been demonstrated for Ti_2AlC [8]. Such a multiple healing ability is crucial for the successful introduction of the material in real life engineering components operating at high temperatures and high loads, such as turbine engines. This potential has been demonstrated convincingly even under such harsh conditions [9].

Farle et al. [10] (c.f. Chapter 2) analyzed the relevant parameters and phenomena in the known self-healing MAX phases and defined the following parameters as being crucial for obtaining high temperature oxidative self-healing behavior: formation of a stable oxide upon selective oxidation of the A-element, a relatively high diffusivity of the A-element to ensure fast oxidation, a sufficient volume expansion to fill a crack gap and a good adhesion of the oxide product to the matrix, as well as comparable coefficients of thermal expansion (CTE) and Young's Moduli of the healing product to those of the parent MAX phase. In these design rules, kinetic aspects were not taken into account.

Applying these criteria to the 79 known MAX phases returned the known self-healing grades (Ti_2AlC, Ti_3AlC_2 and Cr_2AlC) but also identified Ta_2AlC as a potential self-healing MAX phase. The analysis showed that Al_2O_3 over Ta_2O_5 should form, in which case there is a substantial volume increase, good adhesion and matching Young's Modulus and coefficient of thermal expansion. Earlier oxidation studies of Ta_2AlC have shown the formation of protective oxide layers is restricted to a narrow temperature window up to 600°C [11].

The current study aimed to check and quantify the healing ability of spark plasma sintered Ta_2AlC and the underlying oxidation mechanisms. A newly-developed wedge loaded chevron notched specimen configuration (Chapter 3) was used to measure strength recovery after 16 hours of oxidation in air. By inducing a path-controlled crack in a brittle material, self-healing strength recovery could be measured in a single sample, effectively reducing material consumption. To explain the absence of self-healing, oxide morphology, reaction energies and oxidation behavior were assessed by thermal gravimetric and

differential analysis over a wider temperature regime.

6.2. Experimental

Samples were prepared by spark plasma sintering (SPS) of Ta (> 99.9%, < 100 µm, ChemPur, Germany), Al (99.8 %, 45 µm, TLS Technik GmbH & Co, Germany) and graphite (> 99.5 %, 6 µm, Graphit Kropfmuhl AG, Germany) powders in the molar ratio of 2:1.2:1. The starting powders were mixed for 12 h in a Turbula T2C Mixer (Willy A. Bachofen, Switzerland) using 5 mm ZrO_2 balls in a ratio of 10:1. Sintering was carried out in a spark plasma sintering furnace (Type HP D 25, FCT-Systeme GmbH, Germany) using graphite molds of 20 and 40 mm diameter to create samples of approx. 5 mm thickness. The heating rate to the peak temperature of 1400°C was 50 °C min^{-1}. The subsequent cooling rate was 100 °C min^{-1}. A pressure of 50 MPa was applied after heating to 700°C and during sintering. To counteract the effects of Al loss while sintering at high temperatures, Al was taken to be over-stoichiometric in the initial mixture. Furthermore, pressureless heating up to 700°C was applied to allow formation of solid intermetallics such as Ta_5Al_3 and prevent squeezing out of liquid aluminum formed around 660°C.

In addition to the SPS experiments attempts were made to synthesize Ta_2AlC via pressureless sintering, however these did not yield pure MAX-phase powders, even when using the same composition and temperatures successfully employed during spark plasma sintering.

Self-healing of ceramics and MAX phases is commonly tested by four- or three-point bending, resulting by definition in a relatively high material consumption [12], as monitoring of strength recovery in an individual fractured sample is impossible. To track the oxidation induced strength recovery of Ta_2AlC in the same sample, a modified chevron notched compact specimen was used.

Details of the test and subsequent data analysis to extract reliable fracture data can be found elsewhere, c.f. Chapter 3. A 10° quenched and tempered steel wedge was used for load application to create a crack along a designated path in a 24 x 25 mm sample with a rounded bottom and a chevron notch. Tests were performed using a 100 kN electromechanical load frame (Instron, type 5500R) which was fitted with a 10 kN load cell. Wedge displacement was stopped upon a specified (50 %) load drop to arrest the crack before full fracture of the sample. Tests were carried out under closed loop displacement control, with a fixed crosshead displacement rate of 0.1 mm s^{-1}. The crack length was determined ex-situ by optical microscopy using a digital microscope (Keyence VHX-100, Osaka, Japan) and scanning electron microscopy (see below).

Cracks were healed ex-situ at 600°C for 16 h in atmospheric air using an alumina tube furnace (LTF 16/75/610, Lenton, UK) before the wedge loading test was repeated under the conditions of the first loading. The healing temperature was based on observations by Gupta et al. [11].

For microstructural analysis all samples were ground and polished using SiC abrasive paper up to 2500 grit and diamond paste up to 0.25 µm. Quantitative compositional analysis of the synthesised MAX phase as well as the oxidation products was carried out by electron probe X-ray micro analysis (EPMA) using a JXA-8900R superprobe (JEOL Ltd., Tokyo, Japan) equipped with wave dispersive spectroscopy (WDS). Measurements were performed on carbon coated samples using an electron beam with 10 keV energy

and a beam current of 50 nA. Decontamination of measurement spots was achieved using an air-jet. The composition at each analysis location of the sample was determined using the X-ray intensities of the constituent elements after background correction relative to the corresponding intensities of reference materials. The thus obtained intensity ratios were processed with a matrix correction program CITZAF [13].

Furthermore, oxide morphology, scale thickness and homogeneity were investigated by scanning electron microscopy using a JSM 6500F microscope (JEOL Ltd., Tokyo, Japan). This microscope is equipped with an energy dispersive x-ray spectrometer (EDS) (ThermoFisher UltraDry 30 mm2 detector) for X-ray microanalysis (XMA). Data acquisition and analysis was carried out with Noran System Seven software package (Thermo Electron Scientific Instruments LLC., USA).

Isothermal oxidation kinetics were investigated by thermal gravimetric analysis (TGA) using a high performance symmetrical TGA system (TAG 16/18, Setaram Instrumentation, Caluire, France) to eliminate buoyancy effects. Bulk samples (3 x 4.5 x 12.5 mm), suspended from sapphire rods, were oxidized for 10 h at 600, 700 and 800°C in a flow of dry artificial air composed of 40 sccm N_2 (purity > 5N) and 10 sccm O_2 (purity > 5N). Prior to oxidation all samples were manually ground with SiC paper of increasing fineness up to 2500 grit and cleaned in acetone. Heating and cooling of all samples was conducted in Ar (purity > 5N, 50 sccm) atmosphere.

Necessary machining for TGA and the modified chevron notched compact specimen was carried out by electronic discharge machining (EDM) with wire diameters of 0.25 and 0.1 mm.

Differential thermal analysis (DTA) was performed using a SETSYS Evolution 1750 (Setaram, Caluire, France) coupled with mass spectrometry (OmniStarTM, GSD 301 O, Pfeiffer Vacuum, Asslar, Germany) to detect CO_2 evolution. Powdered samples of Ta_2AlC were heated to 1200°C with different heating rates (1, 2, 5, 10, 15 $°C\,min^{-1}$) in a flow of pure dry synthetic air, i.e. 40 sccm N_2 (purity > 5N) and 10 sccm of O_2 (purity > 5N). The recorded data was corrected for buoyancy effects by subtraction of a blank measurement performed under the same conditions. Weight gain was normalized to a range of 0 to 1, corresponding to the maximum weight gain of 6.7 mg. Powders were obtained by pulverizing dense bulk SPS samples using a variable speed rotary tool (Dremel 395, Dremel, USA) with a clean diamond tip. The resulting powder was characterized by SEM and laser diffraction particle size analysis (Mastersizer X, Malvern Instruments, UK). The average powder size was 2-10 µm.

The DTA results were analysed using the so called Kissinger-Sunose-Akahira equation [14]:

$$\ln\left(\frac{\beta}{T_p^2}\right) + \frac{E_A}{RT_p} = \text{constant} \tag{6.1}$$

where E_A is the activation energy, R is the gas constant, T_p the peak temperature and β the heating rate. The slope of the straight line fitted to the data points for $\ln\left(\frac{\beta}{T_p^2}\right)$ versus $\left(\frac{1}{T_p^2}\right)$ yields the activation energy of the reaction.

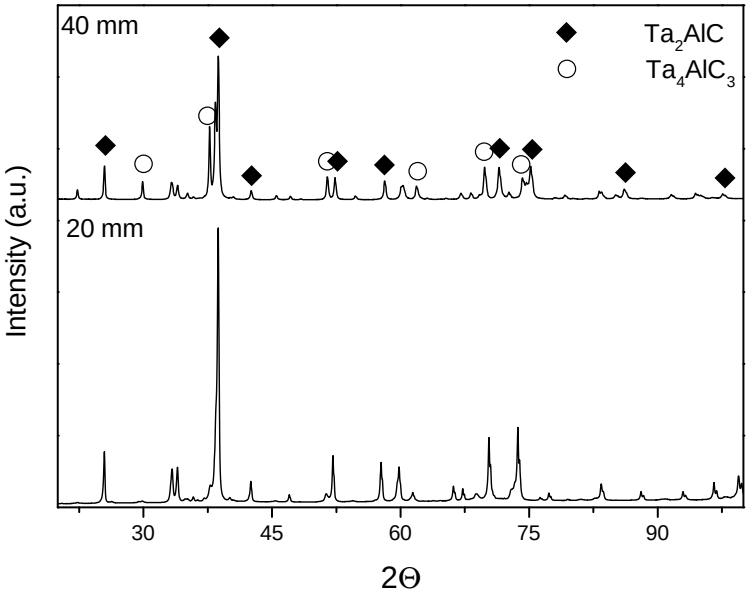

Figure 6.1: XRD patterns of spark plasma sintered Ta_2AlC with varying Ta_4AlC_3 content for two samples sizes.

6.3. Results and Discussion

For the optimal SPS conditions, listed above, homogeneous, dense material, free of internal defects was obtained. The same synthesis procedure employed for all samples resulted in compositional variations between the samples of different sizes. Figure 6.1 shows two XRD patterns, of a 20 mm and a 40 mm diameter sample. Both contain Ta_4AlC_3, another MAX-phase configuration as a second phase, whereby 20 mm samples contain approx. 10% and the larger samples up to 50%. The 40 mm samples were used for crack healing tests and the 20 mm samples for TGA and DTA.

The difference in mold size did not affect the microstructure of the samples. Elongated grains of 20 to 40 µm in length, with completely random orientation, were identified in all samples. Load-displacement curves of the wedge loaded specimen, recorded before and after oxidation showed a large difference in the slope during initial loading, see Figure 6.2. This is attributed to a change in the friction coefficient between the wedge and sample upon oxidation (c.f. Chapter 3). Furthermore, softening of the material seemed to occur.

Wedge loading of the chevron notched compact specimen led to stable crack growth and a peak load of 225 N for the virgin material. After the load dropped to 157 N the wedge was retracted and the samples were examined, revealing a crack with the length of 8.3 mm and a width of up to 5 µm, approx. 55% of the available sample length. The crack morphology was as that commonly observed in MAX phase materials [4].

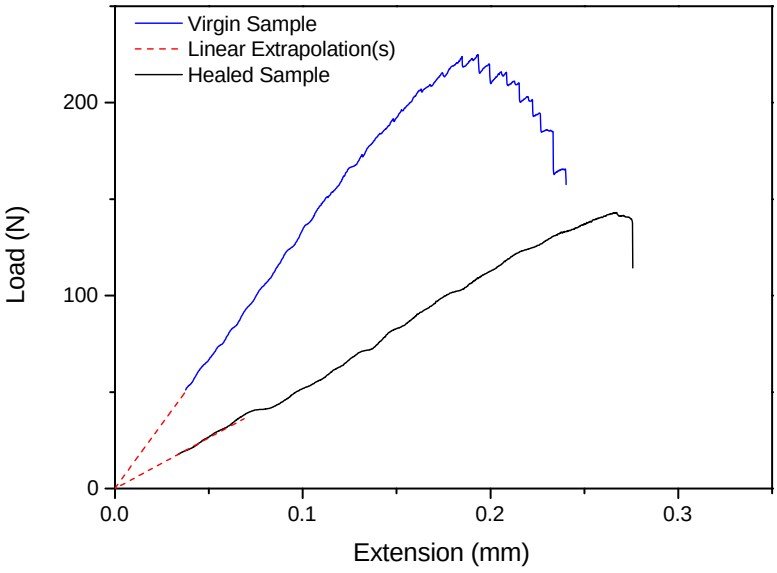

Figure 6.2: Load versus displacement curves of wedge loaded chevron notched Ta_2AlC specimen before and after isothermal oxidation at 600°C for 16 h in air. Samples were pre-loaded to approx. 20 and 55 N, thus both curves were extrapolated for better comparison.

Loading of the sample healed at 600°C for 16 h was resumed. However, the maximum load did not exceed 143 N, which is below the residual load-bearing capacity of the virgin material, see Figure 6.2. Hence, no strength recovery was achieved by oxidation at 600°C for 16 hours.

SEM images of an oxidized specimen before re-cracking show an oxidized zone of approx. 60 µm thickness on both crack surfaces after 16 h at 600°C. The crack gap is flanked by porous Ta-oxide on top of the original matrix material. As can be seen in Figure 6.3, convergence of the crack walls could not be detected. Figure 6.3b shows the oxidation proceeding along the grain boundaries, enveloping areas of virginal material. Furthermore, the oxidation progresses exclusively inward from the fracture surfaces.

The absence of Al_2O_3 and thus strength recovery, supports the necessity for further oxidation studies. Supplementary thermogravimetric analysis of bulk Ta_2AlC at 600, 700 and 800°C for 10 h supports the observations of the wedge intrusion test. 10 h of oxidation at 600°C did not result in a porous or pronounced oxide layer, however oxidation at 700 and 800°C similar morphology to the sample treated at 600°C for 16 h. Figure 6.4 shows the weight gain of bulk Ta_2AlC for oxidation at different temperatures for 10 h. Isothermal oxidation of bulk Ta_2AlC with some Ta_4AlC_3 (cf. Figure 6.1) revealed nearly linear oxidation kinetics at all tested temperatures, i.e. 600, 700 and 800°C.

XRD could not detect any oxide formed at 600°C after 10 h. SEM and SEM-XMA how-

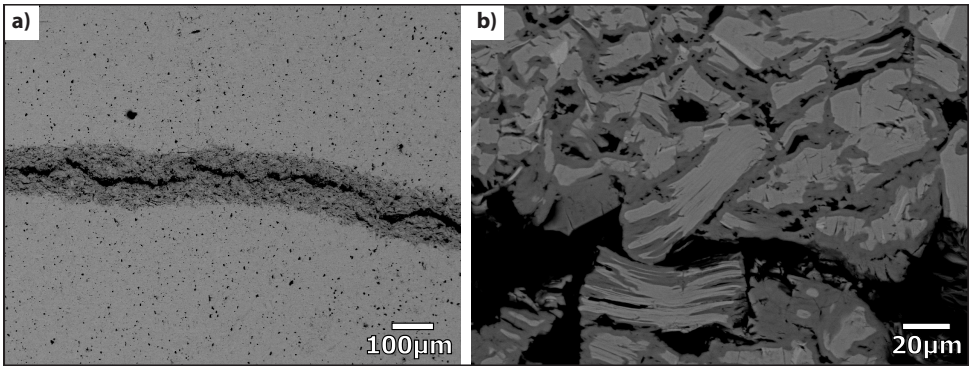

Figure 6.3: Backscattered electron image of Ta_2AlC oxide after 16 h of oxidation at 600°C.

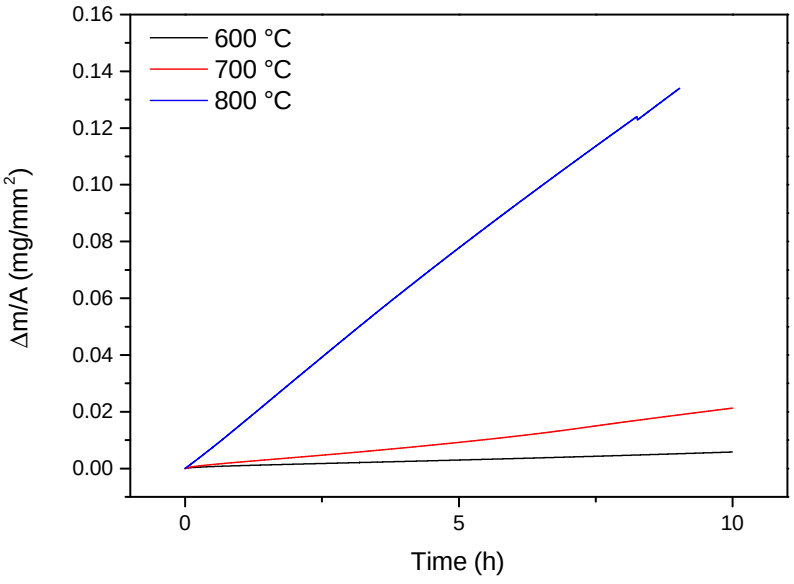

Figure 6.4: Weight gain of Ta_2AlC at 600, 700 and 900°C for 10 h.

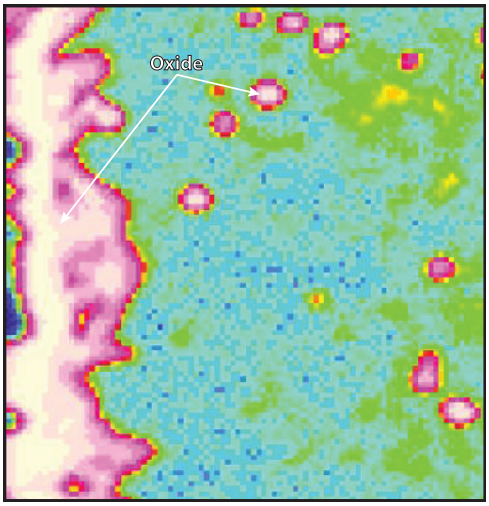

Figure 6.5: Qualitative EPMA map of oxygen in Ta_2AlC oxidized at 600°C for 10 h.

ever show a 2-5 µm thick oxygen enriched Ta-Al layer with atom ratios of Ta:Al:O = 2.5 : 1 : 6. Qualitative EPMA measurements display an up to 6 µm thick oxygen enriched area; see Figure 6.5.

SEM and EPMA show areas of original MAX phase composition within the oxidized region after oxidation at 700 °C, see Figure 6.6b. Comparable morphology can be seen after isothermal oxidation at 800 °C, where the porous oxide layer has increased up to 250 µm in thickness, but no longer contains original MAX phase material (Figure 6.6c). The oxide developed after 10 h of oxidation at 800 °C is composed of TaO, $TaO_{1,67}$ and Ta_2O_5, as determined by XRD analysis. In contrast to the predictions based on postulated criteria [10] no Al based oxides were identified.

Sufficient volume expansion upon oxidation of Al was a design criterion for effective self-healing of Ta_2AlC [10]. However, the formation of Ta-oxides leads to highly porous and cracked oxides due to the large volume expansion upon oxidation of Ta_2AlC to Ta_2O_5, and possibly $TaAlO_4$. The relative volume expansion upon oxidation (RVE) [10] was determined for two cases: i.e. the conversion of MAX phase into Ta_2O_5 only, and conversion of MAX phase into Ta_2O_5 and the maximum possible amount of $TaAlO_4$, based on stoichiometry (see Eqs (2) and (3)). All values calculated lie above 1.5, viz.: 1.55 and 2.0 for the full or combined oxidation of Ta_2AlC, and 1.77 and 2.02 for Ta_4AlC_3.

$$\mathrm{RVE} = \frac{V_{Ta_2O_5}}{V_{Ta_xAlC_y}} \tag{6.2}$$

$$\mathrm{RVE} = \frac{xV_{Ta_2O_5} + 2V_{TaAlO_4}}{2V_{Ta_xAlC_y}} \tag{6.3}$$

The high RVE corresponds well with the observed microstructure of the oxide scales on TGA samples after isothermal oxidation at 700 and 800 °C. Furthermore, cracks in

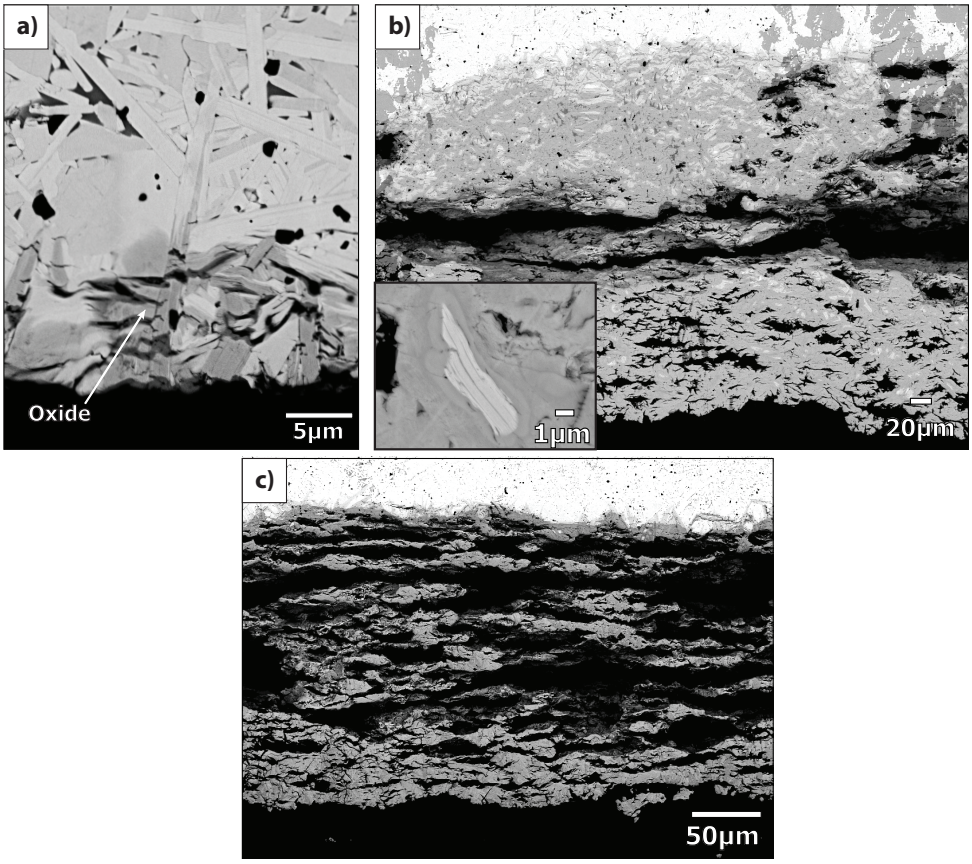

Figure 6.6: SEM images of oxide scales after 10 hours of isothermal oxidation of Ta_2AlC in artificial air at a) 600, b) 700 and c) 800°C

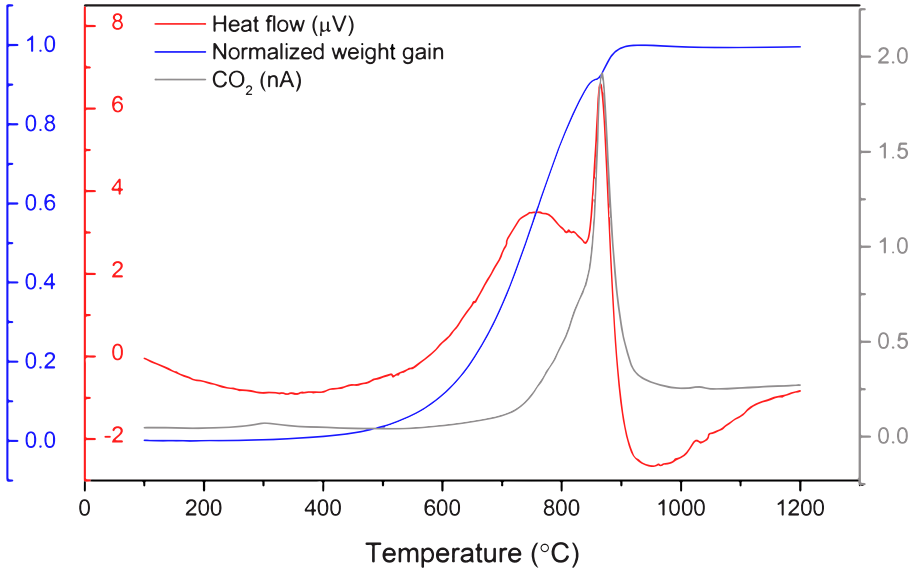

Figure 6.7: Heat flow, mass gain (TG) and CO_2 signal of Ta_2AlC powder heated up to 1200 °C with 5 °C min^{-1}.

the oxides could be a result of the thermal mismatch between Ta-oxides and the MAX phase, i.e. the CTE of Ta_2O_5 is reported to be between 2.9 and 4.0 x 10^{-6} K^{-1} while the measured dilatometric thermal expansion coefficient (TEC) of Ta_2AlC is 6.0 x 10^{-6} K^{-1} [11, 15]. With the exception of no solid Al_2O_3 layer, all criteria for self-healing are met. The absence of the healing effect due to porous Ta-oxides must be due to kinetics.

According to the DTA measurements shown in Figure 6.7 the oxidation of Ta_2AlC proceeds in a two-step process. For a heating rate of 5 °C min^{-1} the first reaction peaks at approx. 760 °C. Powders retrieved at 800 °C show that the MAX phase has partially oxidized into $TaO_{1.1}$ and $Ta_{1.86}Al_{0.14}O_{4.86}$. The unreacted carbon remains in Ta_4C_3 and Ta_2AlC.

The second exothermal peak is attributed to the oxidation of Carbon from Ta_4C_3 and/or Ta_2AlC to CO_2. Powders retrieved after heating up to 1200 °C show full conversion to Ta_2O_5 and $TaAlO_4$. The conversion from the initial oxides $TaO_{1.1}$, $Ta_{1.86}Al_{0.14}O_{4.86}$ and the remaining Ta_4C_3 and Ta_2AlC to Ta_2O_5 and $TaAlO_4$ takes place at approx. 850 °C under loss of C to form CO_2, see Figure 6.7. Mass spectrometry revealed the reaction of carbon to CO_2 during oxidation, confirming a long standing assumption for MAX-phase oxidation [16].

The formation of Al containing oxides such as $Ta_{1.86}Al_{0.14}O_{4.86}$ and $TaAlO_4$ was not observed for bulk oxidation (TGA) at 600, 700 or 800 °C.

The activation energy (Ea) of the initial decomposition reaction of Ta_2AlC into $TaO_{1.1}$ and $Ta_{1.86}Al_{0.14}O_{4.86}$ was calculated using the Kissinger-Sunose-Akahira equation [14], relating the peak temperatures of reactions measured for different heating rates to their activation energy, see Figure 6.8. This resulted in a value for the activation energy of

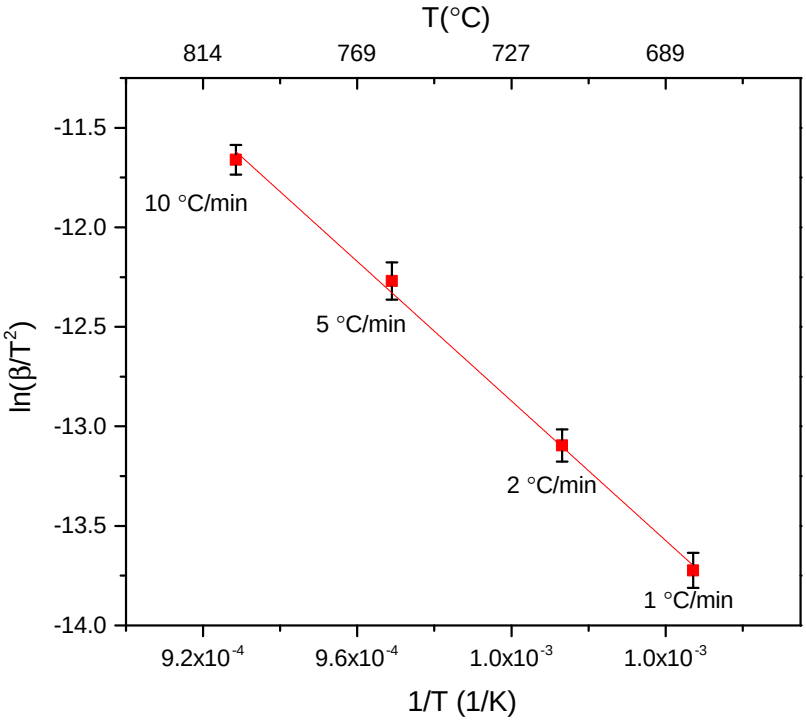

Figure 6.8: Kissinger points and linear fit of 1st reaction from DTA data on Ta_2AlC heated with 1, 2, 5 and 10 °C min^{-1}.

146 ± 10 kJ mol^{-1}. Though data should be treated with care, because activation energies calculated by method of Kissinger-analysis based on DTA data are only valid for simple decomposition reactions, regardless the order of the reaction [14].

The activation energy can now be compared with those of other related materials. The activation energy of 146 ± 10 kJ mol^{-1}, required for oxidation of Ta_2AlC lies below that of Ti_2AlC, Ti_3SiC_2, Ta and TaC, viz.: 363 [9], 325 [6], 183 ± 8 [17] and 379 ± 16 kJ mol^{-1} [18], respectively. It is most comparable to that of Ta_2C with 129 ± 7 kJ mol^{-1} [18].

The similarity in activation energy and oxide morphology [18] of Ta_2AlC and Ta_2C oxidation emphasizes that Al does not substantially contribute to the oxidation reaction. Tantalum oxide formation is dominant, possibly also due to its abundance and higher activity in Ta_2AlC or Ta_4AlC_3 than Al.

Finally, thermodynamic data can be considered insufficient for oxide prediction without supportive kinetic data. Previous work had assumed the internal diffusion of the A-element towards the oxidation front or crack gap would be a critical factor for competitive oxide growth, especially in self-healing compounds [10]. However, initial oxidation of all constituents should be considered and the consequential oxidation limited by oxygen diffusivity and M- and A-element mobility should be among the determining factors

for final oxide prediction. The authors recommend an inclusion of diffusion data, viz.: A in M-oxides, and especially the oxygen transport.

6.4. Conclusions

Self-healing of Ta_2AlC by means of a wedge loaded specimen and thermal treatment at 600 °C did not result in strength recovery. Oxidation studies showed Ta-oxide formation with an activation energy of $146 \pm 10\,kJ\,mol^{-1}$, resulting in highly porous oxide scales. The thermodynamically predicted Al_2O_3 formation was not observed at temperatures up 1200 °C. The study provides proof that kinetic data should be added to the list of design criteria for self-healing MAX phases.

References

[1] A.-S. M. Farle, J. Stikkelman, S. van der Zwaag, and W. G. Sloof, *Oxidation and self-healing behaviour of spark plasma sintered Ta_2AlC,* Journal of the European Ceramic Society , (2017).

[2] M. W. Barsoum, *The $M_{n+1}AX_n$ phases: A new class of solids; thermodynamically stable nanolaminates,* Progress in Solid State Chemistry **28**, 201 (2000).

[3] W. Sloof, A.-S. Farle, and L. Shen, *Intrinsic autonomous crack healing in MAX phase ceramics,* in *Self healing materials - pioneering research in the Netherlands*, edited by S. van der Zwaag and E. Brinkman (IOP Press, Amsterdam, The Netherlands, 2015) pp. 115–123.

[4] G. M. Song, Y. T. Pei, W. G. Sloof, S. B. Li, J. De Hosson, and S. van der Zwaag, *Oxidation-induced crack healing in Ti_3AlC_2 ceramics,* Scripta Materialia **58**, 13 (2008).

[5] R. Pei, S. McDonald, L. Shen, S. van der Zwaag, W. Sloof, P. Withers, and P. Mummery, *Crack healing behaviour of Cr_2AlC MAX phase studied by x-ray tomography,* Journal of the European Ceramic Society , 441–450 (2016).

[6] S. Li, L. Cheng, and L. Zhang, *Oxidation behavior of Ti_3SiC_2 at high temperature in air,* Materials Science and Engineering: A **341**, 112 (2003).

[7] W. G. Sloof, R. Pei, S. A. McDonald, J. L. Fife, L. Shen, L. Boatemaa, A.-S. Farle, K. Yan, X. Zhang, S. van der Zwaag, P. D. Lee, and P. J. Withers, *Repeated crack healing in MAX-phase ceramics revealed by 4d in situ synchrotron x-ray tomographic microscopy,* Scientific Reports **6**, 23040 (2016).

[8] S. Li, G. Song, K. Kwakernaak, S. van der Zwaag, and W. G. Sloof, *Multiple crack healing of a Ti_2AlC ceramic,* Journal of the European Ceramic Society **32**, 1813 (2012).

[9] A.-S.Farle, L. Boatemaa, L. Shen, S. Gövert, J. B. W. Kok, M. Bosch, S. Yoshioka, S. van der Zwaag, and W. G. Sloof, *Demonstrating the self-healing behaviour of some selected ceramics under combustion chamber conditions,* Smart Materials and Structures **25**, 084019 (2016).

[10] A.-S. Farle, C. Kwakernaak, S. van der Zwaag, and W. G. Sloof, *A conceptual study into the potential of $M_{n+1}AX_n$-phase ceramics for self-healing of crack damage,* Journal of the European Ceramic Society **35**, 37 (2015).

[11] S. Gupta, D. Filimonov, and M. W. Barsoum, *Isothermal oxidation of Ta_2AlC in air,* Journal of the American Ceramic Society **89**, 2974 (2006).

[12] ASTM C1421 - 16, *Standard Test Methods for Determination of Fracture Toughness of Advanced Ceramics at Ambient Temperature*, Standard (ASTM International, West Conshohocken, PA, USA, 2016).

[13] J. T. Armstrong, *Quantitative elemental analysis of individual microparticles with electron beam instruments,* in *Electron probe quantitation* (Springer, 1991) pp. 261–315.

[14] H. E. Kissinger, *Variation of peak temperature with heating rate in differential thermal analysis,* Journal of Research of the National Bureau of Standards **57**, 217 (1956).

[15] Y. Touloukian, R. Kirby, R. Taylor, and T. Lee, *Thermal expansion-nonmetallic solids, the TRPC data series, vol. 13,* (1977).

[16] M. W. Barsoum, *MAX Phases: Properties of Machinable Ternary Carbides and Nitrides* (Wiley-VCH, 2013).

[17] A. Beck, M. Heine, E. Caule, and M. Pryor, *The kinetics of the oxidation of Al in oxygen at high temperature,* Corrosion Science **7**, 1IN111 (1967).

[18] M. Desmaison-Brut, N. Alexandre, and J. Desmaison, *Comparison of the oxidation behaviour of two dense hot isostatically pressed tantalum carbide (TaC and Ta_2C) materials,* Journal of the European Ceramic Society **17**, 1325 (1997).

7

Demonstrating the self-healing behavior of some selected ceramics under combustion chamber conditions

Science and everyday life cannot and should not be separated.

Rosalind Franklin

This chapter has been published in Smart Materials and Structures **25**,(2016) [1]. Authors: Ann-Sophie Farle, Linda Boatemaa, Lu Shen, Simon Gövert, Jim B. W. Kok, Myrthe Bosch, Shunsuke Yoshioka, Sybrand van der Zwaag, Willem G. Sloof

Closure of surface cracks by self-healing of conventional and MAX Phase ceramics under realistic turbulent combustion chamber conditions is presented. Three ceramics namely; Al_2O_3*,* Ti_2AlC *and* Cr_2AlC *are investigated. Healing was achieved in* Al_2O_3 *by even dispersion of TiC particles throughout the matrix as the MAX phases,* Ti_2AlC *and* Cr_2AlC *exhibit intrinsic self-healing. Fully dense samples (> 95 %) were sintered by spark plasma sintering and damage was introduced by indentation, quenching and low perpendicular velocity impact methods. The samples were exposed to the oxidizing atmosphere in the post flame zone of a turbulent flame in a combustion chamber to heal at temperatures of approx.* 1000 °C *at low* pO_2 *levels for* 4 h*. Full crack-gap closure was observed for cracks up to* 20 mm *in length and more than* 10 µm *in width. The reaction products (healing agents) were analyzed by SEM, XMA and XRD. A semi-quantification of the healing showed that cracks in* Al_2O_3*/TiC composite (width* 1 µm *and length* 100 µm*) were fully filled with* TiO_2*. In* Ti_2AlC *large cracks were fully filled with a mixture of* TiO_2 *and* Al_2O_3*. And in the* Cr_2AlC*, cracks of up to* 1.0 µm *in width and more than* 100 µm *in length were also completely filled with* Al_2O_3*.*

7.1. Introduction

In recent years the possibility to oxidatively heal surface cracks in high temperature ceramics and metallo-ceramics and to restore mechanical strength at least once has been demonstrated in quite a number of laboratory studies [2–4]. In these laboratory studies relatively high oxygen potentials (comparable to those in heated air) and stagnant air were imposed and the samples were not exposed to any mechanical vibration during the healing treatment. These conditions differ significantly from the prevailing conditions (low partial pressure, very high gas flow velocities and extensive mechanical vibrations) in combustion chambers, where such self-healing ceramics are supposed to be used [5]. The work presented here describes the self-healing behavior of three grades of self-healing ceramics under realistic combustion chamber conditions. The materials to be tested are an extrinsic self-healing system (alumina containing TiC particles as healing agent) and two intrinsic self-healing metallo-ceramics (Cr_2AlC and Ti_2AlC), for which attractive self-healing behavior under laboratory conditions had been demonstrated previously.

The early research on self-healing high temperature ceramics focussed on so-called extrinsic self-healing concepts, in which the crack filling reaction is due to the presences of discrete reactive particles homogeneously distributed in an inert ceramic matrix [5–7]. When a crack is formed in the matrix, the reactive particles in the path of the crack are dissected and oxygen from the environment flowing through the crack can react with the healing particle. In case the reaction product has a larger specific volume than the original particle the excess volume can fill the crack and restore mechanical contact between both opposing crack faces. In case the reaction product adheres relatively well to the matrix material, the filling of the crack not only leads to its sealing but also to the restoration of the tensile strength of the once broken sample. The early work focused on the use of SiC particles or fibres to heal Si_3N_4, mullite and alumina matrices [6, 8, 9] as SiC has a desirable oxidation behavior leading to the formation of SiO_2 which has a good bond strength to many ceramic matrices. By using SiC particles with a size of about 0.3 µm the bending strength of Si_3N_4/SiC composites could be recovered more or less completely by healing between 900-1400 °C for 1 h in air. For the optimum healing temperature of 1300 °C the specimen fractured even outside the healed zone [6]. Similarly, surface cracks of diameter 100-200 µm in mullite were completely healed after heat treatment at 1300 °C for 1 h in air. The crack-healed zone even had a bending strength 150 ± 30 MPa higher than that of the as received material [8].

The optimal volume fraction of granular healing particles was found to be between 15 and 30 % [10–12]. In recent work it has been shown that SiC whiskers rather than granular SiC particles can improve the healing capabilities even further [9] and restore not only strength but also fracture toughness. It was shown that surface cracks with a length of 100 µm could be healed in a composite containing 20 vol. % of 30-100 µm long SiC whiskers. The fracture toughness increased from 3-4 MPa/$\sqrt{m}$ for monolithic alumina to 5.6 MPa/$\sqrt{m}$, and it was reported that the average bending strength after healing is 970 MPa as compared to 1000 MPa for the virginal material. Since then, systematic studies have been done on the effect of crack healing conditions on the mechanical behavior of the crack healed zone [5, 13] the maximum crack size which can completely be healed [14] and the crack healing behavior under static or cyclic loading and crack

healing potential [6, 15].

While SiC additions work rather well, the temperature to induce optimal healing is rather high (1300 °C) and there is a need for lower healing temperatures. TiC has recently been identified and an attractive alternative [16]. The potential of TiC in healing alumina was assessed based on detailed theoretical analysis of the healing reaction and the intrinsic properties of the reaction products TiO_2 (rutile). A systematic analysis of its thermodynamic stability, relative volume expansion, work of adhesion between the healing agent and the matrix, and a comparison of the coefficient of thermal expansion between the matrix and the healing oxide revealed TiC is indeed a potentially attractive healing particle for extrinsic self-healing ceramic systems. Experimentally this was proven when surface cracks of length 100 µm in Al_2O_3-TiC composites containing 30 vol.% TiC particles showed complete tensile strength recovery by annealing for 1 h at 800 °C in air.

The alternative approach to extrinsic self-healing systems in which the healing reaction is due to the intentional addition of a sacrificial phase is that of intrinsic self-healing systems in which the material itself can locally undergo healing reactions. In 2008 metallo-ceramic MAX phases, in particular Ti_3AlC_2, were shown to demonstrate significant self-healing when exposed to high temperatures in oxygen containing atmospheres [4, 17]. The underlying mechanism in the healing reaction is the selective oxidation of the A element in the MAX phases, such as Ti_3AlC_2 and Ti_2AlC as well as Cr_2AlC [17–19]. Cracks in Ti_2AlC MAX phase ceramics of up to some millimetres in length and about 5 µm in width can be healed by oxidation at 1100 °C in air within 2 h [2, 4] leading to full strength recovery. Also cracks running along the same path as previously healed cracks can be restored several times [4][17]. The healing is due to the extensive formation of Al_2O_3 in the crack with minor amounts of the weaker TiO_2 phase. Cr_2AlC MAX phase also shows good self-healing behavior but the reaction rates are a bit slower. Yet the guaranteed absence of the weak TiO_2 in the healed cracks may lead to higher strength values for the healed material [20]. Hence Ti_2AlC and Cr_2AlC were selected for testing under combustion chamber conditions as both materials meet all requirements postulated for successful healing of crack damage [21], e.g. preferential oxidation and fast diffusion of the A-element, volume expansion upon oxidation and adhesion of the healing product to the matrix. As earlier studies [19, 22] on the MAX phase materials have shown that the healing kinetics and the mode of filling of the cracks depends on the grain size, Cr_2AlC samples were produced having two different average grain sizes. The influence of commonly present impurities, such as TiC and Ti_xAl_y in Ti_2AlC are considered by producing MAX phases of different purity grades.

Apart from their self-healing potential MAX phases have interesting mechanical and physical properties, which make them interesting materials for combustion chambers: They are stable up to high temperatures and corrosion resistant [2–4, 23]. Their high thermal conductivity makes them thermal shock resistant [24] and their static strength is maintained up to high temperatures, above which creep will become the limiting factor [25, 26].

In the present work we will demonstrate the self-healing behavior of three promising self-healing ceramics (alumina with TiC as healing agent, phase pure and impure Ti_2AlC and fine and coarse grained Cr_2AlC) under real combustion chamber conditions. First the synthesis of these ceramics will be outlined. Then their micro structure and

Table 7.1: Starting powders for synthesis and sintering.

Powder	Purity (%)	Particle size (μm)	Supplier
Al_2O_3	≥99.99	0.2	Sumitomo Chemicals, Japan
TiC	98	4.5	Alfa Aesar, UK
Ti	>99.5	100	TLS Technik GmbH & Co., Germany
Al	99.8	45	TLS Technik GmbH & Co., Germany
Cr	99.2	100	TLS Technik GmbH & Co., Germany
C (Graphite)	>99.5	6	Graphit Kropfmühl AG, Germany

oxidation behavior will be discussed. Next, different methods to create crack damage are presented. Finally, the results of testing the self-healing ceramics with crack damage under real combustion conditions are evaluated.

7.2. Materials and Methods

7.2.1. Synthesis

Discs of the self-healing ceramics Al_2O_3/TiC, Ti_2AlC and Cr_2AlC with a diameter of 20 mm and a thickness of about 5 mm were prepared by spark plasma sintering (SPS). The powders used to sinter the materials are listed in Table 7.1. These powders were mixed with molar ratios specified in Table 7.2 using a Turbula T2C Mixer (Willy A. Bachofen, Switzerland), for 24 to 48 hours using 5 mm alumina balls. The ball to powder weight ratio was about 3:1. The powder mixtures for Ti_2AlC and Al_2O_3/TiC were sintered directly in the SPS furnace (HP D 25 SD, FCT Systeme GmbH, Germany) using a graphite mould with an inner diameter of 20 mm under Argon atmosphere or in vacuum.

The Al_2O_3/TiC composite was sintered at 1500 °C in Ar and cooled naturally to avoid cracking due to thermal shock. Ti_2AlC samples were directly synthesized by spark plasma sintering using the settings specified in Table 7.2 and a heating rate of 80 °C min^{-1}. The experiments were performed in vacuum. Cr_2AlC was prepared by a two-step sintering process described elsewhere [28]. The coarse grained material was densified directly from pulverized pressureless sintered powder and fine grained sample was sintered from ball milled powders, details can be found in Table 7.2.

Finally the surfaces of the sample were ground using emery paper up to grit 4000, ultrasonically cleaned in ethanol and dried by blowing with pure and dry nitrogen gas.

7.2.2. Characterisation

The density of the sintered materials was measured with the Archimedes method using an analytical balance (Mettler Toledo AG-204, Switzerland) according to ASTM B 3962-15

Table 7.2: Powder composition and sintering conditions for preparing the self-healing ceramics.

Sample	Powder			Ratio	Temperature (°C)	Pressure (MPa)	Duration (min)
Al_2O_3/TiC	Al_2O_3	TiC		0.8:0.2 mass% Al_2O_3:TiC	1500	30	10
Ti_2AlC-P	Ti	Al	TiC	0.85:1.05:1.15	1400	50	30
Ti_2AlC-LP	Ti	Al	TiC	0.85:1.05:1.15	1400	50	60
Cr_2AlC-FG Cr_2AlC-CG	Cr	Al	C	2:1.15:1	1250	50	60

[27]. The Vickers hardness was determined by averaging the results from 10 50 N indents using a hardness tester (Zwick/Z2.5, Germany). The indents were created by loading the indenter with 5 N s^{-1} and a holding time of 20 s.

The Al_2O_3/TiC composite was characterized using the X-ray diffractometer with a Lynxeye position sensitive detector and Cu Kα radiation. The phase purity of the MAX-phase samples was determined via X-ray diffraction using a Bruker D8 Advance diffractometer (Bruker, Germany) in the Bragg-Brentano geometry with graphite monochromator and Co and Cu Kα radiation. The recorded X-ray diffractrograms were processed with Bruker software Diffrac.EVA 4.1 software.

Micro structure, crack morphology and crack filling were investigated using a scanning electron microscope (SEM), type JSM 6500F (JEOL Ltd., Tokyo, Japan) equipped with an energy dispersive spectrometer (EDS, type: ThermoFisher UltraDry 30 mm^2 detector) for X-ray microanalysis (XMA) and with Noran System Seven software package for data acquisition and analysis.

The oxidation kinetics of powders of the healing materials (TiC, Ti_2AlC and Cr_2AlC) were investigated with combined thermogravimetry and differential thermal analysis (TGA/DTA) using a SETSYS Evolution 1750 (Setaram, France). To this end 20 ± 1 mg powder is put into 250 µL alumina crucible and heated to 1400 °C at different heating rates (1, 2, 5, 10 and 15 °C min^{-1}) in a flow of pure and dry synthetic air, i.e. 40 mL min^{-1} of N_2 (> 5N) and 10 mL min^{-1} of O_2 (> 5N). The relation between the heating rate β and the measured peak temperature (T_p) is given by the Kissinger-Sunose-Akahira equation [28]:

$$\ln\left(\frac{\beta}{T_p^2}\right) + \frac{E_A}{RT_p} = \text{constant} \tag{7.1}$$

where E_A is the activation energy and R is the gas constant. The slope of a straight line fitted to the data points for versus yields the activation energy of the oxidation reaction. This relation is based on first order reaction kinetics, hence:

$$k = Aexp\left(\frac{-E_A}{RT}\right) \tag{7.2}$$

where k is the reaction rate and A the frequency factor. Earlier studies [29] have shown that a reaction rate, lnk, corresponding to -13 generally leads to full healing of cracks of

micron sized width within a time span of 1 h, whereas a value of -15 requires 3 h.

7.2.3. Initiation of local crack damage

As a result of the large differences in hardness and toughness different methods had to be applied to the three materials selected to induce local cracks whose healing behavior could be studied under the combustion chamber conditions.

In the case of the alumina-TiC composite material Vickers indentation (Zwick/Z2.5, Germany) at a load of 20 N were used to induce penny-shaped cracks. The relationship between the applied load and the length of crack generated was investigated; see Figure 7.1. The indent size (2a) is defined by the average of the diagonals of the imprint made, whiles the crack length (2c) is defined as the average of the horizontal and vertical cracks formed in addition to the indent size. The fracture toughness was calculated to be 4.3 ± 0.1 MPa$\sqrt{m}$ [30]. This is slightly higher than the reported values for the constituents, i.e., 4.0 ± 0.1 MPa$\sqrt{m}$ for monolithic Al_2O_3 [31] and 3.8 MPa$\sqrt{m}$ for TiC [32]. When applying a load of less than 5 N the Vickers indenter did not generate any crack. However, at 20 N an appreciable surface crack of length 100 µm forms. The cracks opened up to a width of about 1 µm, see Figure 7.5(a) and (b).

In the case of Ti_2AlC samples neither indentation nor an impact method resulted in finite cracks within the samples. In this case thermal shock treatments were applied. Crack formation due to thermal shock first occurred at a temperature difference between heating and cooling of 450 °C. Micro-cracks of less than 2 µm in width were formed. For maximum temperatures between 450 and 950 °C cracks between 5 and 20 mm in length were formed by quenching in water. Based on 16 experiments the results were reproducible. Crack widths remained between 1 and 15 µm in this temperature range.

The Ti_2AlC samples used in the combustion study were quenched from 850 °C. This led to a large crack of 10 µm width and 20 mm length in the pure Ti_2AlC disk through the sample thickness. The second Ti_2AlC sample, containing TiC, Ti_3AlC and Ti_3Al impurities formed a crack of 5 µm in width and of approx. 0.5 mm in depth.

In the fine grained Cr_2AlC samples microcracks could be created with the Vickers indenter by applying a load of 300 N for 12 s. Cracks of about 140 µm, having a width of less than 1 µm were obtained. Per disc 10 of such cracks were produced in the samples to be tested in the combustion chamber. The fracture toughness value was estimated to be 8.7 MPa$\sqrt{m}$ using the load dependence of the indentation crack length.

In the case of the coarse grained material indention loading did not result in radial cracks and only caused local plastic deformation. To induce local cracks of finite dimensions, coarse grained Cr_2AlC discs were clamped to a steel plate and subjected to low velocity perpendicular impact using 10 mm tungsten carbide balls. Beyond a critical impact energy, cracks were initiated at the crater edge and then propagated in the radial direction [33, 34]. The correlation between impact energy and inducing cracks is depicted in Figure 7.2. The threshold impact energy for Cr_2AlC is about 50 mJ. A crack with a length of 700 µm and a maximum crack opening of 2.5 µm is observed in the coarse grained sample tested in the combustion chamber.

Samples tested in the combustion chamber contained cracks initiated by methods described above. Al_2O_3/TiC composites and both the fine and course grained Cr_2AlC had more than 5 cracks with lengths up to 1 mm and an average width of less than

(a)

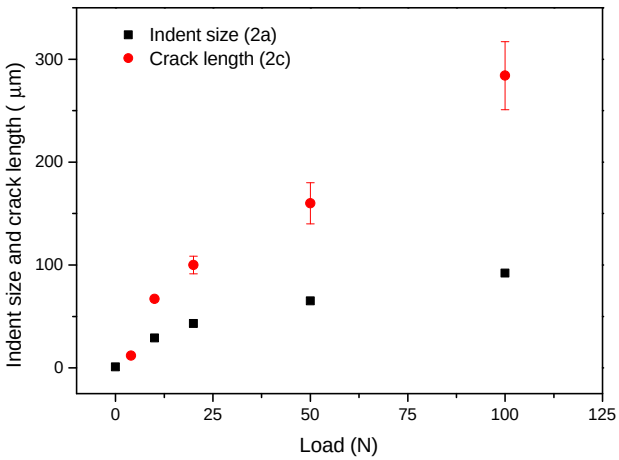

(b)

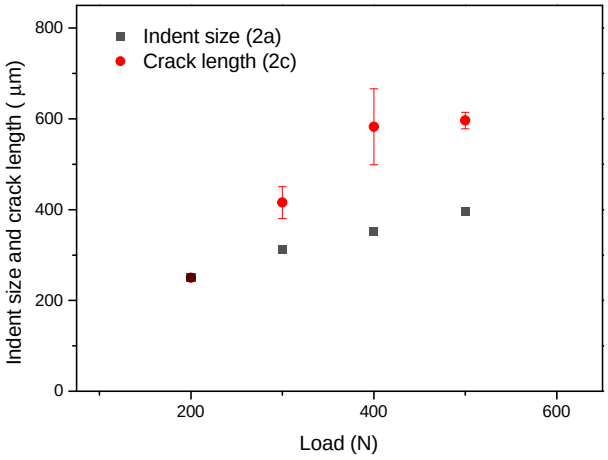

Figure 7.1: Vickers Indent size and crack length versus applied load of (a) Al_2O_3 with 20 vol. % TiC composite and (b) fine grained Cr_2AlC.

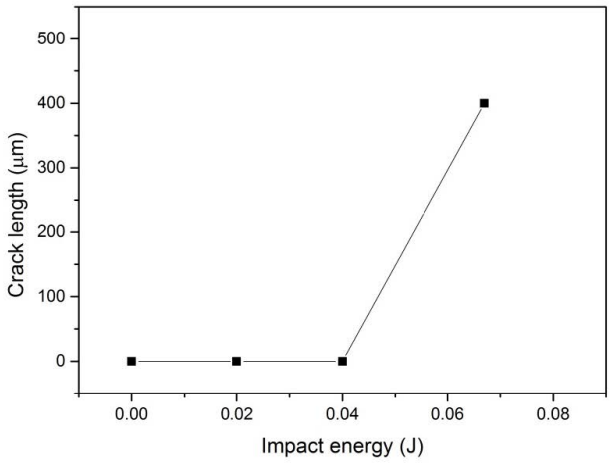

Figure 7.2: Crack length versus impact energy for cracks created in coarse grained Cr_2AlC by impact of WC balls.

2 µm. The through crack produced by thermal shock in the high purity Ti_2AlC sample was 10 µm wide and 20 mm in length, while the impurities of the second Ti_2AlC sample resulted in a thinner 5 µm crack with of approx. depth of 0.5 mm, while comparable in length.

7.2.4. Crack healing in a combustion chamber

To investigate healing of crack damage at conditions encountered in a real combustion chamber, samples were placed in a combustor setup (Limousine Combustor, UTwente, The Netherlands [35]); see Figure 7.3. The flow in the combustor is turbulent, as the Reynolds number is well above 4000 for all conditions. The combustor is operated at atmospheric pressure and the gases are injected at room temperature. The fuel used is 100 % methane at room temperature. The air and fuel flow are controlled from a PC with control software and mass flow controller valves. The air and fuel mass flow are about 24.62 $g\,s^{-1}$ and 0.8 $g\,s^{-1}$, respectively resulting in an average gas flow speed of 16 $m\,s^{-1}$ at the location of the samples. The combustor is operated at an operating point with a thermal power of 40 kW and an air excess factor of 1.8. The air factor is the ratio of the actual fuel-to-air flow rate ratio to the fuel-to-air flow rate ratio necessary for stoichiometric combustion and indicates the excess of air in the chemical reaction. The combustor can operate in a stable or unstable regime. In the unstable regime pressure oscillations are amplified by the combustion process and they grow in a limit cycle to amplitudes of 160 dB Sound Pressure Level. This phenomenon can happen in gas turbine engines but is to be avoided with a view to fatigue damage. Under the conditions mentioned before, the combustor is running stable and the observed pressure oscillations are lower (about 100 dB) and representative for normal operation of a gas turbine engine. The adi-

Table 7.3: Properties of sintered materials and impurities as detected by X-ray diffraction.

Sample	Impurities	Average grain size (μm)	Density (%)	Hardness (GPa)
Al_2O_3/TiC-01	WC	4.5	95%	18.7
Al_2O_3/TiC-02	WC	4.5	99%	19.3
Ti_2AlC-P	none	15-40	95.8%	3.9
Ti_2AlC-LP	TiC, Ti_3AlC_2, TiAl	15-40	95.1%	3.5
Cr_2AlC-FG	Cr	2	99.1%	6.0
Cr_2AlC-CG	Cr_7C_3	20-30	98.7%	3.2

abatic flame temperature and oxygen concentration at equilibrium conditions can be estimated using Chemkin Equil [36] assuming constant pressure and enthalpy. Using the GRI-Mech 3.0 reaction mechanism [37] and an initial temperature of 295 K the adiabatic flame temperature at these operating conditions is estimated to be about 1581 K. Under the above mentioned assumptions of adiabatic, isobaric conditions and assuming that the reacting mixture has already reached the equilibrium state, the oxygen mole fraction at the sample holder location is computed to be about 0.0876. Assuming a mixture of ideal gases, the volume fraction of oxygen then becomes 8.76 %vol.

The 6 samples (3 sets of 2) were mounted in an Inconel 800 holder suspended midway in the exhaust of the combustor; see Figure 7.3. Samples are arranged back to back so both samples of one material are exposed to the same conditions; see Figure 7.3b. After exposure to the chamber conditions for 4.5 hours, the samples were removed after switching off the fuel supply and allowing the chamber to cool down in approximately 45 minutes. The temperature at the sample holder was approx. 1000 °C. Temperature fluctuations during the course of the experiment were of the order of ± 2 °C.

After exposure and subsequent cooling down the samples were examined using SEM and XMA. Both the surface and cross-sections prepared by cutting with a diamond blade were investigated regarding the oxides formed and crack gap volume filled.

7.3. Results

7.3.1. Materials Characterisation

All sintered materials were found to have a density above 95 %; see Table 7.3. The ceramic composite samples (Al_2O_3/TiC) showed traces of WC, an impurity of the TiC powder. Impurities in the MAX phase ceramics stem from incomplete reactions during synthesis. Cr_2AlC was prepared with a fine and course grained microstructure resulting in a different hardness, viz. 6.0 and 3.2 GPa, respectively. The average grain sizes are reported in Table 7.3.

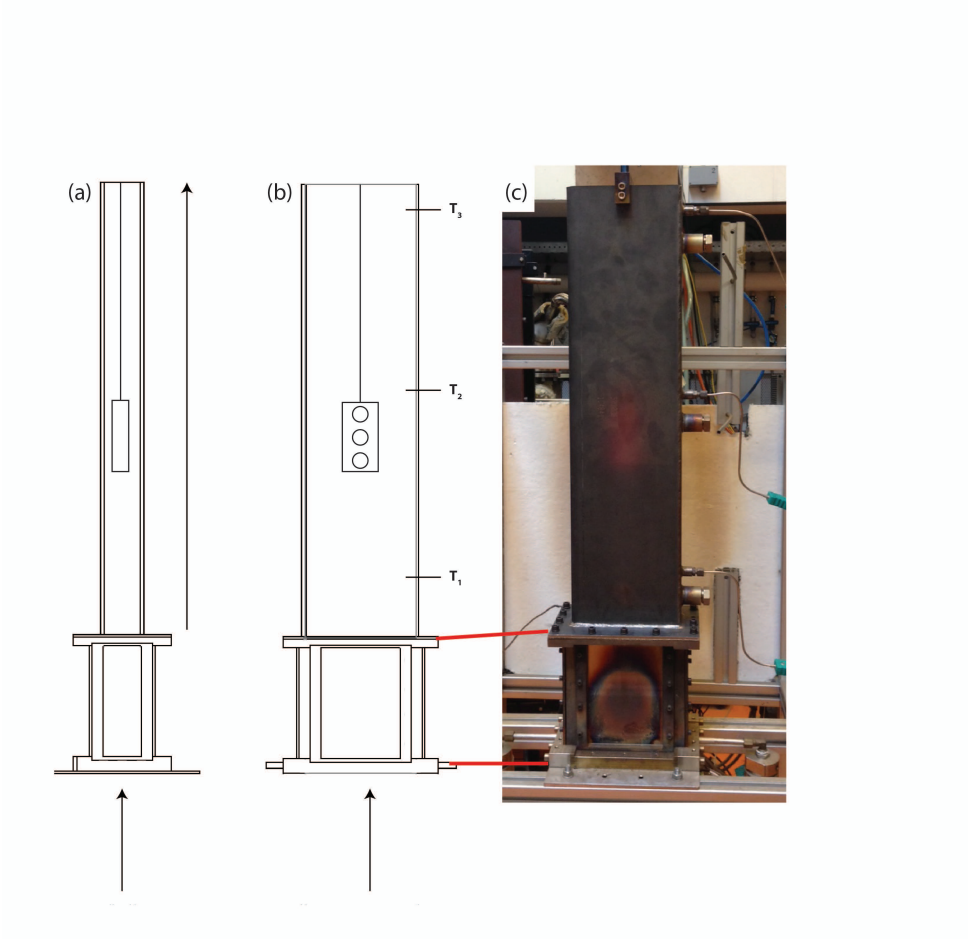

Figure 7.3: Combustion setup: (a) schematic side view with arrows indicating gas flow direction, (b) front view showing the position of the sample holder and thermocouples and (c) actual experimental setup.

7.3.2. Oxidation of TiC, Ti_2AlC and Cr_2AlC in air and combustion environment

Differential thermal analysis of the powdered healing agents TiC, Ti_2AlC and Cr_2AlC determined oxidation reaction peaks for all materials below 1300 °C. In Figure 7.4 the reaction rates are plotted as a function of the inverse temperature for the three powders investigated. Taking the values of -15 and -13 for the natural logarithm of the reaction rate as the lower and upper value for optimal healing [29] (cf. Section 7.2.2), we find the following optimal annealing temperatures, 600-660 °C for the formation of TiO_2 from TiC. For Ti_2AlC the temperature range is 556-580 °C and 826-885 °C for the formation to TiO_2 and Al_2O_3 respectively. And for Cr_2AlC it is 929-963 °C and 1170-1257 °C for the formation of Al_2O_3, and Cr_2O_3 respectively.

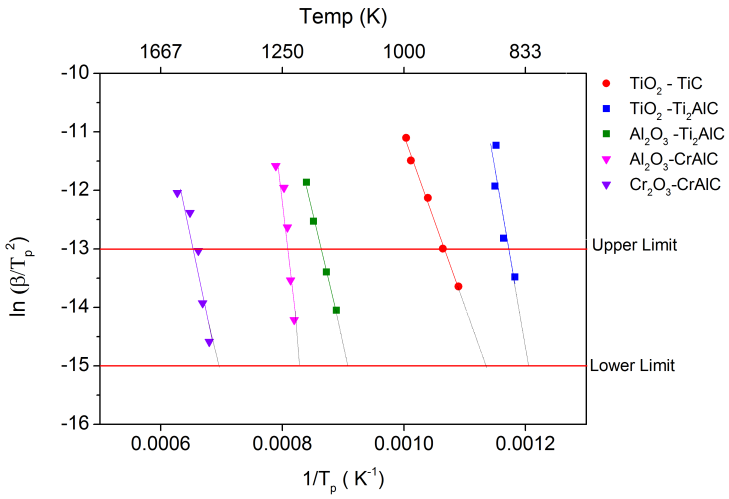

Figure 7.4: Evaluating the activation energy for the different reactions occurring during oxidation of all healing materials considered (Plot of reactivity versus peak temperature).

After exposure in the combustion chamber for 4 h where the temperature at sample location was measured to be between 940 and 1100 °C the colour of the Al_2O_3/TiC samples had changed from very dark grey to light grey, indicating full oxidation. Observations at higher resolution in the SEM showed that islands of TiO_2 formed all over the surface on top of the TiC particles. The activation energy of the complete transformation of TiC to rutile amounts to 242 ± 11 kJ mol^{-1} according to DTA. After removing the surface oxides by diamond polishing complete filling of the cracks with oxide was observed; see Figure 7.5(c) and (d). Even, after removing a layer of about 10 µm by diamond polishing, the indentation induced cracks appeared to be fully filled with oxides. This suggests that the cracks running from the surface inside the composite are healed. Moreover, it seems that the oxides grew laterally from the TiC particles along the crack gap, while the oxides on the surface grew locally.

Observation of the tested Ti_2AlC samples showed dark discoloration on the surface exposed to the combustion environment. Both Ti_2AlC samples showed significant oxide growth after being exposed to the combustion environment for 4 h. Grains of less than 5 µm cover the complete surface and all cracks smaller than 10 µm in width within the indents; see Figure 7.6. The outer layer of the oxide was identified as TiO_2 by SEM-XMA and XRD. A uniform and dense mixed oxide layer with a thickness of about 13 µm developed on the high purity Ti_2AlC material. According to DTA analysis small amounts of TiO_2 are expected to form around 570 °C while full rutile transformation is achieved at 700 °C, followed by Al_2O_3 formation around 800 °C.

The thermally induced crack in pure Ti_2AlC was fully filled with TiO_2 and Al_2O_3 up to a depth of 1.2 mm; see Figure 7.6. Beyond this depth, oxides were formed at the opposing fracture surfaces, however not fully bridging the crack gap. The Ti_2AlC material

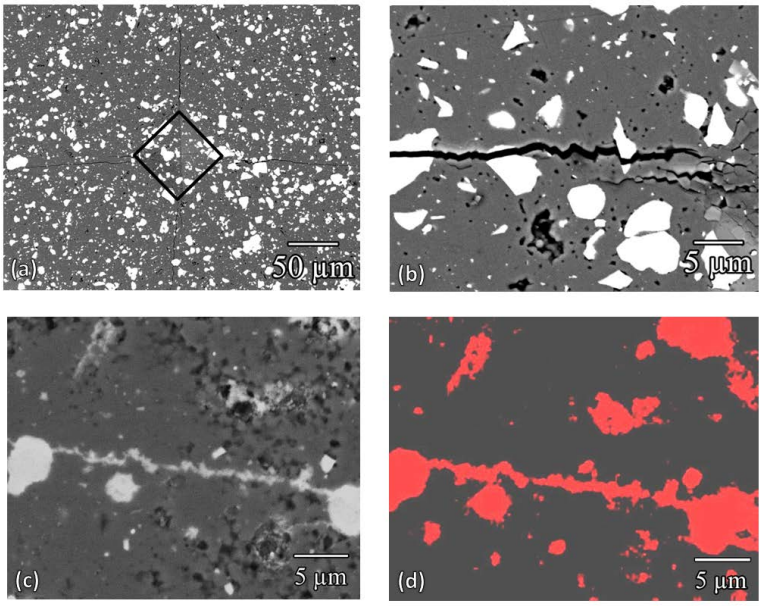

Figure 7.5: SEM micrographs of Al_2O_3/TiC composite. (a) Cracks created by Vickers indentation: (b) close-up showing crack-particle interaction, (c) healed crack after exposure to combustion environment for 4 h, (d) Ti X-ray mapping showing the filling of the healed crack.

containing impurities of TiC, Ti_3AlC and Ti_3Al formed a 15 µm thick mixed oxide scale with an outer layer of TiO_2 of approx. 3 µm thickness. The crack, having a jagged path and a width of only 1 µm was fully filled up to its crack tip at a depth of 0.5 mm. The oxide within the crack gap is Al_2O_3. Given that oxidation still occurs at oxygen potentials lower than in atmospheric air (0.088 vs 0.2 atm), the fact that cracks 1.2 mm below the surface were not fully closed was attributed to regions of the crack being sealed by surrounding oxide bridges or to the lower rate of oxidation.

The oxidation of Cr_2AlC requires higher temperatures and is slower compared to Ti_2AlC. Formation of Al_2O_3 begins around 900 to 1000 °C. A second peak in the heat flow signal of the DTA analysis at 1170-1275 °C corresponds to the formation of an Al_2O_3 and $(CrAl)_2O_3$ solid solution according to XRD. The oxide grown on the surface after 4 h of oxidation in the combustion chamber was about 0.24 µm and 0.19 µm thick on the fine and coarse gained sample, respectively. These oxide layers are thinner than the oxide layers formed in synthetic air for corresponding temperature and time, namely: 0.6 µm and 0.5 µm, respectively. Apparently the lower oxygen partial pressure in the combustion ambient as compared with that of air resulted in low oxide nucleation density (i.e. larger oxide grain size) and consequently slower oxidation kinetics. Hence, cracks with a width of less than 0.5 µm were fully healed with oxide and those with larger crack opening were only partially healed; see Figure 7.7.

The significant difference in oxygen partial pressure from standard self-healing investigations performed in synthetic or atmospheric air (0.2 atm) to the conditions found

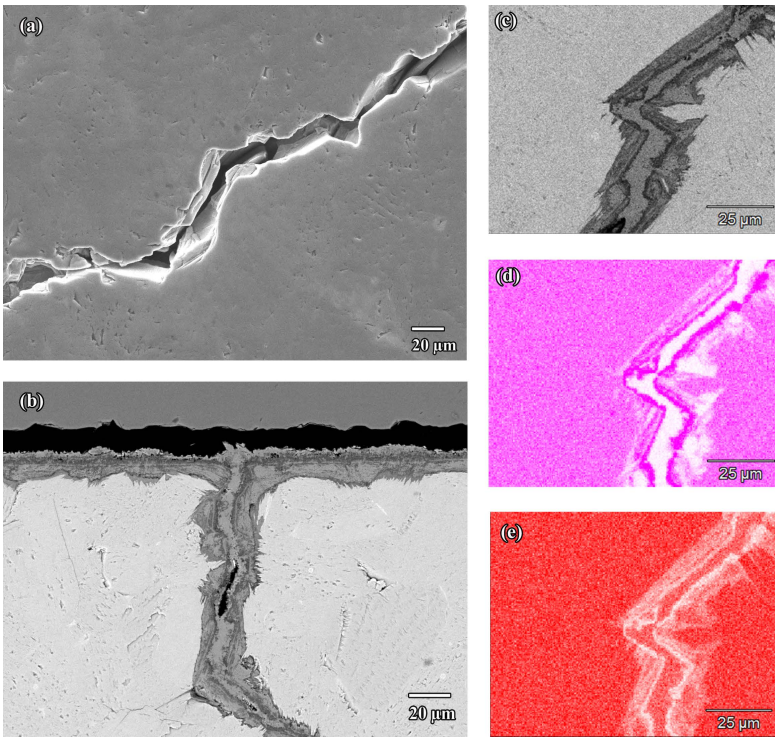

Figure 7.6: (a) Cracks in Ti_2AlC-A after quenching in water from 850 °C; (b) cross-section of healed crack after exposure to combustion conditions for 4 h; (c) close up of healed crack; (d) Al X-ray map; (e) Ti X-ray map.

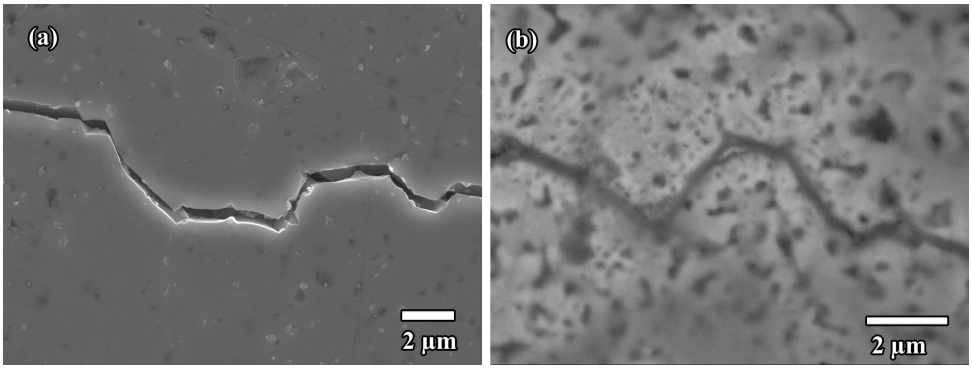

Figure 7.7: (a) Crack damage in fine grained Cr_2AlC generated by Vickers indentation; (b) Crack healed by Al_2O_3 formed in combustion environment for 4 h.

in the combustion setup (0.088 atm) show no significant impairment of the healing ability in the case of the three tested materials. The lower PO_2 resulted in thinner oxide scales for Cr_2AlC than those found in thermal gravimetric analysis, 0.2 to 0.5 µm for fine grained Cr_2AlC. Healing in Ti_2AlC and Al_2O_3/TiC was not affected by the reduced oxygen partial pressure. Surprisingly other compositional changes to the atmosphere due to combustion, e.g. higher NOx content, showed no effect on sample composition.

7.4. Conclusions

Three high temperature ceramic systems, Al_2O_3/TiC, Ti_2AlC and Cr_2AlC were investigated concerning their fracture, oxidation and self-healing behavior under real combustion conditions. All tested materials showed full crack-gap filling for 0.5 to more than 10 µm wide cracks of up to 20 mm length, after exposure to the high velocity exhaust gas mixture at approx. 1000 °C for 4 h. Although the oxygen partial pressure in the combustion chamber is much lower than in air (0.088 versus 0.2 atm), the conditions are sufficient to realize full healing of crack damage. The high gas flow rate (16 m s^{-1}) and thermal load did not impair the healing process.

References

[1] A.-S.Farle, L. Boatemaa, L. Shen, S. Gövert, J. B. W. Kok, M. Bosch, S. Yoshioka, S. van der Zwaag, and W. G. Sloof, *Demonstrating the self-healing behaviour of some selected ceramics under combustion chamber conditions,* Smart Materials and Structures **25**, 084019 (2016).

[2] G. M. Song, *Self-healing of max phase ceramics for high temperature applications: evidence from Ti_3AlC_2,* in *Advances in Science and Technology of $M_{n+1}AX_n$ Phases,* edited by I. M. Low (Woodhead Publishing, 2012) pp. 271–288.

[3] A. Ganguly, M. W. Barsoum, and R. D. Doherty, *Interdiffusion between Ti_3SiC_2–Ti_3GeC_2 and Ti_2AlC–Nb_2AlC diffusion couples,* Journal of the American Ceramic Society **90**, 2200 (2007).

[4] S. Li, G. Song, K. Kwakernaak, S. van der Zwaag, and W. G. Sloof, *Multiple crack healing of a Ti_2AlC ceramic,* Journal of the European Ceramic Society **32**, 1813 (2012).

[5] K. Ando, T. Ikeda, S. Sato, F. Yao, and Y. Kobayasi, *A preliminary study on crack healing behaviour of Si_3N_4/SiC composite ceramics,* Fatigue & Fracture of Engineering Materials & Structures **21**, 119 (1998).

[6] K. Ando, M. C. Chu, F. Yao, and S. Sato, *Fatigue strength of crack-healed Si_3N_4/SiC composite ceramics,* Fatigue & Fracture of Engineering Materials & Structures **22**, 897 (1999).

[7] Y.-W. Kim, K. Ando, and M. C. Chu, *Crack-healing behavior of liquid-phase-sintered silicon carbide ceramics,* Journal of the American Ceramic Society **86**, 465 (2003).

[8] K. Ando, Y. Shirai, M. Nakatani, Y. Kobayashi, and S. Sato, *(crack-healing+proof test): a new methodology to guarantee the structural integrity of a ceramics component,* Journal of the European Ceramic Society **22**, 121 (2002).

[9] K. Takahashi, B.-S. Kim, M.-C. Chu, S. Sato, and K. Ando, *Crack-healing behavior and static fatigue strength of Si_3N_4/SiC ceramics held under stress at temperature (800, 900, 1000 °C),* Journal of the European Ceramic Society **23**, 1971 (2003).

[10] T. Osada, W. Nakao, K. Takahashi, K. Ando, and S. Saito, *Strength recovery behavior of machined Al_2O_3/SiC nano-composite ceramics by crack-healing,* Journal of the European Ceramic Society **27**, 3261 (2007).

[11] R. Sugiyama, K. Yamane, W. Nakao, K. Takahashi, and K. Ando, *Effect of difference in crack-healing ability on fatigue behavior of alumina/silicon carbide composites,* Journal of Intelligent Material Systems and Structures **19**, 411 (2008).

[12] F. Yao, K. Ando, M. Chu, and S. Sato, *Crack-healing behavior, high temperature and fatigue strength of SiC-reinforced silicon nitride composite,* Journal of Materials Science Letters **19**, 1081 (2000).

[13] J. Korouš, M. C. Chu, M. Nakatani, and K. Ando, *Crack healing behavior of silicon carbide ceramics,* Journal of the American Ceramic Society **83**, 2788 (2000).

[14] F. Yao, K. Ando, M. Chu, and S. Sato, *Static and cyclic fatigue behaviour of crack-healed Si_3N_4/SiC composite ceramics,* Journal of the European Ceramic Society **21**, 991 (2001).

[15] K. Ando, K. Furusawa, M. C. Chu, T. Hanagata, K. Tuji, and S. Sato, *Crack-healing behavior under stress of mullite/silicon carbide ceramics and the resultant fatigue strength,* Journal of the American Ceramic Society **84**, 2073 (2001).

[16] S. Yoshioka, L. Boatemaa, S. van der Zwaag, W. Nakao, and W. G. Sloof, *On the use of TiC as high-temperature healing particles in alumina based composites,* Journal of the European Ceramic Society **36**, 4155 (2016).

[17] G. M. Song, Y. T. Pei, W. G. Sloof, S. B. Li, J. De Hosson, and S. van der Zwaag, *Oxidation-induced crack healing in Ti_3AlC_2 ceramics,* Scripta Materialia **58**, 13 (2008).

[18] H. J. Yang, Y. T. Pei, J. C. Rao, J. T. M. De Hosson, S. B. Li, and G. M. Song, *High temperature healing of Ti_2AlC: On the origin of inhomogeneous oxide scale,* Scripta Materialia **65**, 135 (2011).

[19] S. Li, L. Xiao, G. Song, X. Wu, W. G. Sloof, and S. van der Zwaag, *Oxidation and crack healing behavior of a fine-grained Cr_2AlC ceramic,* Journal of the American Ceramic Society **96**, 892 (2013).

[20] D. J. Tallman, B. Anasori, and M. W. Barsoum, *A critical review of the oxidation of Ti_2AlC, Ti_3AlC_2 and Cr_2AlC in air,* Materials Research Letters **1**, 115 (2013).

[21] A.-S. Farle, C. Kwakernaak, S. van der Zwaag, and W. G. Sloof, *A conceptual study into the potential of $M_{n+1}AX_n$-phase ceramics for self-healing of crack damage,* Journal of the European Ceramic Society **35**, 37 (2015).

[22] S. Li, X. Chen, Y. Zhou, and G. Song, *Influence of grain size on high temperature oxidation behavior of Cr_2AlC ceramics,* Ceramics International **39**, 2715 (2013).

[23] C.-J. Wang and C.-Y. Huang, *Effect of TiO_2 addition on the sintering behavior, hardness and fracture toughness of an ultrafine alumina,* Materials Science and Engineering: A **492**, 306 (2008).

[24] T. Liao, J. Wang, M. Li, and Y. Zhou, *First-principles study of oxygen incorporation and migration mechanisms in Ti_2AlC,* Journal of Materials Research **24**, 3190 (2009).

[25] M. W. Barsoum, T. H. Scabarozi, S. Amini, J. D. Hettinger, and S. E. Lofland, *Electrical and thermal properties of Cr_2GeC,* Journal of the American Ceramic Society **94**, 4123 (2011).

[26] Z. M. Sun, *Progress in research and development on MAX phases: A family of layered ternary compounds,* International Materials Reviews **56**, 143 (2011).

[27] ASTM B962-15, *Standard Test Methods for Density of Compacted or Sintered Powder Metallurgy (PM) Products Using Archimedes' Principle*, Standard (ASTM International, West Conshohocken, PA, USA, 2015).

[28] H. E. Kissinger, *Variation of peak temperature with heating rate in differential thermal analysis,* Journal of Research of the National Bureau of Standards **57**, 217 (1956).

[29] S. Yoshioka and W. Nakao, *Methodology for evaluating self-healing agent of structural ceramics,* Journal of Intelligent Material Systems and Structures **26**, 1395 (2014).

[30] A. G. Evans and E. A. Charles, *Fracture toughness determinations by indentation,* Journal of the American Ceramic society **59**, 371 (1976).

[31] V. Sglavo, E. Trentini, and M. Boniecki, *Fracture toughness of high-purity alumina at room and elevated temperature,* Journal of materials science letters **18**, 1127 (1999).

[32] J. L. Chermant, A. Deschanvres, and F. Osterstock, *Toughness and fractography of TiC and WC,* Fracture Mechanics of Ceramics **4**, 891 (1978).

[33] P. Duó, J. Liu, D. Dini, M. Golshan, and A. M. Korsunsky, *Evaluation and analysis of residual stresses due to foreign object damage,* Mechanics of Materials **39**, 199 (2007).

[34] A. G. Evans, M. E. Gulden, and M. Rosenblatt, *Impact damage in brittle materials in the elastic-plastic response regime,* Proceedings of the Royal Society A: Mathematical, Physical and Engineering Sciences **361**, 343 (1978).

[35] d. J. C. Roman Casado, *Nonlinear behavior of the thermoacoustic instabilities in the limousine combustor*, Thesis (2013), public.

[36] R. Kee, F. Rupley, J. Miller, M. Coltrin, J. Grcar, E. Meeks, H. Moffat, A. Lutz, G. Dixon-Lewis, and M. Smooke, *Chemkin collection, release 3.6, reaction design,* Inc., San Diego, CA (2000).

[37] G. P. Smith, D. M. Golden, M. Frenklach, N. W. Moriarty, B. Eiteneer, M. Goldenberg, C. T. Bowman, R. K. Hanson, S. Song, and W. C. Gardiner Jr, *Gri-mech 3.0,* $http://www.me.berkeley.edu/gri\_mech$ **51**, 55 (1999).

Acknowledgements

To begin, I would like to express my gratitude to the two men who gave me a shot at research after a single skype interview. Wim and Sybrand have both shown great patience and confidence in my (eventual) success. Without their continuous support and straight feedback this thesis would not be in your (the readers) hands now.
I would like to also gratefully acknowledge the funding schemes that have made this thesis possible: the Marie Curie SHeMat programme and DCMat.
Throughout my time at the MSE department I've gotten to work and interact with so many people, that I will not attempt to list all names. But a special shout out goes to Hans Brouwer and Kees Kwakernaak, who've made all the time spent in the lab a success and the many hours polishing or sintering samples feel less like work. To everyone, past and present, on the fourth floor: It's been a pleasure to work side by side with you all these years and I am excited and happy to see everyone succeeding in their own ways.
I need to thank Casper, Kelvin and Robert-Jan for inspiring, confusing, distracting and highly entertaining 'Fensterbank'-talks that made me laugh more than should be allowed in a serious work place. Dancing, an occasional after work beer, but most of all, very confusing conversations will color my memories of this phd thanks to them!
I should also acknowledge many other people who have made the past 4,5 years an unforgettable experience. From Tubalkain to NovAm and everyone in between: Prost!
Some names that defy categorization: Romain, Brennan, Merel, Sarah, Yusuf, Filipe.
Special thanks goes to Jil: the best outcome of a Graduate School Course, ever. We've done everything together, from long kakao-breaks, to late nights both working and not, and even eventually graduating two weeks apart!
To my German big brother in the Netherlands: Danke Heiko! Can't imagine a PhD or life without you.
Keeping it short and sweet: Thank you Ashwath.
Last but not least: my family. From new additions (Hello Caspar!) and an adopted sister (Emma) to the glue that holds it all together (Mama), this PhD would never have happened without you. Ninja, Papa, Mama, Wenne, Danke für die Geduld, Unterstützung, Besuche und Ablenkung! Familie kann man sich nicht aussuchen; ich hab einfach die Beste.

List of Publications

6. **A. S. Farle**, J. Krishnasamy, S. Turteltaub, C. Kwakernaak, S. van der Zwaag, W. G. Sloof, *Determination of fracture strength and fracture energy of (metallo-) ceramics by a wedge loading methodology and corresponding cohesive zone-based finite element analysis*, Fracture Mechanics, (-), **submitted**.

5. **A. S. Farle**, S. Stikkelman, S. van der Zwaag, W. G. Sloof, *Oxidation and self-healing behaviour of spark plasma sintered Ta_2AlC*, Journal of the European Ceramic Society **37**, 1969-1974 (2017).

4. **A. S. Farle**, L. Boatemaa, L. Shen, S. Gövert, J. B. W. Kok, M. Bosch, S. Yoshioka, S. van der Zwaag, W. G. Sloof, *Demonstrating the self-healing behaviour of some selected ceramics under combustion chamber conditions*, Smart Materials and Structures **25**,(2016).

3. **W. G. Sloof**, R. Pei, A. S. McDonald, J. L. Fife, L. Shen, L. Boatemaa, A. S. Farle, K. Yan, X. Zhang, S. van der Zwaag, and P.D. Lee, and P. J. Withers, *Repeated crack healing in MAX-phase ceramics revealed by 4D in situ synchrotron X-ray tomographic microscopy*, Scientific Reports **6**, 23040 (2016).

2. **W. G. Sloof**, A. S. Farle, L. Shen, *Intrinsic autonomous crack healing in MAX phase ceramics*, In: Self healing materials - pioneering research in the Netherlands, S. van der Zwaag, E. Brinkman (ed), IOP Press, 115-123 (2015).

1. **A. S. Farle**,C. Kwakernaak, S. van der Zwaag, W.G. Sloof, *A conceptual study into the potential of $M_{n+1}AX_n$-phase ceramics for self-healing of crack damage*, Journal of the European Ceramic Society **35**, 37-45 (2015).

Curriculum Vitæ

Ann-Sophie Farle

Ann-Sophie M. Farle was born November 19th, 1988 in Berlin, Germany. After completing high school (Abitur) in Mülheim an der Ruhr she attended the Rheinisch Westfälische Technische Hochschule (RWTH) Aachen to pursue a degree in Engineering and Economics: Materials Science and Process Technology. Working as a teaching and research assistant during her studies and after a 3 month internship in Nanjing, China, she graduated with a Bachelor of Science degree in December of 2010. Ann-Sophie completed her Master studies at the University of Queensland (UQ) in Brisbane, Australia, in December 2011 in Engineering Science: Materials Engineering.

Since October 2012 Ann-Sophie Farle has been a PhD candidate at Delft University of Technology on self-healing MAX-phases at the Department of Material Science and Engineering of the Faculty of 3mE. As part of a Marie Curie Initial Training Network (SHeMat) she attended regular workshops for young scientists throughout Europe. Aside from her own research, she has been teaching Bachelor and Master students and has been an active member of both the 3mE Graduate School PhD Council and the MSE Tubalkaïn Student association.